

FACULTY OF PHYSICS AND ASTRONOMY

UNIVERSITY OF HEIDELBERG

MEASUREMENT OF DIJET CROSS SECTIONS
IN DIFFRACTIVE PHOTOPRODUCTION AT HERA

by

SEBASTIAN SCHÄTZEL

DIPLOMA THESIS IN PHYSICS

December 2000

This thesis was carried out at the Physical Institute of the University of Heidelberg, Germany, under the supervision of Prof. Dr. F. Eisele.

Abstract

A measurement is presented of differential dijet cross sections in low- $|t|$ diffractive photoproduction processes of the type $ep \rightarrow eXY$, in which the photon dissociation system X is separated from a low-mass baryonic system Y by a large rapidity gap. The data, corresponding to an integrated luminosity of 7.54 pb^{-1} , were collected in the year 1996 with the H1 experiment at the HERA collider. The cross sections are given on stable hadron level and cover the kinematic range $165 \text{ GeV} < W < 250 \text{ GeV}$, $x_{\mathbb{P}} < 0.05$, $p_T^{\text{jct}} > 4 \text{ GeV}/c$.

The Resolved Pomeron Model with pomeron parton distributions extracted in diffractive deep inelastic ep scattering describes reasonably well the shapes of the differential cross sections but fails in the normalization by a factor 2.5. A consistent description of both the normalization and the shapes is obtained by applying a suppression factor to the model which depends on the fractional pomeron momentum $z_{\mathbb{P}}$ entering in the hard subprocess.

Übersicht

Differentielle Wirkungsquerschnitte diffraktiver Zweijet-Ereignisse in Photoproduktion vom Typ $ep \rightarrow eXY$ wurden gemessen, in denen das dissoziative Photonsystem X durch eine große Rapiditätslücke vom baryonischen System Y niedriger Masse getrennt und der am Protonvertex übertragene Impuls klein ist. Die Daten, die einer integrierten Luminosität von 7.54 pb^{-1} entsprechen, wurden im Jahr 1996 mit dem H1-Experiment am HERA-Beschleuniger aufgezeichnet. Die Wirkungsquerschnitte sind für das Niveau stabiler Hadronen gegeben und umfassen den kinematischen Bereich $165 \text{ GeV} < W < 250 \text{ GeV}$, $x_{\mathbb{P}} < 0.05$, $p_T^{\text{jct}} > 4 \text{ GeV}/c$.

Das Resolved-Pomeron-Modell mit Pomeron-Partondichten gemessen in diffraktiver tief-inelastischer ep -Streuung beschreibt die Form der differentiellen Wirkungsquerschnitte zufriedenstellend, versagt jedoch in der Normierung um einen Faktor 2.5. Eine konsistente Beschreibung sowohl der Normierung als auch der Form wird durch Anwendung eines Unterdrückungsfaktors auf das Modell erzielt, der vom in den harten Streuprozess eingehenden Impulsbruchteil des Pomerons abhängt.

Contents

List of Figures	iii
1 Introduction	1
2 Theoretical Basis	3
2.1 Hadron-Hadron Interactions	3
2.1.1 Elastic Scattering	4
2.1.2 Diffractive Dissociation	4
2.1.3 Total Cross Sections	7
2.1.4 Regge Phenomenology	7
2.2 Diffractive Scattering	10
2.2.1 Rapidity Gaps	10
2.2.2 Diffractive Parton Distributions	11
2.2.3 Resolved Pomeron Model	11
2.2.4 Soft Colour Interaction Model	11
2.3 Diffractive Deep Inelastic Scattering at HERA	11
2.3.1 Deep Inelastic Scattering	11
2.3.2 Diffractive Structure Function of the Proton	12
2.3.3 Pomeron Parton Density Functions	13
2.3.4 Diffractive DIS Dijets	15
2.4 Diffractive $p\bar{p}$ Scattering at the Tevatron	15
2.5 Diffractive Photoproduction at HERA	16
2.6 Kinematics of Dijets in Diffractive Photoproduction	17
2.6.1 Overview	17
2.6.2 General Description of the Processes	17
2.6.3 Kinematical Reconstruction	20
2.7 Monte Carlo Generators	22
2.7.1 PYTHIA	22
2.7.2 POMPYT	22
2.7.3 DIFFVM	22
2.7.4 Hadronization	22
3 Experiment	24
3.1 HERA	24
3.2 H1 Detector	27
4 Analysis	32
4.1 Event Selection	32
4.1.1 Run Selection	32
4.1.2 Photoproduction Subtrigger S83	33

4.1.3	Jets	33
4.1.3.1	CDFCONE Jet Algorithm	33
4.1.3.2	Combined Objects	34
4.1.4	Detector Acceptance Cuts	35
4.1.5	Diffractive Cuts	35
4.1.6	Preselection	35
4.1.7	Summary and Event Display	36
4.2	Definition of the Cross Sections	36
4.3	Correction of Detector Effects	36
4.3.1	Detector Simulation	39
4.3.2	Monte Carlos used for Correction	40
4.3.3	Description of Uncorrected Data	44
4.3.4	Correction of the Data	47
4.3.5	Resolutions	50
4.3.6	Noise in Forward Detectors	50
4.3.7	Correction for Proton Dissociation	56
4.3.8	Systematic Errors	56
5	Results	58
5.1	Cross Sections	58
5.2	Comparison to the Resolved Pomeron Model with Parton Distributions extracted from DDIS	58
5.2.1	Test of hard QCD Scattering	58
5.2.2	Cross Section differential in z_{IP}^{had}	59
5.2.3	Suppression Factor $S(z_{IP})$	59
5.2.4	Cross Section differential in x_{γ}^{had}	60
5.2.5	Cross Section differential in x_{IP}^{had}	61
5.2.6	Cross Section differential in M_X^{had}	61
5.2.7	Cross Section differential in $\langle \eta_{\text{jet}}^{\text{had}} \rangle$	62
5.2.8	Cross Section differential in M_{12}^{had}	62
5.2.9	Cross Section differential in y^{had}	62
5.3	Summary of Results	62
5.4	Comparison to previous Measurements	62
6	Conclusions and Outlook	73
	Bibliography	75
A	χ^2 Fit of x_{IP}^{det}	77
A.1	Shape Fit	77
A.2	Factors to unnormalized Monte Carlo Events	78
B	Error Treatment	82
B.1	Sources of Uncertainty	82
B.2	Statistical Errors	85
B.3	Systematic Errors	85
B.3.1	Uncorrelated Systematic Errors	85
B.3.2	Correlated Systematic Errors	85
C	Tabulated Cross Sections	86

List of Figures

2.1	Proton-Proton Elastic Scattering Cross Section differential in t	5
2.2	Single Diffractive Dissociation $pp \rightarrow Xp$	6
2.3	Single Diffractive Dissociation Cross Section for $pp \rightarrow Xp$	6
2.4	Total Cross Sections for Hadron-Hadron Scattering	8
2.5	Regge Trajectories	9
2.6	Inclusive Diffractive Deep Inelastic Scattering	12
2.7	H1 QCD Fit Pomeron Parton Density Functions	14
2.8	DDIS Dijet BGF Process	15
2.9	Diffractive Structure Function of the Antiproton	16
2.10	Diffractive Dijet Process in Resolved Pomeron Model	18
3.1	HERA and Pre-Accelerators	25
3.2	HERA and H1 Integrated Luminosities	26
3.3	H1 Detector	28
3.4	H1 Luminosity System	30
3.5	Bethe Heitler Process	31
4.1	Event Display	37
4.2	$(x_{\mathbb{P}}^{\text{had}}, M_Y^{\text{had}})$ Plane of used Monte Carlos	41
4.3	$x_{\mathbb{P}}^{\text{det}}$ Fit Result	42
4.4	η_{max} Distribution	43
4.5	Background	44
4.6	Detector Level Distributions	45
4.7	Detector Level Distributions (cont'd)	46
4.8	Jet Profiles	47
4.9	Energy Flow on Detector Level	48
4.10	Efficiencies for Cross Section Variables	51
4.11	Resolutions and Correlations	53
4.12	Resolutions and Correlations (cont'd)	54
4.13	Resolutions and Correlations (cont'd)	55
5.1	Ratio of Cross Sections differential in $z_{\mathbb{P}}^{\text{had}}$	60
5.2	Differential Cross Section $d\sigma/dx_{\gamma}^{\text{had}}$, direct γ processes unsuppressed	61
5.3	Differential Cross Section $d\sigma/d\Delta\eta_{\text{jet}}^{\text{had}}$	64
5.4	Differential Cross Section $d\sigma/d\Delta\eta_{\text{jet}}^{\text{had}}, S(z_{\mathbb{P}})$	64
5.5	Differential Cross Section $d\sigma/d\langle p_T^{\text{jet,had}} \rangle$	65
5.6	Differential Cross Section $d\sigma/d\langle p_T^{\text{jet,had}} \rangle, S(z_{\mathbb{P}})$	65
5.7	Differential Cross Section $d\sigma/dz_{\mathbb{P}}^{\text{had}}$	66
5.8	Differential Cross Section $d\sigma/dz_{\mathbb{P}}^{\text{had}}, S(z_{\mathbb{P}})$	66
5.9	Differential Cross Section $d\sigma/dx_{\gamma}^{\text{had}}$	67

5.10	Differential Cross Section $d\sigma/dx_\gamma^{\text{had}}, S(z_{IP})$	67
5.11	Differential Cross Section $d\sigma/d\log_{10}(x_{IP}^{\text{had}})$	68
5.12	Differential Cross Section $d\sigma/d\log_{10}(x_{IP}^{\text{had}}), S(z_{IP})$	68
5.13	Differential Cross Section $d\sigma/dM_X^{\text{had}}$	69
5.14	Differential Cross Section $d\sigma/dM_X^{\text{had}}, S(z_{IP})$	69
5.15	Differential Cross Section $d\sigma/d\langle\eta_{j\text{et}}^{\text{had}}\rangle$	70
5.16	Differential Cross Section $d\sigma/d\langle\eta_{j\text{et}}^{\text{had}}\rangle, S(z_{IP})$	70
5.17	Differential Cross Section $d\sigma/dM_{12}^{\text{had}}$	71
5.18	Differential Cross Section $d\sigma/dM_{12}^{\text{had}}, S(z_{IP})$	71
5.19	Differential Cross Section $d\sigma/dy^{\text{had}}$	72
5.20	Differential Cross Section $d\sigma/dy^{\text{had}}, S(z_{IP})$	72
A.1	x_{IP}^{det} Fit	79
A.2	x_{IP}^{det} Fit Result	80

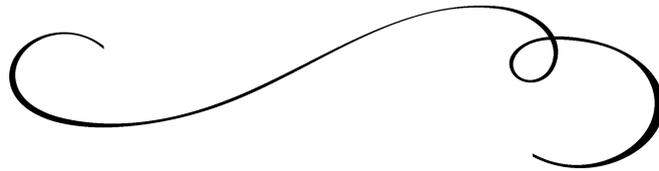
Acknowledgements

I am grateful to Prof. Eisele for giving me the chance to work on a current subject of particle physics. I thank him for his confidence in my work and for his excellent guidance through the complexity of this analysis and the topic of diffraction.

I thank Dr. A. Hebecker for the second marking of this thesis.

I thank the members of the Heidelberg H1 Group, J. Dingfelder, M. Ellerbrock, D. Emschermann, C. Gerlich, J. Marks, and C. Werner for their help and assistance in all aspects of every day work and the stimulating working atmosphere, and especially O. Behnke for salutary discussions and his help with fitting techniques. I thank F.-P. Schilling for his help and discussions.

I appreciate the helpful discussions with the members of the DESY Diffractive Working Group, in particular A. Buniatian, R. Demirchyan and S. Levonian.



Introduction

Quantum Chromodynamics (QCD) is the generally accepted theory of strong interactions. It is a non-abelian field theory based on the group $SU(3)$. Many phenomena can be successfully described and predicted using perturbative expansion ('perturbative QCD'). Because of the non-abelian character, however, the renormalization procedure leads to a running coupling constant, which is small only at small distances. The perturbative approach to QCD calculations is therefore limited to hard scales $Q \gg \Lambda_{\text{QCD}} \approx 0.2 \text{ GeV}$.

The total cross section of hadronic interactions is dominated by peripheral collisions, in which the hadrons stay intact and exchange only a small amount of energy. Since the beginnings of particle physics it has been the aim of physicists to understand this regime. In 1935 Yukawa introduced the pion as the exchange particle of the strong force. Because of its low mass, however, according to Heisenberg's Uncertainty Principle, it can only describe the long range part of the interaction. An extension to this model is provided by Regge phenomenology [Reg59], which can well describe hadronic interactions. However, it has remained a difficult task to understand the domain of soft hadronic interactions within the QCD framework.

A prime example is elastic pp scattering, where the two protons exchange energy and momentum but no discrete quantum numbers. Within QCD this exchange must be mediated by colourless states of quarks or gluons. At hadron colliders a class of events has been observed, in which a proton is scattered elastically and a large gap exists between the directions of this proton and the hadrons produced in the interaction. These gaps arise naturally if no net colour is exchanged (absence of colour strings). From the hadronic cross section differential in the squared momentum t transferred at the proton vertex, which at high energies resembles a diffraction pattern, these events have been titled 'diffractive.'

Diffractive processes with a hard scale can be treated in perturbative QCD by making assumptions on how final colour singlet states occur. In the *Resolved Pomeron Model* a colourless particle is exchanged in the early stage of the interaction. This exchange, the pomeron, has a partonic structure. An alternative approach is used in soft colour neutralization models. They assume that initially exchanged colour is rearranged during the interaction without changing the momentum configuration of the system.

The observation of diffractive events at the HERA ep collider has started a revival of experimental studies on diffractive scattering. While at HERA the focus was on diffractive deep inelastic scattering (DDIS), diffractive $p\bar{p}$ collisions were examined at Fermilab. The transition from DDIS to $p\bar{p}$ scattering can be studied in γp interactions at HERA.

In this thesis, differential cross sections were measured in diffractive photoproduction interactions with two jets. They are compared to predictions of diffraction models. The data were taken in 1996 with the H1 experiment at HERA.

The text is organized as follows: First, a brief review is given on the phenomena of elastic hadron scattering and the related theoretical models. The kinematics of diffractive γp scattering are introduced (chapter two). The detector is described in the third chapter. Chapter four contains the analysis procedure leading to the differential cross sections on hadron level. The resulting cross sections are compared to model predictions in chapter five. The thesis ends with conclusions and an outlook. Throughout the text natural units are used, in which $c = 1$.

Theoretical Basis

This chapter first introduces phenomena of hadron-hadron interactions and the phenomenological Regge model. Diffractive scattering is discussed in Sec. 2.2, where also different models are summarized. Deep inelastic diffractive ep scattering (DDIS) is described in Sec. 2.3 and compared in the following section to $p\bar{p}$ scattering results from the Tevatron. Sec. 2.5 discusses the characteristics of γp photoproduction processes. Photoproduction provides a transition from deep inelastic ep scattering (DIS) to hadron-hadron scattering. By measuring differential cross sections in diffractive γp interactions with two jets, the understanding of hard diffraction can be improved. These processes are introduced in Sec. 2.6 A brief description of the Monte Carlo generators used in the analysis ends the chapter.

2.1 Hadron-Hadron Interactions

In proton-proton interactions the following features are experimentally observed:

1. The elastic cross section differential in the squared momentum transfer t is exponentially peaked for $|t| \rightarrow 0$.
2. The single diffraction dissociation cross section differential in the fractional longitudinal momentum loss ξ of the quasi-elastically scattered proton is proportional to $1/\xi$ in the range $\xi < 0.15$.
3. The total cross section is increasing with rising s , the square of the centre-of-mass energy.

4. The forward elastic scattering peak becomes sharper, or *shrinks*, as s increases.

This section reviews these phenomena and gives a brief overview of the application of Regge theory to high energy particle physics.

2.1.1 Elastic Scattering

Fig. 2.1 shows the differential cross section $d\sigma/dt$ for elastic pp scattering for different proton momenta. As the proton energy increases, the exponential forward ($t \rightarrow 0$) elastic peak becomes sharper and a secondary maximum appears. This behaviour is reminiscent of the diffraction of light by a circular disk. The intensity of the scattered light is given by

$$\frac{I}{I_0} \approx 1 - \frac{R^2}{4} (k\theta)^2, \quad (2.1)$$

in which R is the radius of the disk, k is the wave number of the photons, and θ is the scattering angle.

Observed for elastic pp scattering is the behaviour

$$\frac{d\sigma/dt}{(d\sigma/dt)_{t=0}} = e^{bt} \approx 1 - b (p\theta)^2, \quad (2.2)$$

with the incident proton's momentum p . Comparison of Eqs. (2.1) and (2.2) leads to a relationship between the interaction radius and the slope parameter b :

$$b = R^2/4. \quad (2.3)$$

For the typical strong interaction radius $R = 1/m_\pi$, Eq. (2.3) yields $b = 12.5 \text{ GeV}^{-2}$. This is approximately what is observed at high energies [Gou00].

2.1.2 Diffractive Dissociation

The phenomenon of diffraction dissociation [Goo60], has no classical analogue. The single diffractive dissociation process $pp \rightarrow Xp$ is pictorially shown in Fig. 2.2. In this quasi-elastic scattering, one hadron remains intact, whereas the other hadron dissociates into a higher mass system, retaining its quantum numbers.

The Lorentz invariant double differential cross section $d^2\sigma/dt d(M_X^2/s)$ for this process is shown in Fig. 2.3. For large s , it is proportional to $1/M_X^2$ in the region $M_X^2/s < 0.15$.

This phenomenon can be understood in terms of coherent excitation of the dissociating hadron and the exchange of a colour singlet state with vacuum quantum numbers [Gou00]. The coherence condition demands the longitudinal momentum transfer ΔP_L to be smaller than the inverse of the longitudinal extension R_L of the excited proton:

$$\Delta P_L < \frac{1}{R_L} \approx m_\pi \frac{P_1}{m_p},$$

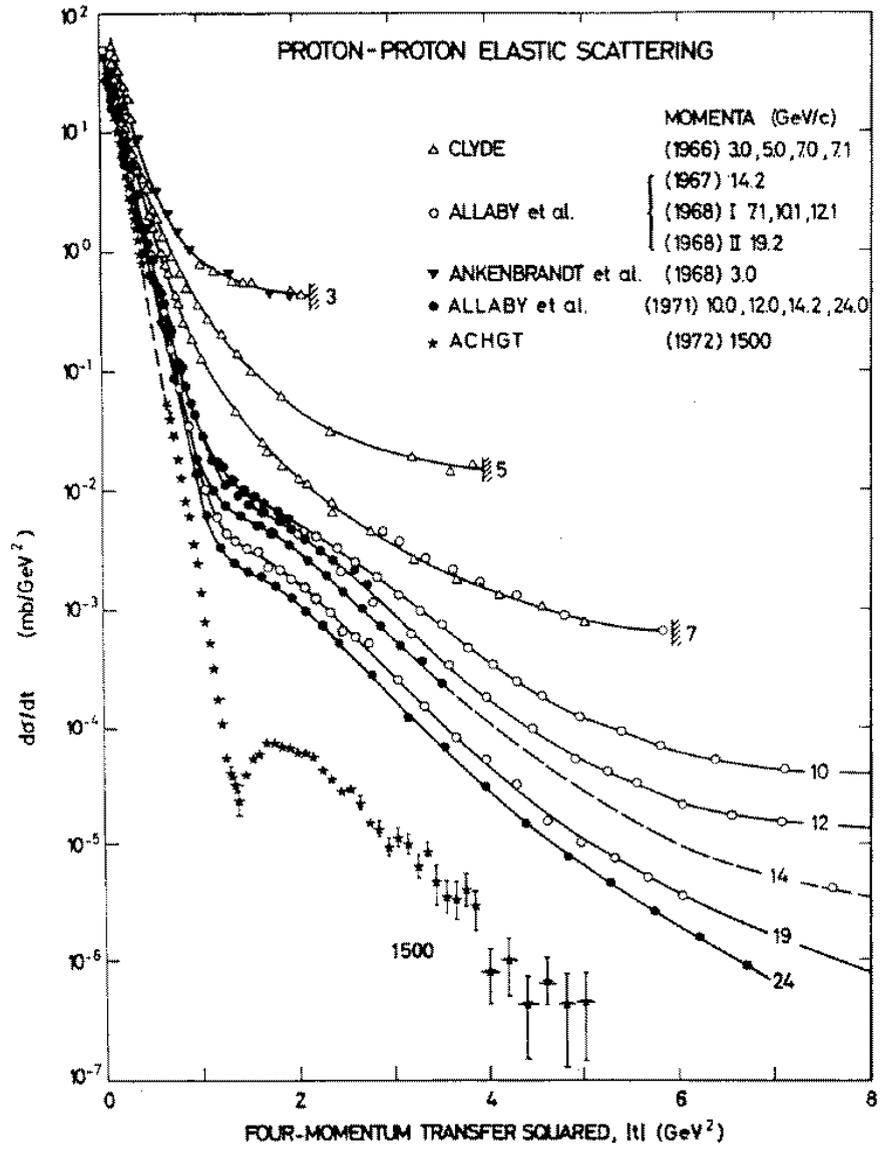


Fig. 2.1. Proton-proton elastic scattering cross section differential in t for different proton momenta (from [Gou83]).

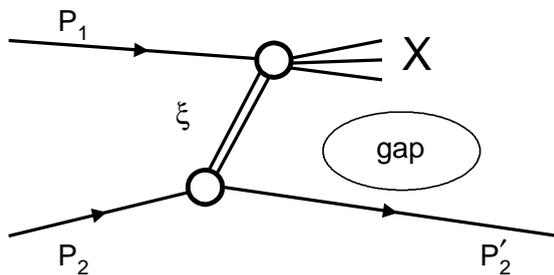


Fig. 2.2. Single diffractive dissociation process $pp \rightarrow Xp$. One proton remains intact, whereas the other proton dissociates into a system X . The two final state systems are separated by a gap due to the colourless exchange (denoted by the double line). ξ is the fractional longitudinal momentum loss of the proton remaining intact.

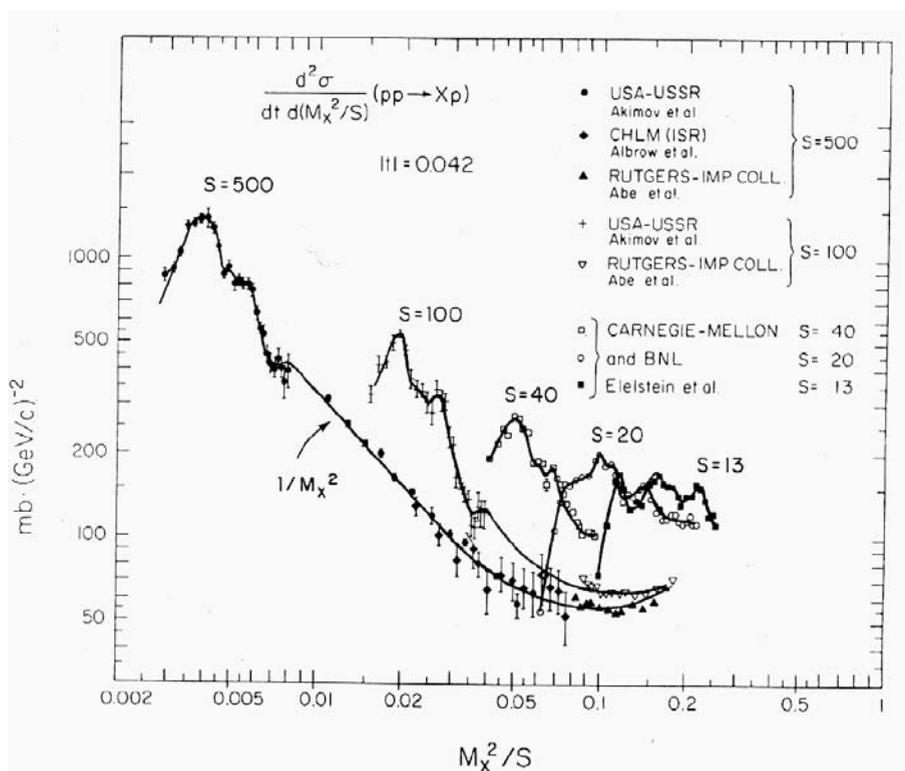


Fig. 2.3. The invariant differential cross section $\frac{d^2\sigma}{dt d(M_X^2/s)}$ for $pp \rightarrow Xp$ at $t = -0.042 \text{ GeV}^2$ plotted versus M_X^2/s for various values of s (from [Gou83]).

in which P_1 is the momentum of the excited proton and P_1/m_p is the relativistic γ factor. P_2 and P'_2 denote the momentum of the proton remaining intact before and after the interaction, respectively. With

$$\Delta P_L = P_2 - P'_2 \equiv \xi P_2,$$

and the fact that in the centre-of-mass system $P_1 = P_2$, it follows that

$$\xi < \frac{m_\pi}{m_p} = 0.15.$$

The Lorentz invariant quantity ξ is the fractional longitudinal momentum loss of the proton remaining intact. For $t \ll M_X^2$, ξ is related to the mass of the dissociation system by

$$\xi = \frac{M_X^2 - m_p^2}{s} \approx M_X^2/s.$$

The $1/\xi$ shape of $d\sigma/d\xi$ can be understood in terms of an exchanged particle with vacuum quantum numbers. Such a particle does not radiate as it traverses space, leaving a gap devoid of particles. The gap width in rapidity space¹ $\Delta\eta$, measured from the rapidity of the proton remaining intact to the rapidity of the exchanged particle, is given by [Ber87]

$$\Delta\eta \approx \ln \frac{1}{\xi}. \tag{2.4}$$

Because there is no resistance to the propagation of the exchanged particle, the cross section of diffractive dissociation is flat in $\Delta\eta$: $d\sigma/d\Delta\eta = \text{const.}$, which through Eq. (2.4) leads to

$$\frac{d\sigma}{d\xi} \propto \frac{1}{\xi}.$$

2.1.3 Total Cross Sections

Fig. 2.4 shows the total cross sections for hadron-proton and γp scattering. All cross sections exhibit a small rise with increasing centre-of-mass energies for $s > 10 \text{ GeV}^2$.

2.1.4 Regge Phenomenology

This section briefly summarizes the application of Regge theory to high energy particle physics. A thorough discussion is found in [Col77].

Particles which differ only in mass m and angular momentum J , but with otherwise equal quantum numbers, align on trajectories in the (m^2, J) plane (cf. Fig. 2.5).

The trajectories are experimentally observed to be of the form

$$\alpha(t) = \alpha(0) + \alpha' t, \tag{2.5}$$

1. In the limit of high energies, the rapidity can be approximated by the *pseudorapidity* η , which is related to the polar scattering angle θ (cf. Sec. 2.6.3).

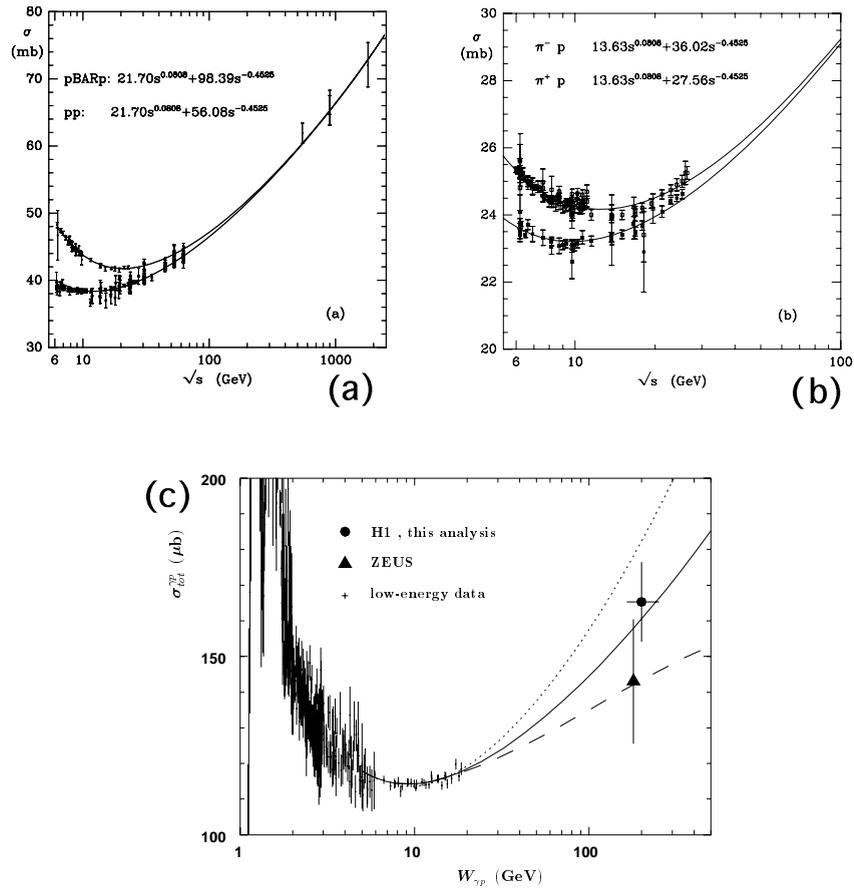


Fig. 2.4. The total cross sections for a) pp and $p\bar{p}$ scattering, b) πp scattering, and c) γp scattering as functions of the centre-of-mass energy. The solid curves are the Donnachie-Landshoff Regge theory fits (cf. Sec. 2.1.4) (from [New96]).

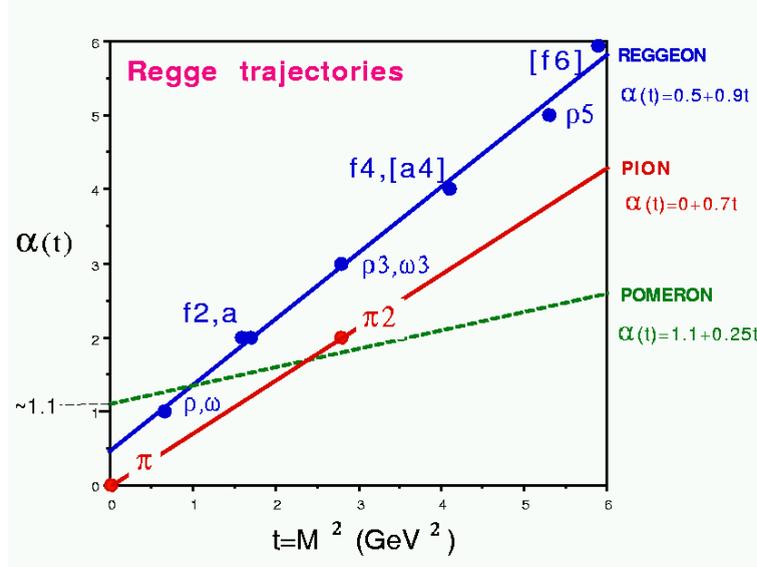


Fig. 2.5. Three Regge trajectories (from [Gou00]).

in which $t = m^2$. These lines can be extrapolated to negative squared masses t , where t then corresponds to the four momentum transfer squared of an exchanged particle. Examples are (cf. Fig. 2.5)

$$\begin{array}{lll} \text{Reggeon trajectory} & \alpha(t) = 0.5 + 0.9 t & \rho, \omega, f2, \dots \\ \text{Pion trajectory} & \alpha(t) = 0 + 0.7 t & \pi \end{array}$$

In Regge theory, hadronic interactions are described in terms of t -channel exchanges of these trajectories. In the high energy limit $s \rightarrow \infty$, $t/s \rightarrow 0$, the amplitude for the trajectory $\alpha(t)$ is given by

$$T(s, t) \propto \beta(t) \left(\frac{s}{s_0} \right)^{\alpha(t)}, \quad (2.6)$$

in which β describes the coupling of the trajectory to the external particles and s_0 is of order 1 GeV. The cross section differential in t is given by

$$\begin{aligned} \frac{d\sigma}{dt} &\propto \frac{1}{s^2} |T(s, t)|^2 \\ &\propto f(t) \left(\frac{s}{s_0} \right)^{2\alpha(t)-2}. \end{aligned} \quad (2.7)$$

From Eqs. (2.5) and (2.7) it follows that

$$\begin{aligned} \frac{d\sigma}{dt} &\propto f(t) \left(\frac{s}{s_0} \right)^{2\alpha' t} = f(t) e^{2\alpha' \ln(s/s_0) t}, \\ \frac{d\sigma}{dt} &\propto \left(\frac{d\sigma}{dt} \right)_{t=0} e^{bt}, \end{aligned} \quad (2.8)$$

with the slope parameter $b = 2\alpha' \ln(s/s_0)$. Thus, Regge theory describes the observed forward elastic scattering peak as well as its shrinkage with rising s .

The total cross section is connected to the elastic scattering forward amplitude by the optical theorem

$$\sigma_{\text{tot}} \propto \frac{1}{s} \text{Im}\{T_{\text{el}}(s, t = 0)\}$$

Because the elastic scattering amplitude is almost pure imaginary at high energies, the total cross section's dependence on s follows from Eq. (2.6):

$$\sigma_{\text{tot}} \propto s^{\alpha(0)-1}.$$

Because the total cross sections in hadron interaction rise at large s (cf. Sec. 2.1.3), this requires a trajectory with an intercept $\alpha(0) > 1$. However, the intercepts of all known meson trajectories are less than ≈ 0.5 . To describe the rising cross sections, the Pomeron trajectory was introduced. The associated particle is called pomeron. It has to be colour neutral to mediate the elastic exchange between hadrons. Donnachie and Landshoff [Don92] have fitted the measured cross sections by a combination of the reggeon and the pomeron trajectory (cf. Fig. 2.4). The obtained value for the pomeron intercept is $\alpha_P(0) = 1.08$.

The simple introduction of a trajectory with an intercept $\alpha(0) = 1 + \epsilon > 1$ leads to unitarity problems as $s \rightarrow \infty$. The power law dependence of the total cross section on s , e.g., violates the Froissart bound [Fro61]:

$$\sigma_{\text{tot}} \propto s^\epsilon > \ln^2 \frac{s}{s_0}.$$

Several other problems arise (see [Gou00] and references therein).

2.2 Diffractive Scattering

Proton-proton elastic scattering is mediated by a colourless object. Interactions related to a colourless exchange are termed 'diffractive' because of the resemblance of the pp elastic cross section differential in t and the diffraction pattern observed, when light is scattered by a circular disk.

This section introduces rapidity gap events, summarizes two of the current models of diffractive scattering, and reviews experimental results.

2.2.1 Rapidity Gaps

A colourless object does not radiate when it is accelerated. It thus leads to the formation of a gap between the scattering particles. Radiating exchanges have exponentially suppressed probabilities to produce a gap, which is related to multiplicity fluctuations in the final state particle distribution. Experimentally, diffractive events can be selected by requiring the presence of a gap between the outgoing hadron and the hadrons produced in the interaction.

2.2.2 Diffractive Parton Distributions

In [Col98] J.C. Collins proved that the cross section for diffractive deep inelastic scattering $\gamma^* p \rightarrow Xp$ can be written as convolutions of universal partonic cross sections $\hat{\sigma}^{\gamma^*i}$ with diffractive parton distributions f_i^D :

$$\frac{d^2\sigma(x, Q^2, x_{IP}, t)^{\gamma^* p \rightarrow Xp}}{dx_{IP} dt} = \sum_i \int_x^{x_{IP}} d\xi \hat{\sigma}^{\gamma^*i}(x, Q^2, \xi) f_i^D(\xi, Q^2, x_{IP}, t),$$

in which the sum runs over all quark and anti-quark flavours. f_i^D represents the probability for a parton i to emerge from within the proton under the constraint that the proton remains intact (diffraction).

2.2.3 Resolved Pomeron Model

In the Resolved Pomeron Model by Ingelman and Schlein [Ing85], diffractive scattering is mediated by a hadronic object composed of gluons and quarks. Its structure is given by parton distribution functions. The model is based on Regge factorization, which assumes that the diffractive structure function of the proton can be decomposed into a universal pomeron flux factor $f_{IP/p}(x_{IP}, t)$ and pomeron parton distribution functions f_i^{IP} :

$$f_i^D(x, Q^2, x_{IP}, t) = f_{IP/p}(x_{IP}, t) f_i^{IP}(\beta = x/x_{IP}, Q^2) \quad \text{Regge Factorization.}$$

$f_{IP/p}(x_{IP}, t)$ is the probability for a pomeron with longitudinal proton momentum fraction x_{IP} and squared mass t to be emitted by the proton. This model is implemented in the Monte Carlo generator POMPYT (cf. Sec. 2.7.2).

2.2.4 Soft Colour Interaction Model

In the Soft Colour Interaction Model by Edin, Ingelman and Rathsman [Edi96] diffraction occurs through colour rearrangements between the outgoing partons, which leave the momentum configuration unchanged. If two colour singlet states are obtained in this rearrangement process, the final state exhibits a rapidity gap. The original model contained only one free parameter, the gap formation probability, which was fixed by a fit to the measured proton diffractive structure function. This approach has been refined recently [Rat99].

2.3 Diffractive Deep Inelastic Scattering at HERA

2.3.1 Deep Inelastic Scattering

At the HERA collider, deep inelastic ep scattering (DIS) is examined. The electron emits a photon with momentum q , which interacts with a parton inside the proton. The DIS regime is characterized by $Q^2 \equiv -q^2 \gg 1 \text{ GeV}^2$.

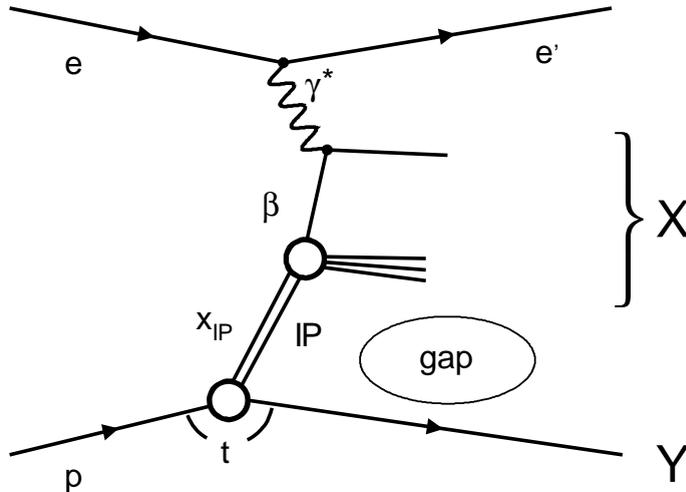


Fig. 2.6. *Inclusive DDIS process viewed in terms of the Resolved Pomeron Model. The virtual photon scatters off a parton in the pomeron with a pomeron momentum fraction β . The pomeron (\mathbb{P}) emerges from within the proton with a proton momentum fraction $x_{\mathbb{P}}$. A gap is observed between the systems X and Y .*

In about 10 % of all deep inelastic events a gap is observed between the outgoing system belonging to the proton and the hadronic system produced in the interaction. Fig. 2.6 shows the inclusive diffractive deep inelastic scattering process in terms of the Resolved Pomeron Model. The virtual photon scatters off a parton in the pomeron with a pomeron momentum fraction β . The pomeron (\mathbb{P}) emerges from within the proton with a proton momentum fraction $x_{\mathbb{P}}$. The proton remains intact or dissociates into a system Y of low mass and escapes through the beam pipe. A gap is observed between the outgoing proton and the hadrons produced in the interaction (system X). The square of the momentum transferred at the proton vertex is labelled t .

2.3.2 Diffractive Structure Function of the Proton

In inclusive diffractive deep inelastic scattering (DDIS), the diffractive structure function $F_2^{D(3)}$ of the proton was measured at HERA [Adl97]. The diffractive structure function of the proton is defined in an analogous way to the ordinary proton structure function. In principle, it depends on five independent variables characterizing the scattering process:

$$\frac{d^5 \sigma_{ep \rightarrow eXY}}{dx_{\mathbb{P}} d\beta dQ^2 dM_Y dt} = \frac{4\pi\alpha_{\text{em}}^2}{\beta^2 Q^4} \left(1 - y + \frac{y^2}{2(1 + R^{D(5)})} \right) F_2^{D(5)}.$$

$R^{D(5)}$ is the ratio of longitudinal photon to transverse photon cross sections. It was neglected in the analysis. The Y system was not accessible, so the variables M_Y and

t were implicitly integrated over, leaving a three-fold differential cross section and the structure function $F_2^{D(3)}(x_{\mathbb{P}}, \beta, Q^2)$:

$$\frac{d^3\sigma_{ep\rightarrow eXY}}{dx_{\mathbb{P}}d\beta dQ^2} = \frac{4\pi\alpha_{\text{em}}^2}{\beta^2 Q^4} \left(1 - y + \frac{y^2}{2}\right) F_2^{D(3)}.$$

Assuming Regge factorization, $F_2^{D(3)}$ can be decomposed into a flux factor and the structure function of the pomeron:

$$F_2^{D(3)}(x_{\mathbb{P}}, \beta, Q^2) = f_{\mathbb{P}}(x_{\mathbb{P}}) F_2^{\mathbb{P}}(\beta, Q^2).$$

$f_{\mathbb{P}}(x_{\mathbb{P}})$ is the probability that a pomeron with momentum fraction $x_{\mathbb{P}}$ is emitted by the proton. The H1 measurement of $F_2^{D(3)}$ indicated a breaking of this factorization. However, by describing the processes as a sum of reggeon and pomeron exchanges, factorization could be reestablished:

$$F_2^{D(4)}(x_{\mathbb{P}}, \beta, Q^2, t) = f_{\mathbb{P}}(x_{\mathbb{P}}, t) F_2^{\mathbb{P}}(\beta, Q^2) + f_{\mathbb{R}}(x_{\mathbb{P}}, t) F_2^{\mathbb{R}}(\beta, Q^2).$$

For the flux factors, a Regge-motivated parameterization was used:

$$f(x_{\mathbb{P}}, t) = \frac{1}{x_{\mathbb{P}}^{2\alpha(t)-1}} C e^{Bt}.$$

The pomeron intercept found in the analysis is higher than the value from the Donnachie-Landshoff fit: $\alpha_{\mathbb{P}}(0) = 1.20 \pm 0.04$.

2.3.3 Pomeron Parton Density Functions

The virtual photon only couples to the quarks in the proton, because gluons do not carry electric charge. The diffractive cross section therefore contains only quark contributions. However, from the scaling violation of the measured pomeron quark structure function, the gluon density in the pomeron can be extracted.

The quark and antiquark densities q_i and \bar{q}_i are related to the structure function by

$$F_2^{\mathbb{P}}(\beta, Q^2) = \sum_i e_i^2 \beta (q_i(\beta, Q^2) + \bar{q}_i(\beta, Q^2)),$$

in which the sum runs over all quark flavours, and e denotes the quark charge in units of the proton charge. Because quarks can emit gluons and gluons can create quark-antiquark pairs as well as split into several gluons, the parton density functions are not constant. In first order QCD, they evolve according to the DGLAP evolution equations, depending on the scale Q^2 and the parton momentum β . The parton distributions were parameterized at a starting scale $Q_0^2 = 3 \text{ GeV}^2$ and fitted to the data.

Fig. 2.7 shows the obtained pomeron parton density functions for the gluons and the light quarks u, d, s as functions of the momentum fraction carried by the partons. About 80% of the pomeron momentum is carried by gluons. Two different parameterizations are shown, which both give an adequate description of the data: the ‘flat gluon’ fit 2 and the ‘hard gluon’ fit 3.

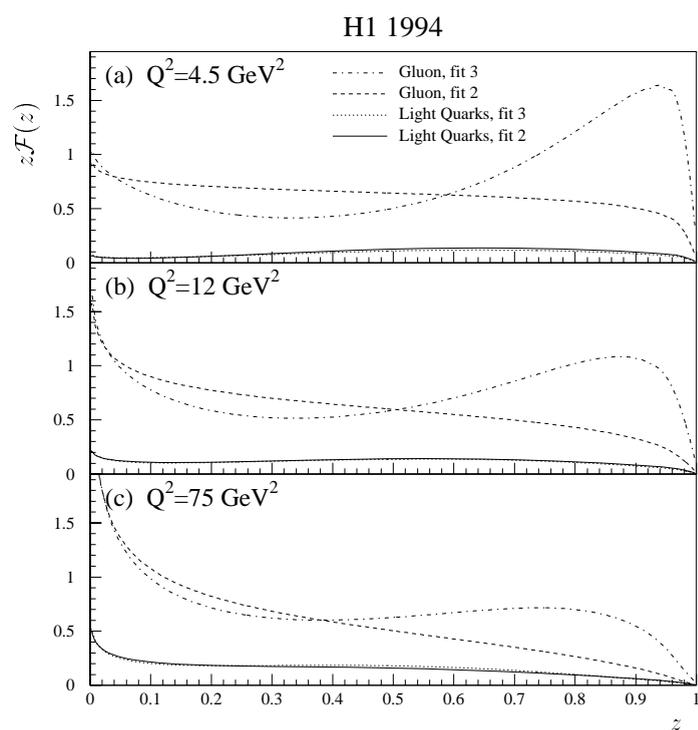


Fig. 2.7. Pomeron parton density functions obtained by H1 in a QCD analysis of $F_2^{D(3)}$. The distributions are shown as functions of the fractional parton momentum z at three different scales Q^2 . The functions are normalized to represent the parton distributions multiplied by the flux factor at $x_{\mathbb{P}} = 0.003$ (from [Adl97]).

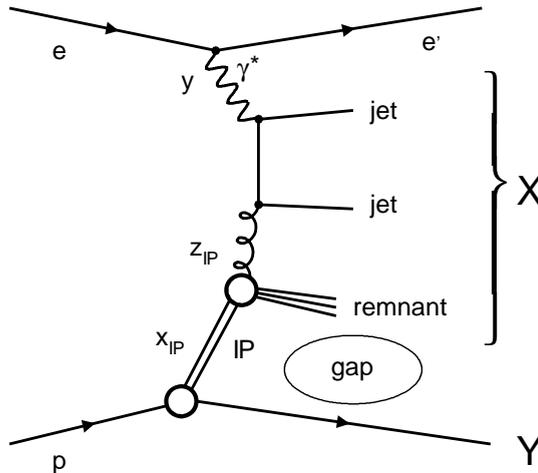


Fig. 2.8. DDIS dijet boson gluon fusion process viewed in terms of the Resolved Pomeron Model. The virtual photon γ^* probes the gluon content of the pomeron.

2.3.4 Diffractive DIS Dijets

In inclusive DIS measurements the diffractive gluon density in the proton can be extracted only indirectly from the scaling violation observed in the diffractive structure function.

The *boson-gluon fusion* process (BGF) (cf. Fig. 2.8), however, is directly sensitive to the gluon density. It leads to a quark-antiquark pair. These quarks can be observed as two jets if they emerge with high transverse momenta.

The crossed process of QCD compton scattering (QCDC) is in principle equally likely to occur, but from the inclusive measurement it is known that the diffractive structure function of the proton is dominated by gluons. Therefore, the QCDC process is suppressed in diffractive dijet events. Some of the conclusions from an analysis of dijets in diffractive DIS [Sch00] are the following. The Resolved Pomeron Model can describe the data within the achieved experimental accuracy if the H1 QCD fit 2 parton distributions are assumed for the pomeron. The hard gluon fit 3 is not suited to describe the data. The SCI model cannot reproduce the normalization and the shape of the data at the same time.

2.4 Diffractive $p\bar{p}$ Scattering at the Tevatron

At the Fermilab Tevatron $p\bar{p}$ collider, diffractive dijets with an intact outgoing (*leading*) antiproton were studied at a centre-of-mass energy of 1800 GeV [Aff00]. The diffractive structure function of the antiproton was measured and compared to predictions based on the pomeron parton densities determined in DDIS at HERA. The result is shown in Fig. 2.9. The CDF measurement differs from the predictions both in shape and normalization. The discrepancy in the normalization amounts to one order of magnitude. A

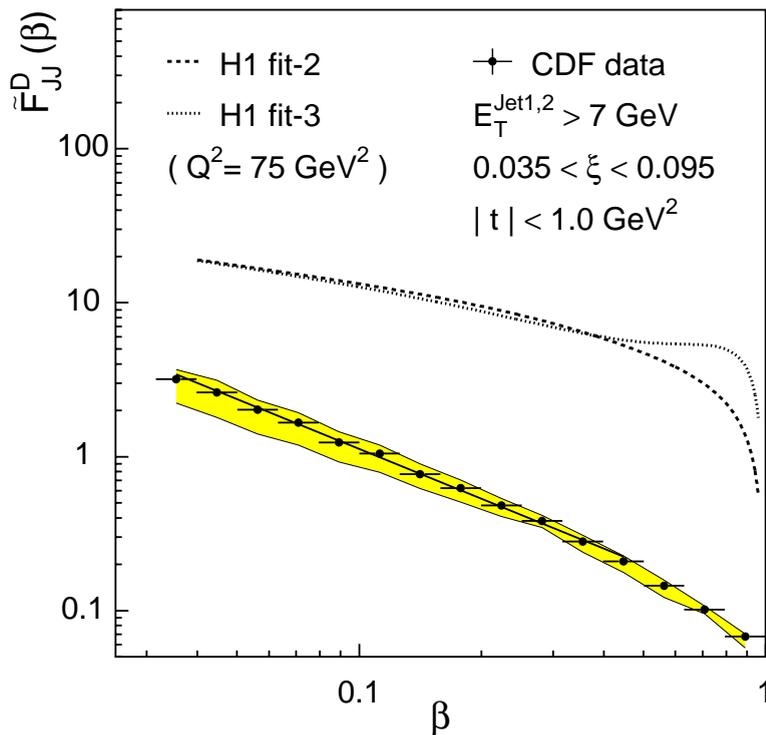


Fig. 2.9. The diffractive structure function of the antiproton as measured by the CDF Collaboration (from [Aff00]). The lower (upper) boundary of the filled band represents the data distribution obtained using only the two leading jets (up to four jets of $E_T > 5$ GeV) in evaluating β . The additional systematic uncertainty of the data is $\pm 25\%$. The straight line is a fit of the form β^{-n} . The expectations from the H1 fits 2 (3) are the dashed (dotted) lines.

similar discrepancy was observed [Abe97] in comparing diffractive W -boson and dijet production rates at the Tevatron with expectations based on ZEUS results [Der95] obtained from DDIS and dijet photoproduction at HERA. The discrepancy is testimony to the breakdown of factorization in hard hadron-hadron diffractive scattering.

2.5 Diffractive Photoproduction at HERA

In contrast to DIS, where the photon emitted by the electron is highly virtual, the regime of photoproduction is characterized by $Q^2 \approx 0$, i.e., the photon is approximately on its mass shell (*real* photon). The photon can fluctuate into a hadronic system composed of quarks and gluons, from which a parton emerges and takes part in the subprocess with a parton from the proton side (*resolved* photon process). The photon can also couple directly to a parton from the proton side.

An observable quantity exists, which can distinguish between direct and resolved processes: x_γ denotes the photon momentum fraction of the particle entering the subprocess from the photon side. For resolved processes x_γ is less than 1.

By selecting events in a specific x_γ range, different subprocesses can be studied in photoproduction. At large x_γ values, the photon is dominated by quarks, whereas in the low x_γ regime, the gluon content is dominant. Processes with a gluon entering the subprocess from the photon side can therefore be enhanced by selecting events with low x_γ . In these processes, additional colour from the photon side is involved in the subprocess. This affects soft colour neutralization models, in which the gap probability depends on the number of colour states accessible to the subsystem. The Resolved Pomeron Model is unaffected by additional colour. The analysis of resolved photoproduction events can therefore contribute to the understanding of diffraction.

2.6 Kinematics of Dijets in Diffractive Photoproduction

This section defines the kinematical variables used in the analysis and explains their reconstruction procedures.

2.6.1 Overview

Fig. 2.6.1 illustrates a resolved photon diffractive dijet process in terms of the Resolved Pomeron Model. The beam electron e emits a photon γ , which fluctuates into a hadronic system, from which a single parton emerges and takes part in the hard subprocess with a parton appearing from within the pomeron. This interaction leads to the formation of two final state jets of large transverse momenta. From the photon and the pomeron two remnant systems are present. The photon-pomeron system is labelled X . The pomeron (P) is emitted by the beam proton p , which then forms the system Y . The systems X and Y are separated by a gap.

These events leave the following signature in the detector:

- an electron scattered by a small angle,
- two jets with high transverse momentum,
- a region devoid of hadronic activity between the detected hadronic final state (system X) and the beam pipe, through which the system Y escapes.

2.6.2 General Description of the Processes

The data of this analysis were recorded from electron proton head-on collisions, i.e., the initial momenta pointed in opposite directions. The coordinate system's positive z axis is chosen to coincide with the direction of the incident proton's momentum $P = (E_P, 0, 0, P_z)$.

Electron Side

The incoming electron emits a collinear photon of momentum $q \approx (E_\gamma, 0, 0, -E_\gamma)$. This process is termed 'photoproduction.' The real photon ($-q^2 \equiv Q^2 \approx 0$) takes then part in

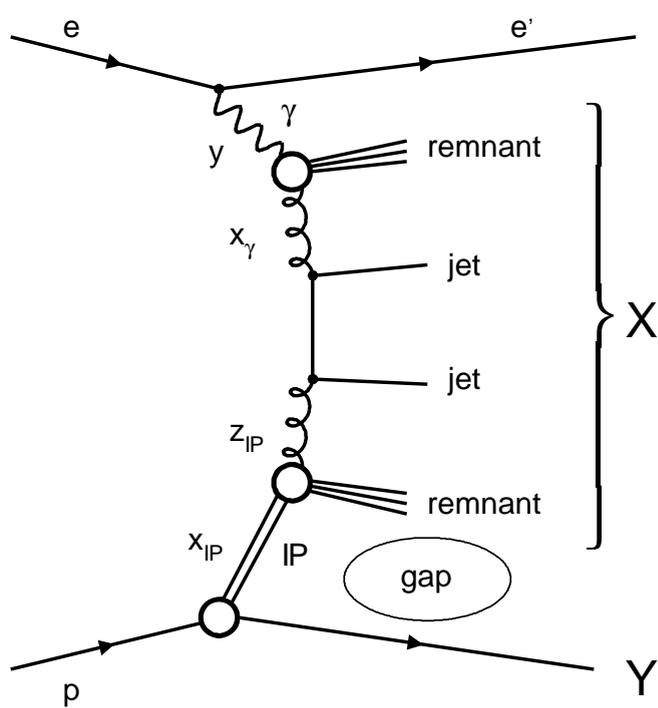


Fig. 2.10. Diffractive dijet process in resolved photoproduction in terms of the Resolved Pomeron Model.

a γp collision, in contrast to deep-inelastic ep scattering, when the proton is probed with a highly virtual photon γ^* ($Q^2 \gg 1 \text{ GeV}^2$).

The inelasticity y denotes the energy fraction of the electron transferred to the photon. With $s \approx 4 E_p E_e$ being the squared centre-of-mass energy of the electron-proton system, the centre-of-mass energy of the photon-proton system is given by $W = \sqrt{ys}$.

Because of the uncertainty principle, for the short duration of the interaction the photon can fluctuate in a hadronic object composed of quarks and gluons. The probability to find a parton with momentum fraction $x_\gamma < 1$ ('resolved photon process') in the photon is given by the photon structure function $F_2^\gamma(\mu^2, x_\gamma)$, in which μ^2 is the scale. For $x_\gamma = 1$ the photon itself enters the subprocess ('direct photon process').

Proton Side

The incoming proton with momentum P is quasi-elastically scattered into a system Y of momentum P' . Y is either a proton or a low-mass proton excitation. The squared momentum transferred at the proton vertex is given by $t = (P - P')^2$. The Feynman- x $x_F = P'_z/P_z$ denotes the longitudinal momentum fraction carried by Y . Diffractive events are characterized by $1 - x_F < 0.1$. Then the longitudinal momentum transferred to Y is small, and even a small transferred transverse momentum well separates the systems X and Y in space ('rapidity gap'). The mass of the system X is given by $M_X = \sqrt{(1 - x_F)ys}$.

In the Resolved Pomeron Model a colour singlet state, the pomeron, is emitted by the proton. The pomeron carries the proton momentum fraction $x_P = 1 - x_F$, and t is its squared mass. A parton from within the pomeron takes part in the hard subprocess. The pomeron parton density functions give the probability for a parton to emerge with a momentum fraction z_P . The pomeron cannot enter the subprocess by itself, there are no 'direct pomeron processes.'

Hard Subprocess

The dijet final state results from a hard ' $2 \rightarrow 2$ process.' Two incident partons interact, producing two partons with large transverse momenta \hat{p}_T ($> 1 \text{ GeV}$). Fragmentation then leads to the formation of two jets. In this analysis the kinematical variables of the jet with the largest p_T are denoted by a subscript 1, whereas a subscript 2 is used for the second largest p_T jet. The mass of the jet system is labelled M_{12} .

Remnant Interactions

In direct photon processes, the pomeron remnant can interact with the Y system. In resolved photon processes, the remnants of the photon and pomeron systems can undergo interactions with one another or with the Y system.

2.6.3 Kinematical Reconstruction

With the H1 experiment the following quantities are directly measurable (cf. Sec. 3.2).

- E'_e :
the scattered electron's energy can be measured in a separate small angle electron detector.
- **system X** :
the four-vectors of the objects of the system X can be determined.
- **jet system**:
jets are identified within the X system as large amount of hadronic energy within a small angular region. The four-vectors of the jets can be reconstructed.
- (M_Y) :
the system Y is not directly detected, but its mass is restricted to less than 1.6 GeV by requiring the absence of energy around the beam pipe.

From these observables the kinematical variables were reconstructed as follows.

The inelasticity is given by

$$\boxed{y = \frac{E_\gamma}{E_e} = 1 - \frac{E_{e'}}{E_e}}. \quad (2.9)$$

x_γ and z_{IP} can be calculated from the jet information. Let P_γ denote the momentum of the parton from the photon and P_{IP} be the momentum of the parton from the pomeron side. Then the momentum conservation of the hard subprocess reads

$$P_\gamma + P_{IP} = P_1 + P_2. \quad (2.10)$$

P_γ , P_{IP} and IP are related to their mother particle momenta via x_γ , z_{IP} and x_{IP} , respectively:

$$P_\gamma = x_\gamma q + P_\gamma^T, \quad (2.11)$$

$$P_{IP} = z_{IP} IP + P_{IP}^T, \quad (2.12)$$

$$IP = x_{IP} P + IP^T, \quad (2.13)$$

in which the script T denotes purely transversal quantities of the form $(0, *, *, 0)$. Multiplying Eq. (2.10) by the longitudinal P yields

$$x_\gamma q \cdot P + z_{IP} x_{IP} P^2 = (P_1 + P_2) \cdot P.$$

Neglecting terms $m_p^2/E_p^2 = 1.3 \cdot 10^{-6} \ll 1$ and² $\frac{x_{IP} z_{IP} m_p^2}{x_\gamma 2 E_\gamma E_p} \ll 1$ it follows that

$$x_\gamma 2 E_\gamma E_p = E_p \sum_{\text{jets}} (E - p_z),$$

2. In a diffractive MC corresponding to a luminosity of 10 pb^{-1} this ratio was less than 0.25 ‰ for all events.

$$\boxed{x_\gamma = \frac{\sum_{\text{jets}}(E - p_z)}{2 y E_e}}. \quad (2.14)$$

Similarly, multiplying Eq. (2.10) by q leads to

$$\boxed{z_{\mathbb{P}} = \frac{\sum_{\text{jets}}(E + p_z)}{2 x_{\mathbb{P}} E_p}}. \quad (2.15)$$

In the case when the pomeron is collinear to the proton, such that

$$R \equiv \frac{\mathbb{P}_T^2 - t}{(x_{\mathbb{P}} E_p)^2} \ll 1, \quad (2.16)$$

then $\mathbb{P}_0 = x_{\mathbb{P}} E_p$, and $x_{\mathbb{P}}$ can be reconstructed from the X system:

$$\begin{aligned} E_\gamma \sum_X (E + p_z) &= q \cdot P_X, \\ &= q \cdot (q + \mathbb{P}), \\ &= E_\gamma (\mathbb{P}_0 + x_{\mathbb{P}} E_p), \end{aligned}$$

$$\boxed{x_{\mathbb{P}} = \frac{\sum_X (E + p_z)}{2 E_p}}. \quad (2.17)$$

Condition (2.16) is well full-filled for the events of this analysis.³

From Eqs. 2.11, 2.12 and 2.13 it is noted that $x_\gamma, z_{\mathbb{P}}$ and $x_{\mathbb{P}}$ do not fully characterize the corresponding particle's momentum.

The directions of the particles are described by the azimuthal angle Φ and the polar angle θ . The latter is measured with respect to the positive z axis. Unlike Φ , θ is not invariant under Lorentz boosts along z . The *rapidity* y' is defined as

$$y' \equiv \frac{1}{2} \ln \frac{E + p_z}{E - p_z}.$$

Intervals in y' are invariant under boosts along z . The *pseudorapidity* η is defined as

$$\eta \equiv \frac{1}{2} \ln \frac{p + p_z}{p - p_z} = -\ln \left(\tan \frac{\theta}{2} \right). \quad (2.18)$$

In the limit of large energies, when $E \approx |\vec{p}| \equiv p$, η is a good approximation of y' .

The difference in η of the two jets is related to the scattering angle $\hat{\theta}$ in the centre-of-mass system of the partons [Kau98]:

$$\begin{aligned} \Delta\eta &\equiv \eta_1 - \eta_2 = -2 \ln(\tan(\hat{\theta}/2)), \\ \cos(\hat{\theta}) &= \tanh\left(\frac{\Delta\eta}{2}\right), \end{aligned}$$

which for $|\Delta\eta| < 1$ can be approximated by $\Delta\eta \approx 2 \cos(\hat{\theta})$.

The cross section is measured differentially in the following mean jet variables:

$$\langle p_T^{\text{jet}} \rangle \equiv \frac{1}{2} (p_T^{(1)} + p_T^{(2)}), \quad (2.19)$$

$$\langle \eta_{\text{jet}} \rangle \equiv \frac{1}{2} (\eta_1 + \eta_2). \quad (2.20)$$

3. For 95 % of the events in the MC mentioned in the previous footnote $R < 1\%$ and for 71 % of them $R < 1\%$.

2.7 Monte Carlo Generators

In this analysis, three Monte Carlo generators are used to correct the data for detector effects. Non-diffractive background is simulated with PYTHIA. The diffractive photoproduction events are generated with POMPYT, and DIFFVM is used to simulate proton dissociation. The measured cross sections are compared to predictions of the Resolved Pomeron Model, implemented in POMPYT.

2.7.1 PYTHIA

The PYTHIA generator [Sjö86] is based on leading order (LO) matrix elements for hard parton-parton scattering. The probabilities for the partons to emerge from the photon and the proton is given by parton distribution functions. In this analysis, the GRV parameterizations [Glü92] in LO are used for both the photon and the proton.

PYTHIA is used to subtract non-diffractive background from the data event distributions.

2.7.2 POMPYT

The Resolved Pomeron Model is implemented in the MC program POMPYT [Bru93], which is based on the PYTHIA generator. POMPYT simulates hard diffractive scattering processes. The parton distribution functions of the pomeron can be chosen freely. A variety of parameterizations is available for the pomeron flux factor.

The data cross sections are compared to the Resolved Pomeron Model with contributions from pomeron and reggeon exchanges. The H1 QCD fit 2 result is used for the pomeron structure function. The pomeron and reggeon flux are implemented as they were used in this fit.

For the correction of the data for detector effects, the ‘hard gluon’ fit 3 is used, because no fit 2 MC is available on detector level.

2.7.3 DIFFVM

The Monte Carlo generator DIFFVM [Lis93] simulates diffractive vector meson production. Unlike PYTHIA and POMPYT, it simulates proton dissociation. DIFFVM is used to correct the data for migration effect due to this process, by assuming that the dissociation is independent from the rest of the interaction.

2.7.4 Hadronization

The cross sections are presented as functions of variables, which are reconstructed at the level of stable hadrons. Stable hadrons are obtained from the partons through the process of fragmentation, in which colour singlet configurations and strings are resolved and by subsequent decay of resonances. This hadronization process is not calculable in perturbative QCD, because the energy of the initial hard partons is split up further and

further ending at a scale $Q \approx m_{\text{hadron}}$. There exist phenomenological models, however, which parameterize the process and are tuned to describe experimental data. For the Monte Carlo events in this analysis the program JETSET [Sjö86] was used. It is based on the LUND string fragmentation model [And83].

Experiment

At the DESY facility¹ in Hamburg, Germany, the earth's only lepton hadron collider HERA² is located. Since the end of 1991, electrons (or positrons³) are scattered off protons at a centre-of-mass energy of 300 GeV. The present analysis is concerned with data obtained in 1996 by the H1 experiment, one of four large scale detectors grouped around HERA.

This chapter briefly introduces the collider and gives a description of the H1 detector and its components, which are most important for this analysis.

3.1 HERA

Fig. 3.1a shows a diagrammatic view of the HERA collider. Electrons and protons are stored in two separate accelerators, HERA-e and HERA-p, respectively, with circumferences of 6.4 km. The particles are not continuously distributed along the ring but grouped in bunches. These packets are accelerated by electromagnetic fields of high frequency mostly on the straight sections. Conventional dipole magnets with field strengths of 0.17 T bend the electron beam, whereas for the proton beam superconducting magnets with a strength of up to 4.5 T are used.

After electron energies of 27.5 GeV and proton energies of 820 GeV have been reached, the beams are crossed in two interaction zones in halls North and South at a centre-of-

1. Deutsches Elektronen-Synchrotron.

2. Hadron-Elektron-Ring-Anlage.

3. Throughout this thesis, the word 'electron' will be used as a synonym for both electrons and positrons.

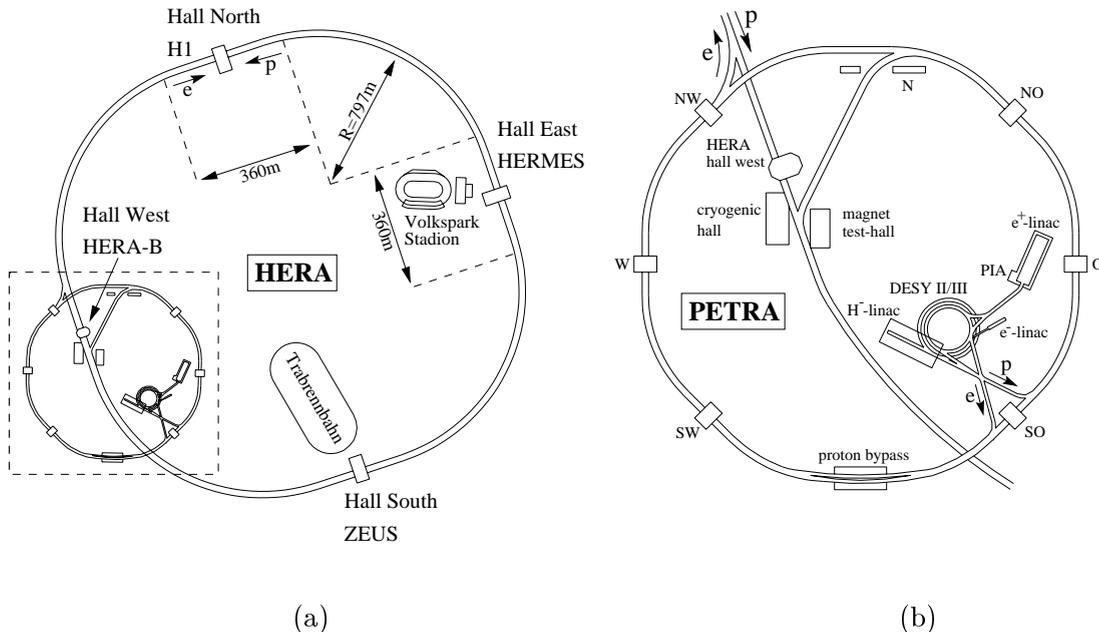


Fig. 3.1. HERA (a) and its pre-accelerators (b).

mass energy of 300 GeV. The 180 bunches in the electron and proton beam cross each other with a frequency of 10^7 Hz, corresponding to 100 ns between two crossings.

Pre-Acceleration

Before being filled into HERA, the particles undergo several pre-acceleration steps (Fig. 3.1b). Electrons emerging from a LINAC⁴ at energies of 450 MeV are speeded up to 7.5 GeV in DESY II and then stored in PETRA II. After 60 electron bunches have been accumulated, they are accelerated to 12 GeV and injected into HERA-e. To produce free protons, negatively charged hydrogen ions of 50 MeV energy are shot onto a thin foil, which strips off the electrons. The remaining protons are accelerated to 7.5 GeV in DESY III and to 40 GeV in PETRA II before being injected into HERA-p.

Luminosity

The interaction rate is determined by the luminosity \mathcal{L} . It calculates from beam parameters as

$$\mathcal{L} = \frac{\nu n_b n_e n_p}{A} \approx 10^{31} \text{ cm}^{-2} \text{ s}^{-1} = 10 \mu\text{b}^{-1} \text{ s}^{-1}, \quad (3.1)$$

with

$$\nu \quad \text{revolution frequency } (5 \cdot 10^5 \text{ Hz})$$

4. Linear Accelerator.

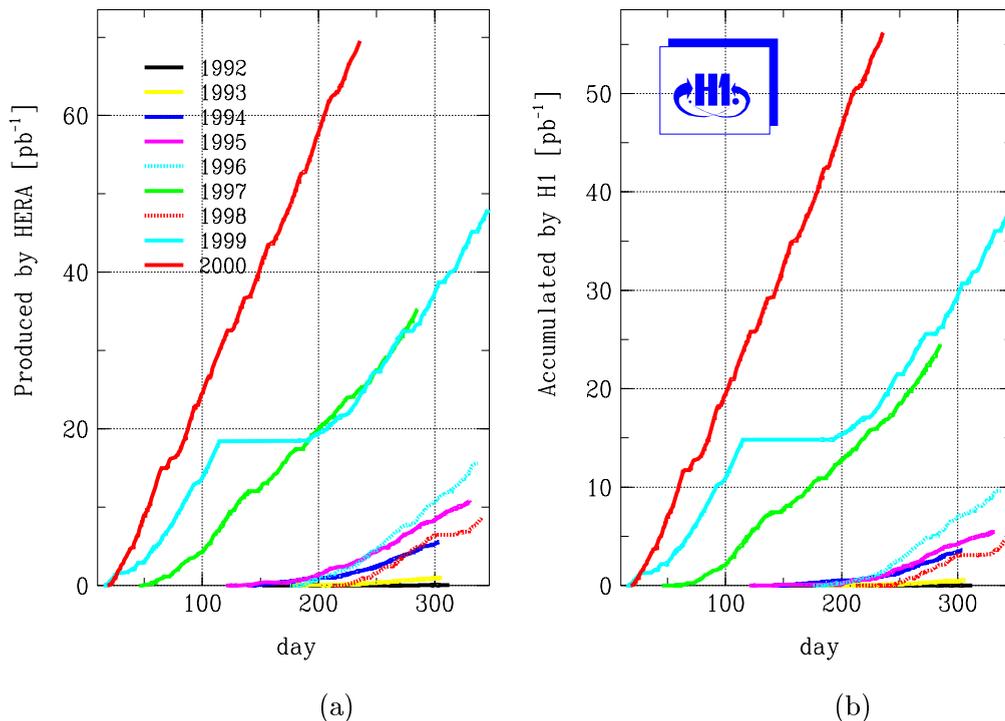


Fig. 3.2. HERA (a) and H1 (b) integrated luminosities shown separately for every year of operation.

- n_b number of bunches (180)
- n_e number of electrons per bunch (10^{10} – 10^{11})
- n_p number of protons per bunch (10^{10} – 10^{11})
- A transverse extension of the interaction region (0.17 mm^2)

Given in braces are the values for the year 1996.

Proportional to the amount of data collected at a collider is the integrated luminosity

L :

$$L = \int \mathcal{L}(t) dt. \quad (3.2)$$

Fig. 3.2a displays the integrated luminosity delivered by HERA for each of its years of service; the data volume actually recorded by the H1 experiment is shown in Fig. 3.2b. The continuous gain of knowledge about the HERA machine made it possible to achieve a better performance every year. By the end of 2000, H1 has taken more than 100 pb^{-1} of data.

HERA Physics Programme

The main aspects of particle physics research done at HERA are tests of the standard model and the search for physics beyond it.

The areas covered by the multipurpose detectors H1 and ZEUS contain

- precision measurements of the proton structure functions,
- search for substructures of quarks and leptons,
- heavy flavour production mechanisms,
- the structure of the photon,
- diffractive phenomena.

In halls West and East two more experiments use the HERA beams. The HERA-B experiment studies CP violation in B meson decays. It uses the HERA's proton beam on a fixed target. HERMES makes use of the electron beam to measure the spin structure functions of the proton and neutron. More information on HERA can be obtained from [HER81].

3.2 H1 Detector

The central detector is diagrammatically shown in Fig. 3.3. It has a mass of 2800 t at a size of $12 \times 10 \times 15$ m³. With electrons coming in from the left and protons from the right side, the interaction point is located at the centre (small mark near 2). The H1 coordinate system defines the positive z axis as the direction of the proton beam (forward direction), x pointing to the centre of the ring, and y pointing upwards. The origin lies in the centre of the H1 detector.

Because of the different beam energies, the final state is not distributed symmetrically with respect to the interaction point; instead it is boosted in the forward direction. Therefore the detector has a finer granularity in this region.

Detector Components

A complete description of the detector can be found in [Det96]. Here, only the components most relevant for the analysis are introduced.

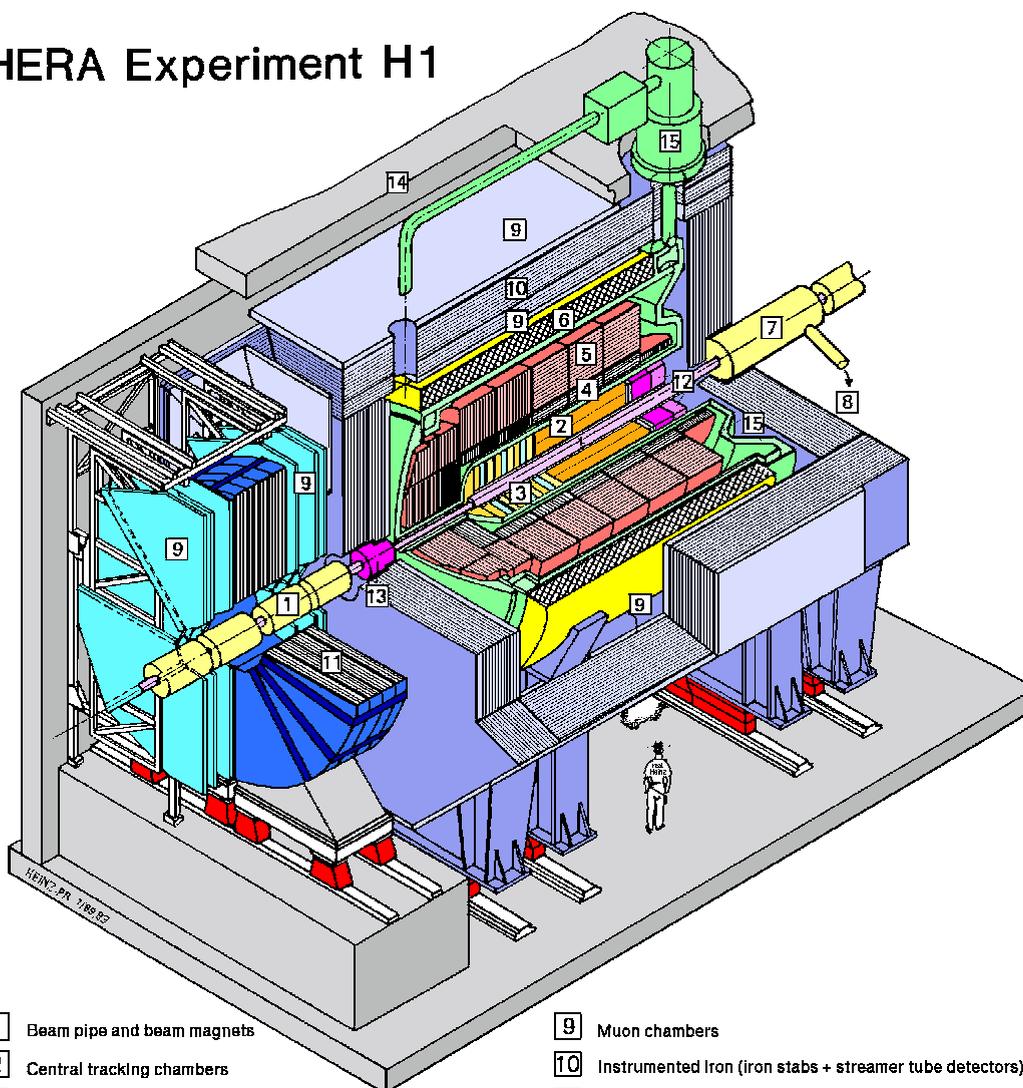
- **Magnetic Field**

The superconducting coil 6 produces a solenoidal magnetic field of strength 1.16 T parallel to the beam axis. Charged particles travelling in the perpendicular $x - y$ plane are subjected to the Lorentz force and their paths get curved.

- **Tracking System**

In detecting charged particles at different points in space, their trajectories can be reconstructed, the curvature giving the momentum and charge (2).

HERA Experiment H1



- | | |
|----------------------------------------------------|--------------------------------------------------------------------|
| 1 Beam pipe and beam magnets | 9 Muon chambers |
| 2 Central tracking chambers | 10 Instrumented Iron (iron stabs + streamer tube detectors) |
| 3 Forward tracking and Transition radiators | 11 Muon toroid magnet |
| 4 Electromagnetic Calorimeter (lead) | } Liquid Argon |
| 5 Hadronic Calorimeter (stainless steel) | |
| 6 Superconducting coil (1.2T) | 12 Warm electromagnetic calorimeter |
| 7 Compensating magnet | 13 Plug calorimeter (Cu, Si) |
| 8 Helium cryogenics | 14 Concrete shielding |
| | 15 Liquid Argon cryostat |

Fig. 3.3. The central H1 detector.

- **Liquid Argon Calorimeter (LAr)**

A calorimeter measures the energy deposited by particles. If a particle is fully absorbed in the calorimeter, its former kinetic energy is equal to the total energy deposition.

In the H1 experiment the main calorimeter is a sandwich type calorimeter, alternately composed of absorber plates and liquid argon as the active detector material. The argon is ionized by shower particles created in the absorber plates by the incident particle. The number of created ion-electron pairs is proportional to the particle's energy. The electrons are collected on electrodes and a signal proportional to the electrical charge is read out. Because the ionization process is of statistical nature, the absolute energy resolution is proportional to \sqrt{E} .

The LAr consists of an inner, electromagnetic part [4] with lead absorber plates corresponding to 20–30 radiation lengths with a relative energy resolution $\sigma_E/E = 11\%/\sqrt{E/\text{GeV}}$ and an outer hadronic part [5] with stainless steel plates amounting to 4.5–7 interaction lengths with a relative resolution of $50\%/\sqrt{E/\text{GeV}}$. The energy calibration has an uncertainty of 5%, which has to be added for both parts. The LAr covers the range $3.6 > \eta > -1.4$.

- **Backward Calorimeter SPACAL**

The lead/scintillating fibre calorimeter SPACAL ('spaghetti calorimeter') [12] covers the backward range $-1.42 > \eta > -3.82$. The energy resolution is $7\%/\sqrt{E/\text{GeV}}$ ([Nic96]).

- **Forward Muon Detector (FMD)**

The FMD is placed outside of the massive iron yoke, having the main purpose of identifying muons from a collision event. However, it can also be reached by particles scattered by collimators around the beam pipe. The detector consists of six drift chambers [9], 3 of them being located behind a toroidal magnet [11]. The acceptance region is $2.9 > \eta > 1.4$ with a relative energy resolution of 24–36 %.

- **Proton Remnant Tagger (PRT)**

Consisting of seven scintillator layers, this lead-shielded detector is used to detect activity in the range $7 > \eta > 5.1$. It is positioned at $z = 26$ m in the HERA tunnel.

- **Electron Detector (ET33)**

At $z = -33$ m a Čerenkov calorimeter is located, the 'electron tagger' (Fig. 3.4). It has an acceptance for electrons scattered by less than 5 mrad, with energies between 5.5 GeV and 22 GeV. This translates into an upper limit of 0.01 GeV^2 for the negative squared momentum transfer Q^2 and an inelasticity range of $0.2 \leq y \leq 0.8$.

- **Photon Detector (PD)**

Together with the ET, the photon detector at $z = -103$ m forms the luminosity system (Fig. 3.4). It is a Čerenkov calorimeter with photomultiplier read-out.

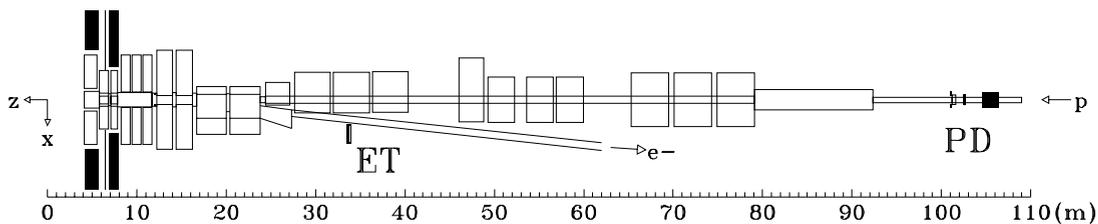


Fig. 3.4. *The H1 luminosity system. The small angle electron detector (ET) is located upstream at $z = -33$ m. The photon detector (PD) is placed at $z = -103$ m*

Data Acquisition and Trigger System

The probability for an interaction per bunch crossing is of order 10^{-3} [Det96]. Therefore, from the rate of 10^7 bunch crossings per second results a collision frequency of 10^4 Hz, dominated by background processes. Physically relevant events are selected by a hardware trigger system. It analyzes patterns of signals coming from the various detector components.

The trigger system is divided into five levels L1–L5. Based on subtriggers, L1 decides within $2 \mu\text{s}$ whether an event is rejected or kept. L1 is fully pipelined and therefore dead-time free. If at least one subtrigger is activated, the event is passed on to L2 for further examination. Typically, the L1 *keep signal* is sent at a rate of 50 Hz. For L2 the pipelines storing the full event information have to be stopped and read out. Based on correlations between the subtriggers, L2 gives a decision within $20 \mu\text{s}$. If the event is not accepted by L2, the read-out is immediately stopped and data taking is continued, otherwise the event is fully read out. In the latter case the total dead time is 1.5 ms. The event is directed to L4 (L3 is not yet operating), consisting of a parallel processor farm examining the full event record. If it can verify the L1 and L2 keep signals, L4 stores the data on tape. The event is fully reconstructed offline by L5.

Luminosity Measurement

The luminosity \mathcal{L} is the ratio of the event rate dN/dt and the cross section σ :

$$\frac{dN_i}{dt} = \mathcal{L} \sigma_i, \quad (3.3)$$

it is independent of the process i . Integrated over the time t , this relation reads

$$N_i = L \sigma_i, \quad (3.4)$$

in which L is the integrated luminosity.

To measure a cross section, the number of events N_i fulfilling certain conditions ('cuts') is determined. It is divided by L , which is obtained from the luminosity system (Fig. 3.5), which measures the rate of Bethe Heitler interactions $ep \rightarrow ep\gamma$ (Bremsstrahlung)

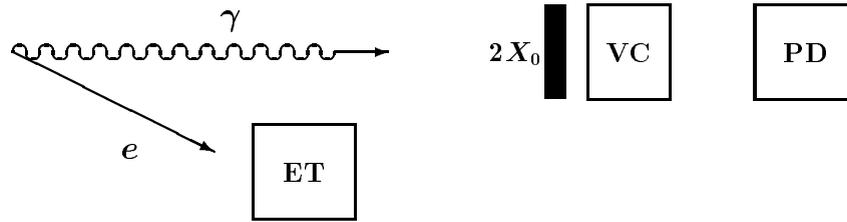


Fig. 3.5. *Bethe Heitler Bremsstrahlung process as seen by the H1 luminosity system. The electron and photon are detected in the small angle electron detector ET and the photon detector PD, respectively. The PD is shielded from synchrotron radiation by a lead filter of two radiation lengths and a water Čerenkov counter.*

for which the cross section is calculable from QED with high precision. Because \mathcal{L} depends on the beam conditions (Eq. (3.1)), the luminosity must be measured in parallel with the data taking.

Analysis

In this chapter all the necessary steps to get from the data recorded by H1 to the aspired cross sections are described. The event selection procedure is elucidated in Sec. 4.1. The kinematic range in which the cross section is measured is defined in Sec. 4.2. The correction of the data for detector effects is discussed in Sec. 4.3 and the corrected data are compared to MC predictions. The final cross section results will be presented in the next chapter.

4.1 Event Selection

In 1996 about 23 million events were recorded by the H1 experiment. This section describes the selection cuts that are imposed to obtain the events used in the present analysis.

First, an inclusive photoproduction sample is selected by requiring a photoproduction subtrigger. Background events, like beam-gas interactions or bremsstrahlung processes, are reduced by specific cuts. The obtained sample is subjected to a jet algorithm, which selects events with at least two jets with $E_T > 4$ GeV. From the photoproduction jet sample, diffractive events are selected by requiring the absence of activity in the forward region.

4.1.1 Run Selection

For the analysis only events are considered which were recorded with the following detector system operational: luminosity system, liquid argon calorimeter (LAr), central jet chambers (CJC) 1 and 2, forward muon detector, backward calorimeter (SPACAL), proton remnant tagger (PRT) and time of flight system (ToF). The number of events remaining after this requirement corresponds to an integrated luminosity of 7.54 pb^{-1} .

4.1.2 Photoproduction Subtrigger S83

The L1 subtrigger S83 selects photoproduction events efficiently and reduces background events to a tolerable level. The trigger requires deposited energy in the low angle electron detector and tracks in the central jet chambers. S83 triggers at a rate of about 25 Hz.

Only events are kept which have the trigger signal S83 set. Listed below are the most important elements of S83 and their requirements. The elements are linked via logical ANDs, i.e., all conditions must be full-filled in order to trigger S83.

- **eTAG:**
more than 4 GeV of deposited energy in ET33,
- **DCRPh_Tc:**
at least 3 track candidates in the central jet chamber,
- **zVtx_sig:**
a significant peak in the z vertex histogram,
- **CIP_Backward:**
signals in more than three sectors of the backward quarter of the central inner proportional chamber. This element is a veto against background due to proton interactions upstream ($z < 0$) with gas or material.

S83 can be triggered by Bethe-Heitler bremsstrahlung processes. To remove these events, the energy deposited in the photon detector is required to be less than 2 GeV. The z coordinate of the reconstructed event vertex is demanded to lie within 35 cm around the origin $z = 0$, to remove background from beam gas interactions. Standard algorithms are used to eliminate background due to coherent noise in the calorimeter, halo events, and cosmic muon events.

4.1.3 Jets

From the photoproduction sample obtained by the cuts mentioned in the previous section, events with two or more jets are selected. The jet algorithm CDFCONE [Hut90] is used.

4.1.3.1 CDFCONE Jet Algorithm

This section describes the CDFCONE jet algorithm as explained in detail in [Sey94].

1. Consider every input object (cf. 4.1.3.2) as a ‘seed’ $s = (\eta_s, \Phi_s)$. Consider the set X of objects within a cone of radius R around the seed:

$$X = \left\{ (\eta, \Phi) \mid \sqrt{(\eta_s - \eta)^2 + (\Phi_s - \Phi)^2} < R \right\}$$

2. Calculate from each seed the following jet parameters

$$E_T = \sum_X E_T, \quad (4.1)$$

$$\eta = \frac{1}{E_{T,X}} \sum_X E_T \eta, \quad (4.2)$$

$$\Phi = \frac{1}{E_{T,X}} \sum_X E_T \Phi, \quad (4.3)$$

in which the sum extends over all objects in the set X . The jet axis is then given by (η, Φ) .

3. If $\eta \neq \eta_s$ or $\Phi \neq \Phi_s$ then define a new seed by the jet axis (η, Φ) and go to step 2.
4. If $E_T > E_T^{\text{cut}}$ then add the jet candidate to a list of ‘protojets,’ if no other jet already exists with the same axis.
5. Consider the centre of every pair of protojets as a seed and repeat steps 2 to 4.
6. Delete protojets that share more than 75 % of their transverse energy with protojets of larger transverse energy.
7. Assign objects in more than one protojet to the one nearest in (η, Φ) . Recalculate the jet parameters. All remaining protojets are the final jets.

The transverse energy is used because it is invariant under Lorentz boosts along z . For this analysis, the transverse energy cut is $E_T^{\text{cut}} = 4$ GeV and the cone size is 1.

As input objects to CDFCONE, a combination of tracks and clusters is used. They are explained in the next section.

4.1.3.2 Combined Objects

Particles with low energy (≤ 1 GeV) are not detected efficiently within the LAr calorimeter, because they are absorbed in the dead material in front of the detector or produce signals below the electronic noise level. For instance, a pion with a momentum of 500 MeV is only detected with a probability of ≈ 10 %. [Mar00]. To improve the measurement of low energetic particles, track information is incorporated. The present analysis uses the software package HFS [Mar], which combines cluster and track information in the following way.

The tracks are extrapolated to the calorimeter front and all calorimeter clusters within a cylinder of a certain radius around the extrapolated tracks are sorted according to their distance from the cylinder axis. Starting at small distances, the cluster energies are added up until the sum equals the track energy. The clusters in the sum are removed from the calorimeter information. The tracks and the remaining clusters form the ‘combined objects.’

The momentum measurement is superior to the calorimeter measurement only at low p_T , since the relative momentum resolution is proportional to the momentum itself: $\sigma_p/p \propto p$. Tracks are therefore only considered, if their transverse momentum is less than 2 GeV.

4.1.4 Detector Acceptance Cuts

The photoproduction dijet sample has to be restricted to a kinematic range in which the detector performs efficiently.

For a precise jet measurement, the jets are required to lie within the central acceptance region of the LAr calorimeter: $-1 < \eta_{\text{jet}} < 2$. The upper limit follows from the jet cone size and from the cut in η_{max} (see below).

The small angle electron detector is efficient in the range $0.3 < y < 0.7$. When the electron is detected near the edge of the electron tagger, the electron shower will not be fully detected. A cut on the centre of the shower is therefore applied, which requires the shower to be fully contained in the detector: $X_{\text{el}} < 6.5$ cm.

4.1.5 Diffractive Cuts

Diffractive events with a rapidity gap are selected by demanding the absence of detector signals above noise levels in the forward region.

No activity in the seven scintillator layers of the Proton Remnant Tagger scintillator is permitted. This cut provides an upper limit of 1.6 GeV on the invariant mass of the Y system.

Due to collimator scattering, the forward muon detector can be used to veto activity in the forward range. However, because the noise is at a high level in the FMD, demanding the absence of activity would dramatically reduce the efficiency to detect a diffractive event. From studies of the detector noise it was concluded that a maximum of one hit pair in the three pre-toroid chambers gives a tolerable rejection of non-diffractive background.

$x_{\mathbb{P}}$ is demanded to be less than 0.05 to remove reggeon exchange contributions.

The most forward LAr calorimeter cluster with an energy larger than 400 MeV defines η_{max} . From a study of non-diffractive contributions (Sec. 4.3.4) the limit on η_{max} is chosen to be 2.8.

4.1.6 Preselection

The H1 data is stored on tape at DESY. All data processing for this analysis was done on the LINUX cluster at the Physical Institute in Heidelberg. This meant transferring the data in form of DST files¹ via the Internet. Because of the huge amount of data, the files were processed in a preselection step prior to the actual analysis selection. Only events that passed the preselection were written to disk and used in the subsequent analysis.

1. Data Summary Tape, a file format used within the H1 collaboration.

The preselection kept events with the subtrigger S83 signal and at least one jet with $E_T^{\text{jet}} > 3$ GeV. The jet algorithm used was CDFCONE with a cone size of 1. In contrast to the main analysis, it did not use combined objects but only calorimeter cluster information. Although a lower E_T^{jet} cut was used, events were lost during the preselection step, that would have passed the actual analysis cuts. To take this effect into account, the simulated MCs are processed by the same preselection program. The efficiency of the preselection is $\approx 84\%$ (cf. Tab. 4.3).

4.1.7 Summary and Event Display

The selection cuts are summarized in Tab. 4.1. 1310 diffractive dijet events remain after these cuts. The data used in the cross section measurement corresponds to an integrated luminosity of 7.54 pb^{-1} .

A typical diffractive dijet event is shown in Fig. 4.1. On the left, the main detector is depicted in the (z, R) plane. The two jets can clearly be identified. In the forward region there is no activity. The bottom right zone shows the same event in an (R, Φ) view; the back-to-back structure of the jets reflects the balancing of transverse momenta. The etagger is displayed in the rightmost zone at the top. The two remaining zones exhibit the absence of activity in the forward muon detector (left) and in the proton remnant tagger (right).

4.2 Definition of the Cross Sections

The detector cuts described in the previous section limit the accessible kinematic range in which the cross section can be measured. The definition of the cross sections, as they are measured in this analysis, is given in Tab. 4.2. No η_{max} or similar cut is imposed; instead, the ‘Eilat definition’ [Eil96] of a diffractive process is adopted.

Eilat Definition

On hadron level, the systems X and Y are separated by the largest rapidity gap in the event. An event is then diffractive, if

$$x_{\mathbb{P}}^{\text{had}} < 0.05 \quad \wedge \quad M_Y^{\text{had}} < 1.6 \text{ GeV} \quad \wedge \quad -t^{\text{had}} < 1 \text{ GeV}^2. \quad (4.4)$$

The advantage over a definition which demands an η_{max} cut on hadron level, is the independence of fragmentation processes.

4.3 Correction of Detector Effects

The final cross sections are given on hadron level, therefore the data need to be corrected for detector effects. These can be studied by passing generated events through a detailed simulation of the H1 detector and comparing the result to the known input. The efficiency

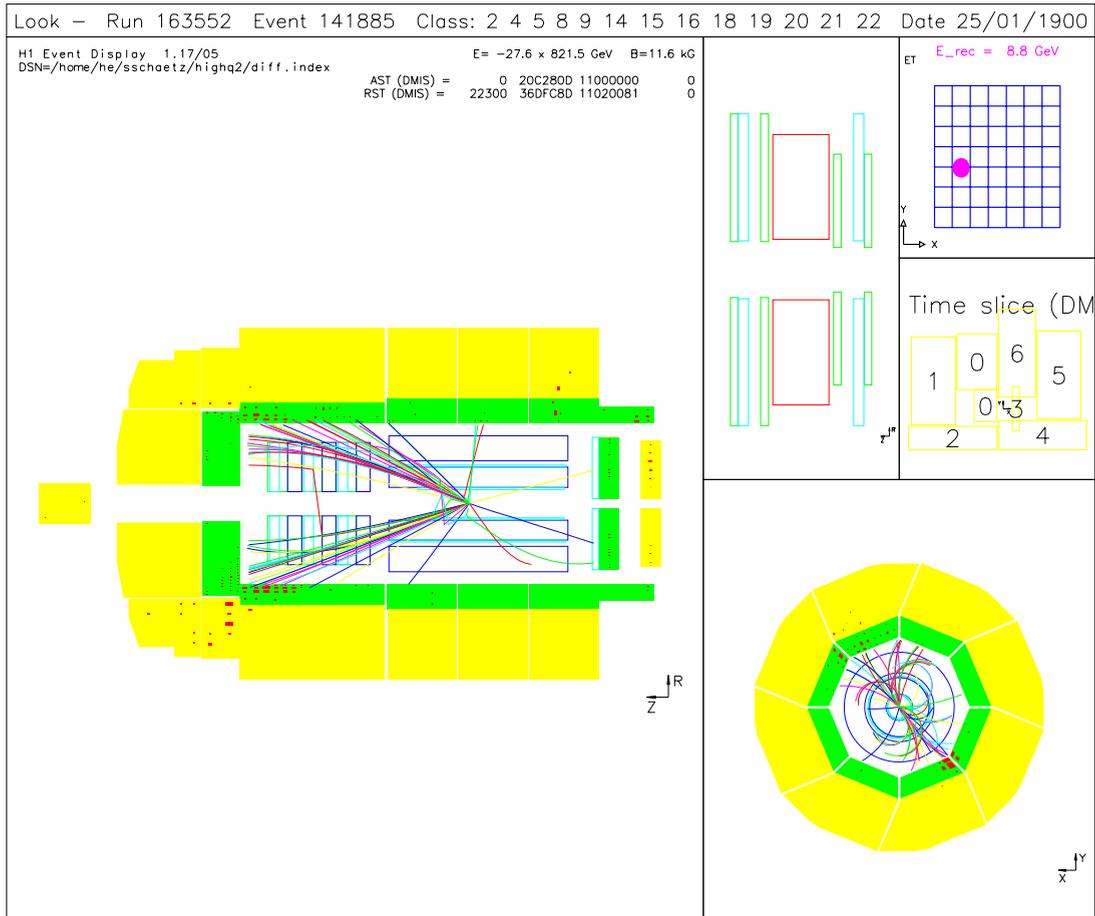


Fig. 4.1. Event display of a diffractive dijet event. The H1 main detector is shown on the left and in the lower right zone. The etagger is shown in the upper right corner. Below the etagger, the proton remnant tagger scintillator layers are depicted. In the middle, the forward muon detector is diagrammed.

Selection Cuts on Detector Level

Name	Description	Reason
run selection	HV and read-out	availability of detector systems
trigger selection	S83	tagged electron and tracks
background rejection	$ z_{\text{Vertex}} < 35 \text{ cm}$ $E_{\text{PD}} < 2 \text{ GeV}$ cosmics veto coherent noise veto	beam/gas, beam/pipe processes Bethe-Heitler processes
photoproduction cuts	$Q^2 < 0.01 \text{ GeV}^2$ $0.3 < y < 0.7$ $ X_{\text{el}} < 6.5 \text{ cm}$	acceptance ET33
jet selection	CDFCONE, R=1 combined objects # jets ≥ 2 $E_T^{\text{jet}} > 4 \text{ GeV}$ $-1 < \eta_{\text{jet}} < 2$	low p_T particles correlations jets/partons acceptance LAr
diffractive cuts	$x_{\mathbb{P}} < 0.05$ $\sum_{1:7} \text{PRT} = 0$ $\sum_{1:3} \text{FMD} \leq 1$ $\eta_{\text{max}} < 2.8$	\mathbb{P} dominated regime $\left\{ \begin{array}{l} M_Y < 1.6 \text{ GeV}, \\ -t < 1 \text{ GeV}^2, \\ \text{rapidity gap} \end{array} \right.$

Tab. 4.1. Selection cuts imposed on the total 1996 H1 data sample to obtain the events used in the cross section measurement. After the run selection the amount of data corresponds to an integrated luminosity of 7.5 pb^{-1} . After all cuts, 1310 events remain.

Cross Section Definition

$0.3 < y < 0.7$
$Q^2 < 0.01 \text{ GeV}^2$
$x_{IP} < 0.05$
$M_Y < 1.6 \text{ GeV}$
$-t < 1 \text{ GeV}^2$
CDFCONE, R=1
$p_T^{\text{jet}} > 4 \text{ GeV}$
$\# \text{ jets} \geq 2$
$-1 < \eta_{\text{jet}} < 2$

Tab. 4.2. Definition of cross sections on hadron level.

to detect diffractive events with the detector can then be calculated and taken into account as a correction factor.

4.3.1 Detector Simulation

A Monte Carlo generator event consists of a list of partons, their four-vectors and charges. Stable hadrons are obtained by applying a fragmentation model. To obtain the detector response to the event, the interactions of the particles with the detector material must be evaluated. For the H1 detector, the program **H1SIM** [Mey91] based on the **GEANT** package [Bru94] performs these calculations.

Each particle is treated individually in its passage through the detector. Tabulated cross sections are evaluated using random numbers, giving the probability for an interaction to take place. These interactions may result in secondary particles, which themselves must be traced. In the end, the subdetector response is obtained in form of simulated electronic signals, from which also the trigger decision can be derived. The MC events are then reconstructed with the same program that is used for data events.

Electron Tagger Treatment

The electron tagger (etagger) must be treated in a special manner, because the simulation does not give an adequate description. This stems from the following reasons [Lev]. Because of its large displacement from the interaction point, the etagger acceptance is largely influenced by electron-beam tilts. A shift of $\approx 1 \text{ mm}$ in the horizontal plane can change the acceptance by 20 %. The beam parameters vary significantly from one fill to another. Furthermore, even in the same luminosity run, variations are observed due to changes in the magnet currents in the vicinity of the interaction point. At present, these changes are not considered in **H1SIM**, so the simulated response from the electron tagger is not correct and cannot be used. Instead the acceptance is parameterized as a function

of the inelasticity y . Then, for a generated event, the acceptance and efficiency is taken into account by a weight depending on the true y , which is applied to the event.

4.3.2 Monte Carlos used for Correction

In correcting the data for detector effects, care must be taken to consider all possible sources of migrations into the detector level diffractive sample. Three different MCs are involved in the data correction. Their domains in the $(x_{\mathbb{P}}^{\text{had}}, M_Y^{\text{had}})$ plane are illustrated in Fig. 4.2.

- **POMPYT**

This resolved pomeron model implementation is used for the pomeron dominated regime $x_{\mathbb{P}}^{\text{had}} < 0.05$. The present version of POMPYT can generate only elastically scattered protons, no proton dissociation is taken into account. In Fig. 4.2, its kinematic range is represented by the line at $M_Y = m_p = 0.94$ GeV. In principle, the pomeron and the reggeon exchange should be covered by the MC, but for technical reasons only the pomeron exchange is available as a simulated MC.

- **PYTHIA**

The inclusive Monte Carlo generator PYTHIA is used to correct migrations from large masses $M_Y > 5$ GeV and $x_{\mathbb{P}}^{\text{had}} > 0.05$. PYTHIA contains proton dissociation, but the description of the low M_Y regime is not good.

- **DIFFVM**

The effect of migrations across the $M_Y = 1.6$ GeV boundary is corrected under the assumption that the proton vertex factorizes from the rest of the interaction. Then a correction factor can be derived from DIFFVM (cf. 4.3.7). This factor is applied to the final cross section.

A combination of POMPYT and PYTHIA events is used to correct the data to stable hadron level. Because the PYTHIA generator is not tuned to data in the vicinity of diffraction, for which it is used in this analysis, the absolute normalization of the number of PYTHIA events is not taken from the generated luminosity. Instead, the shapes of the PYTHIA and POMPYT event distributions in $x_{\mathbb{P}}^{\text{det}}$ are fitted to the data distribution of $x_{\mathbb{P}}^{\text{det}}$. The obtained normalization factors b and c to the MCs define the MC Set used for the correction of the data:

$$\text{MC Set} \equiv b \text{ PYTHIA} + c \text{ POMPYT}.$$

For the fit, the PYTHIA MC is used also in the DIFFVM regime $m_p < M_Y^{\text{had}} < 5$ GeV. The fit procedure is described in detail in Appendix A. Here, only the results are discussed. Fig. 4.3 shows the $x_{\mathbb{P}}^{\text{det}}$ distributions of the data and the MC Set. The obtained χ^2 per degree of freedom is 1.87. The description of the data will most probably improve if the missing reggeon exchange MC is included in the fit. It will give additional

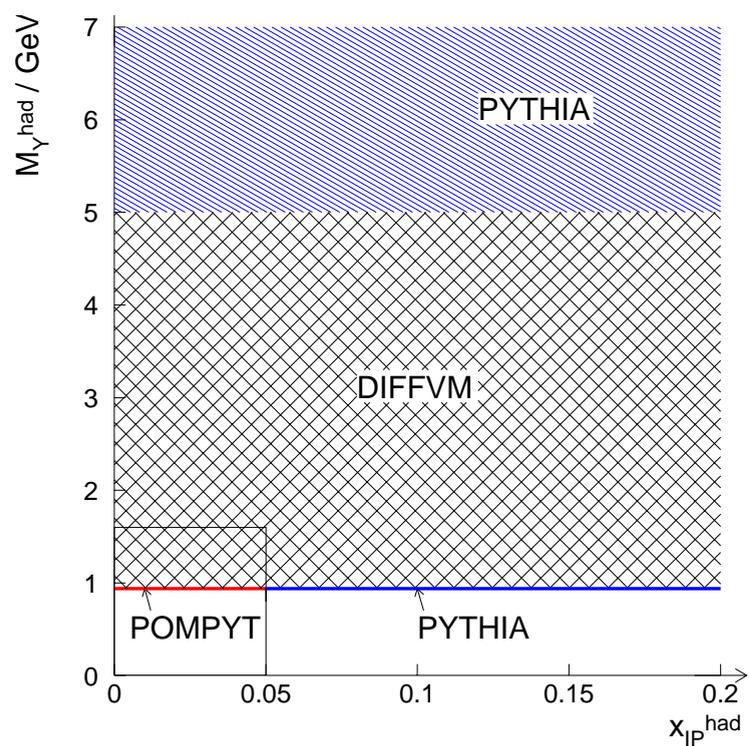


Fig. 4.2. $(x_{IP}^{\text{had}}, M_Y^{\text{had}})$ plane of used Monte Carlos. The kinematic range in which the cross section is measured is indicated by the rectangle ($0 < x_{IP}^{\text{had}} < 0.05$, $0 < M_Y^{\text{had}} < 1.6$ GeV).

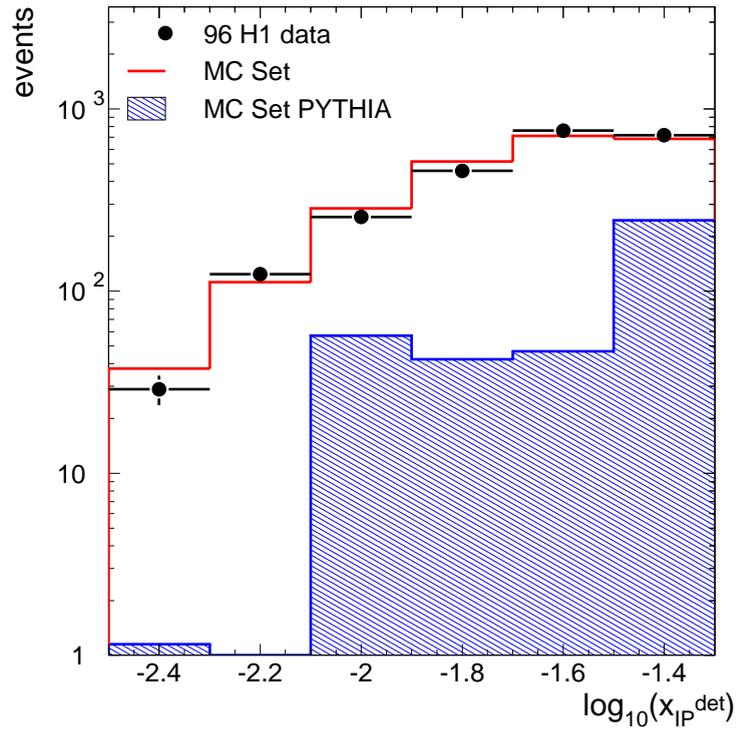


Fig. 4.3. x_P^{det} distributions for the data and the MC Set composed of POMPYT and PYTHIA events. The MC Set is normalized to the data events. The contribution of PYTHIA events to the MC Set is shown as the hatched histogram. The DIFFVM regime $m_p < M_Y^{\text{had}} < 5$ GeV is not covered by the MC Set.

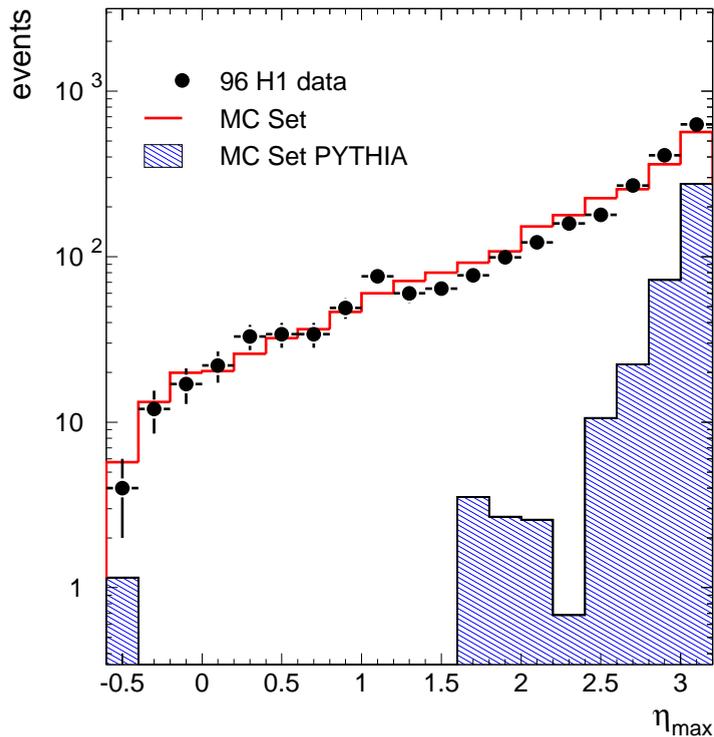


Fig. 4.4. η_{\max} distributions of the data and the MC Set composed of POMPYT and PYTHIA events. The contribution from PYTHIA is shown as the hatched histogram. The MC Set is normalized to the number of data events.

contributions at large x_P^{det} , where now the PYTHIA MC is dominant. This also implies that the number of migration events from PYTHIA is overestimated at present. Because of the large uncertainty related to the background estimation, harsh cuts are applied which limit the background contribution to a low level of a few percent (see below).

A directly measurable quantity related to x_P^{det} is η_{\max} , both are sensitive to energy deposited in the forward region (cf. Eq. (2.17)). η_{\max} directly measures the gap width in the LAr calorimeter.

The η_{\max} distributions of the data and the MC Set are shown in Fig. 4.4. The MC Set is normalized to the number of data events. The PYTHIA η_{\max} distribution exhibits a steep fall-off as the gap size increases. This is what is expected for non-diffractive processes: the probability for a gap is exponentially suppressed as a function of the gap width. Gaps can only be produced by multiplicity fluctuations in the final state particle distribution. The PYTHIA event at $\eta_{\max} = -0.5$ may be the result of such a process. The diffractive POMPYT MC, in contrast, decreases softly as a function of the gap width and can describe the data alone in the region $\eta_{\max} < 2.5$. A clear signal for diffraction is therefore observed in the data.

The η_{\max} cut is particularly suited to suppress non-diffractive background. The integrated fraction of PYTHIA events in the MC Set as a function of the upper limit η'_{\max}

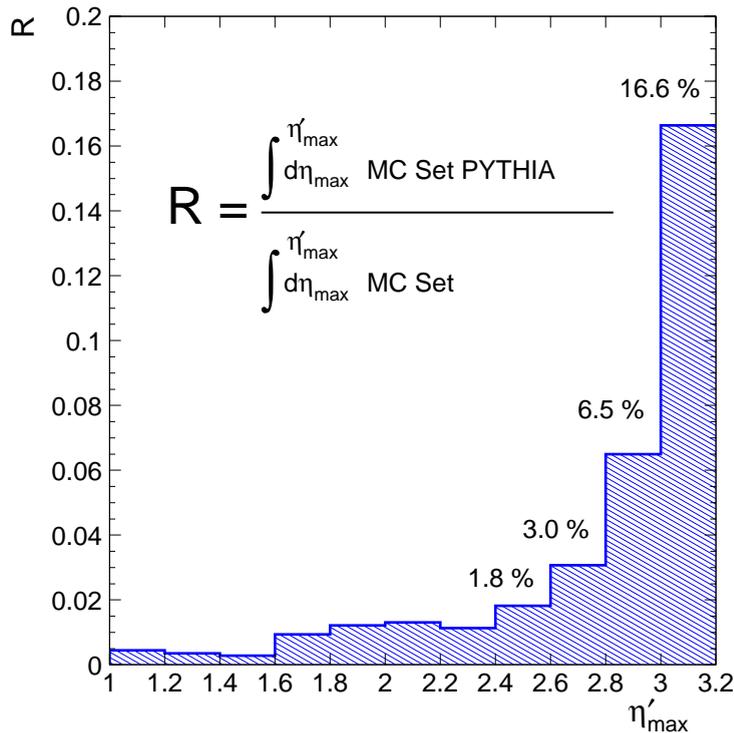


Fig. 4.5. Fraction of PYTHIA events in the MC Set used for the correction of the data as a function of an upper limit on η_{\max} . For $\eta_{\max} < 2.8$ this fraction is 3.0 %.

on η_{\max} is shown in Fig. 4.5. In the diffractive regime, the PYTHIA contribution is negligible, but it rises strongly for $\eta'_{\max} > 2.8$. Although the contributions are below 7 % for $\eta_{\max} < 3.0$, because of the low statistics of the PYTHIA MC, the η'_{\max} is chosen to be 2.8, in order to not have the errors on the cross sections dominated by statistical errors of the background MC.

4.3.3 Description of Uncorrected Data

A reliable correction of detector effects can only be achieved, if the MC can describe the detector level event distributions of the data. In Figs. 4.6 and 4.7 comparisons are given between data and MC on detector level. The MC Set is normalized to the number of data events. Discrepancies are seen at large x_{γ} and large z_{IP} . In M_X , the MC is different in shape for $15 \text{ GeV} \leq M_X \leq 30 \text{ GeV}$. The description is good in all other variables.

Fig. 4.8 shows the mean transverse energy flow per event in the vicinity of the jet with largest transverse momentum. The jet profiles are given in η and Φ relative to the jet axis. In Fig. 4.8a only the Φ hemisphere of this jet is considered to eliminate energy contributions from the second jet. For Fig. 4.8b the range is limited to two η units around the jet axis. Because in Fig. 4.8b the absolute value of $\Delta\Phi$ is shown, the energy is roughly two times higher than in Fig. 4.8a. Only the POMPYT MC is used for this comparison.

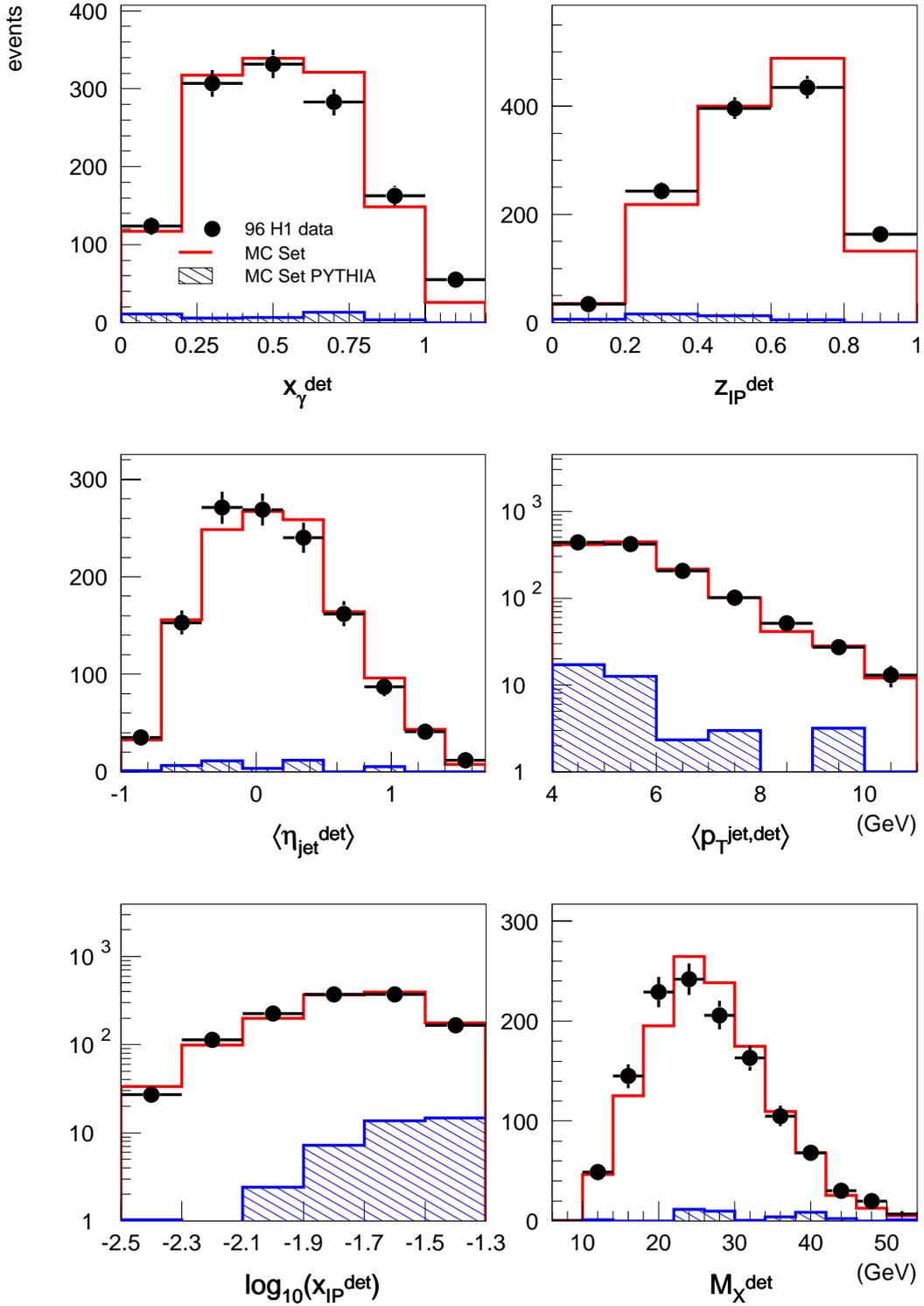


Fig. 4.6. Uncorrected detector level event distributions of the data and the MC Set. The PYTHIA contribution to the MC Set is shown as the hatched histogram. The MC Set is normalized to the number of data events.

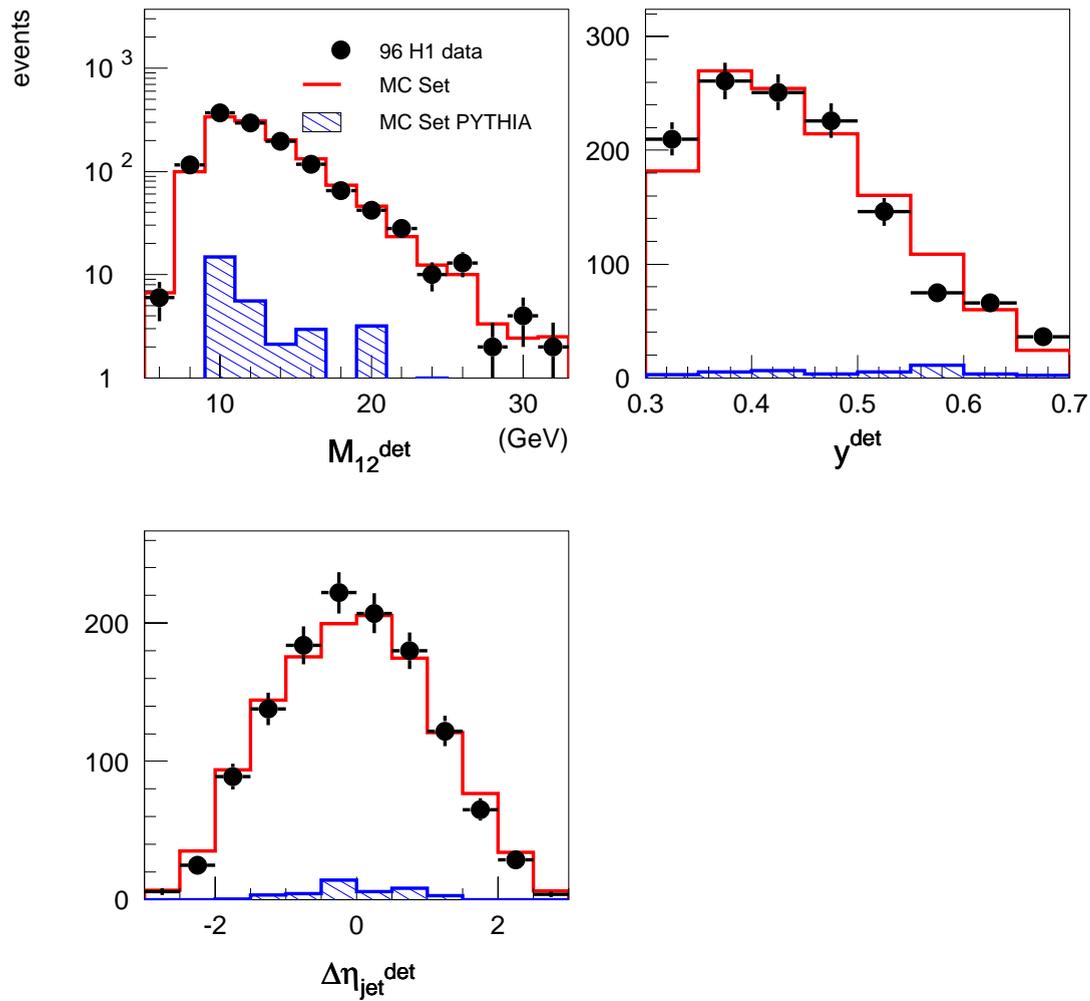


Fig. 4.7. Uncorrected detector level event distributions of the data and the MC Set (cont'd). The PYTHIA contribution to the MC Set is shown as the hatched histogram. The MC Set is normalized to the number of data events.

The description is good in both η and Φ .

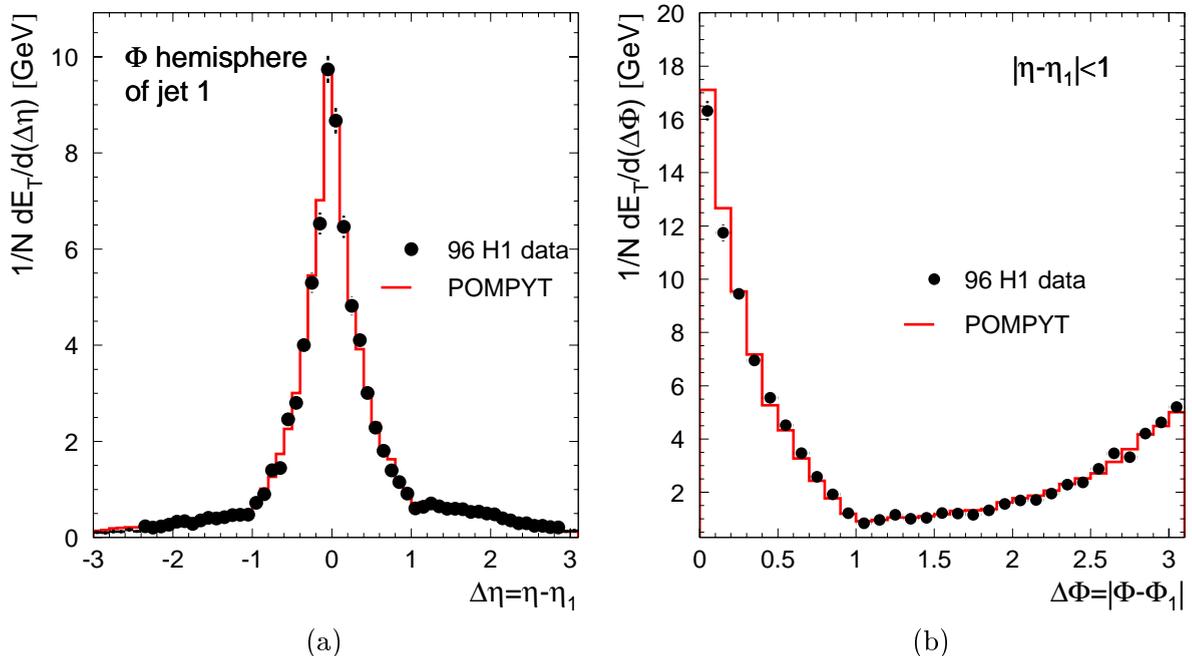


Fig. 4.8. Jet profiles of the jet with largest transverse momentum in (a) $\Delta\eta$ and (b) $\Delta\Phi$. Shown is the mean transverse energy flow per event relative to the jet axis. In (a), only the Φ hemisphere of the jet is considered. In (b), the η region is limited to two units around the jet axis.

Fig. 4.9 shows the energy flow on detector level. $\eta_{\text{jet}} < 1$ is demanded for both jets, to avoid jet activity in the forward region. The energy flow in the forward region is underestimated by the MC by 1 GeV per η unit. In the backward part ($\eta < -1.5$) agreement between data and MC can be established by recalibrating the SPACAL and the BBE (last wheel of the LAr calorimeter) by factors 1.6 and 1.15, respectively. However, the calibration is left to neutral current DIS events. The description of the energy flow is acceptable.

The MC Set can be used for the correction of the data because it describes the data event distributions and the energy flow in and outside the jets.

4.3.4 Correction of the Data

The hadron level cross section differential in the variable x in bin i is given by

$$\frac{d\sigma^i}{dx} = \frac{N_{\text{had}}^i}{L \Delta x}, \quad (4.5)$$

where N_{had}^i is the number of events, selected on hadron level according to the cross section definition in Tab. 4.2. L is the integrated luminosity of the total event sample, from which the events were selected, and Δx is the bin width. The cross section on hadron level for

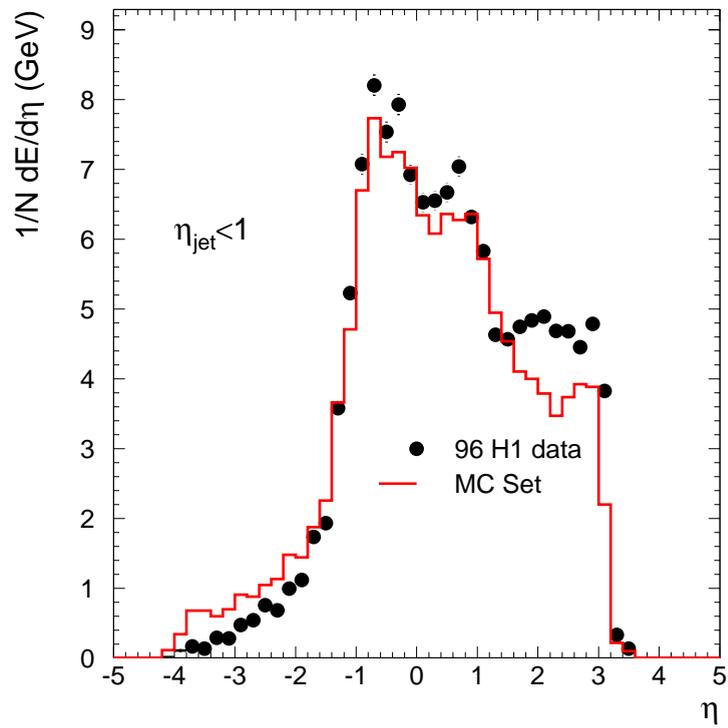


Fig. 4.9. Energy flow on detector level. $\eta_{\text{jet}} < 1$ is demanded to avoid jet energy in the forward region.

the MC is calculated according to Eq. (4.5). For the data, N_{had}^i is not known, only the number N^i of events on detector level is available. Using a correction MC, N^i can be related to N_{had}^i .

For this analysis a bin-to-bin correction method was adopted, i.e., each bin of the cross section is individually corrected. The number N^i of events selected on detector level by the cuts given in Tab. 4.1 is related to N_i^{had} by

$$N_{\text{had}}^i = \frac{N_{\text{data}}^i - N_{\text{non-diffr.}}^i}{C_{\varepsilon}^i} C_{\text{FMD}} C_{\text{diss}},$$

with the quantities defined as follows. $N_{\text{non-diffr.}}^i$ is the number of non-diffractive (background) events in bin i on detector level. $N_{\text{non-diffr.}}^i$ is given by the number of PYTHIA events in the MC Set:

$$N_{\text{non-diffr.}}^i = b \text{PYTHIA}^{\text{det}}(i),$$

it is subtracted from the number of data events. The obtained number of background corrected data events is then corrected for efficiency and migration effects by applying the correction factors C_{ε}^i , C_{FMD} and C_{diss} .

The efficiency to detect a diffractive event is limited because of the limited geometrical detector acceptance, noise in the detector systems, and because of the pure statistical nature of interactions in general. Due to the limited detector resolution, migration effects occur, which means that an event can be reconstructed in a detector level bin that differs from the one in which it was on hadron level. There are also events that are only part of either the hadron sample or the diffractive sample, but not of both.²

C_{ε}^i is given by the ratio of the number of POMPYPY events in the detector sample to the number of POMPYPY events in the hadron sample:

$$C_{\varepsilon}^i = \frac{\text{POMPYPY}^{\text{det}}(i)}{\text{POMPYPY}^{\text{had}}(i)}.$$

C_{ε}^i can be decomposed as follows:

$$C_{\varepsilon}^i = \varepsilon_{\text{trig}}^i \varepsilon_{\text{etagger}}^i \left(\varepsilon_{\text{rec}}^i + \text{mig} \right), \quad (4.6)$$

with

$$\begin{aligned} \varepsilon_{\text{trig}}^i &= \frac{\text{POMPYPY}^{\text{det}}(i)}{\text{POMPYPY}^{\text{det}} \setminus \{\text{trigger}\}(i)} && \text{trigger efficiency,} \\ \varepsilon_{\text{etagger}}^i &= \frac{\text{POMPYPY}^{\text{det}} \setminus \{\text{trigger}\}(i)}{\text{POMPYPY}^{\text{det}} \setminus \{\text{trigger}, \text{etagger}\}(i)} && \text{etagger efficiency,} \\ \varepsilon_{\text{rec}}^i &= \frac{\text{POMPYPY}^{\text{det}} \setminus \{\text{trigger}, \text{etagger}\}(i)}{\text{POMPYPY}^{\text{had}}(i)} && \text{reconstruction efficiency,} \\ \text{mig} &= \frac{\text{POMPYPY}^{\text{det}} \setminus \{\text{trigger}, \text{etagger}\}(i)}{\text{POMPYPY}^{\text{had}}(i)} && \text{migrations into detector sample.} \end{aligned}$$

2. The detector sample is defined by the events that pass the detector level diffractive cuts. In the same way the hadron sample is defined.

in which $\text{POMPYT}_{\text{mig}}^{\text{det}}$ denotes the POMPYT migration events that are present only in the detector sample. The \backslash symbol precedes a list of detector elements that are not required for the corresponding sample.

As studied in a previous analysis [Kau98], the trigger simulation in H1SIM gives an adequate description of the subtrigger S83. Therefore, in the present analysis, the trigger efficiency is calculated as defined above, although it could be derived from the data by using a monitor trigger. The mean trigger efficiency is 81 % averaged over all bins.

As explained in Sec. 4.3.1, the etagger efficiency is given by a factor calculated from the generated y . It is thus different for every event. The mean value of the etagger efficiency is 48 % averaged over all bins.

C_ε^i is shown in Fig. 4.10 for all cross section variables. The mean value is $\approx 27\%$. The fall-off at large values of x_P is due to the η_{max} cut. The shape in y is given by the etagger efficiency.

The efficiency losses and migrations can be studied by applying the cuts in succession. Tab. 4.3 displays the monitoring of all cuts for the MC Set. Starting with the hadron sample (labelled ‘hadron 2jets’), the detector level cuts are gradually imposed. The number of events remaining in the sample is shown in the rightmost column. Events are lost due to the limited detector acceptance and efficiency. The most significant losses are observed in the η_{max} and p_T^{jet} cuts. After all detector cuts have been applied (‘hadron 2jets + all detector cuts’), the cuts on hadron level are gradually removed. Now migration effects from outside the hadron level kinematic range become visible. By far the most dramatic effect is seen in removing the $\langle p_T^{\text{jet, had}} \rangle$ cut. Dividing the event number of the detector sample by the number of events in the hadron sample yields the $\approx 28\%$ efficiency observed in Fig. 4.10.

4.3.5 Resolutions

Figs. 4.11, 4.12 and 4.13 show the resolutions in the cross section variables. The cross section binning was not chosen finer than half the resolution in the corresponding variable. The variables reconstructed on detector level are well correlated to the hadron level quantities. The correlation plots of $\Delta\eta^{\text{jet}}$ exhibit an additional anti-correlation structure which is due to wrong assignments of jets. The jets on hadron level are assigned to the jets on detector level by minimizing the distance in (η, Φ) . Since the scattering angle $\hat{\theta}$ of the subsystem depends on $\Delta\eta^{\text{jet}}$ through symmetric functions, this effect has no consequences. The other jet related quantities are defined as the mean of both jets (partons).

4.3.6 Noise in Forward Detectors

The fraction of diffractive events which are lost due to electronic noise in the forward muon detector can be estimated from randomly triggered events. Because this effect is not dependent on kinematics, the value obtained in an analysis of DIS diffractive jets [Sch00] is used. According to a quoted fraction of $R = 5.5\% \pm 1.4\%$ diffractive events lost

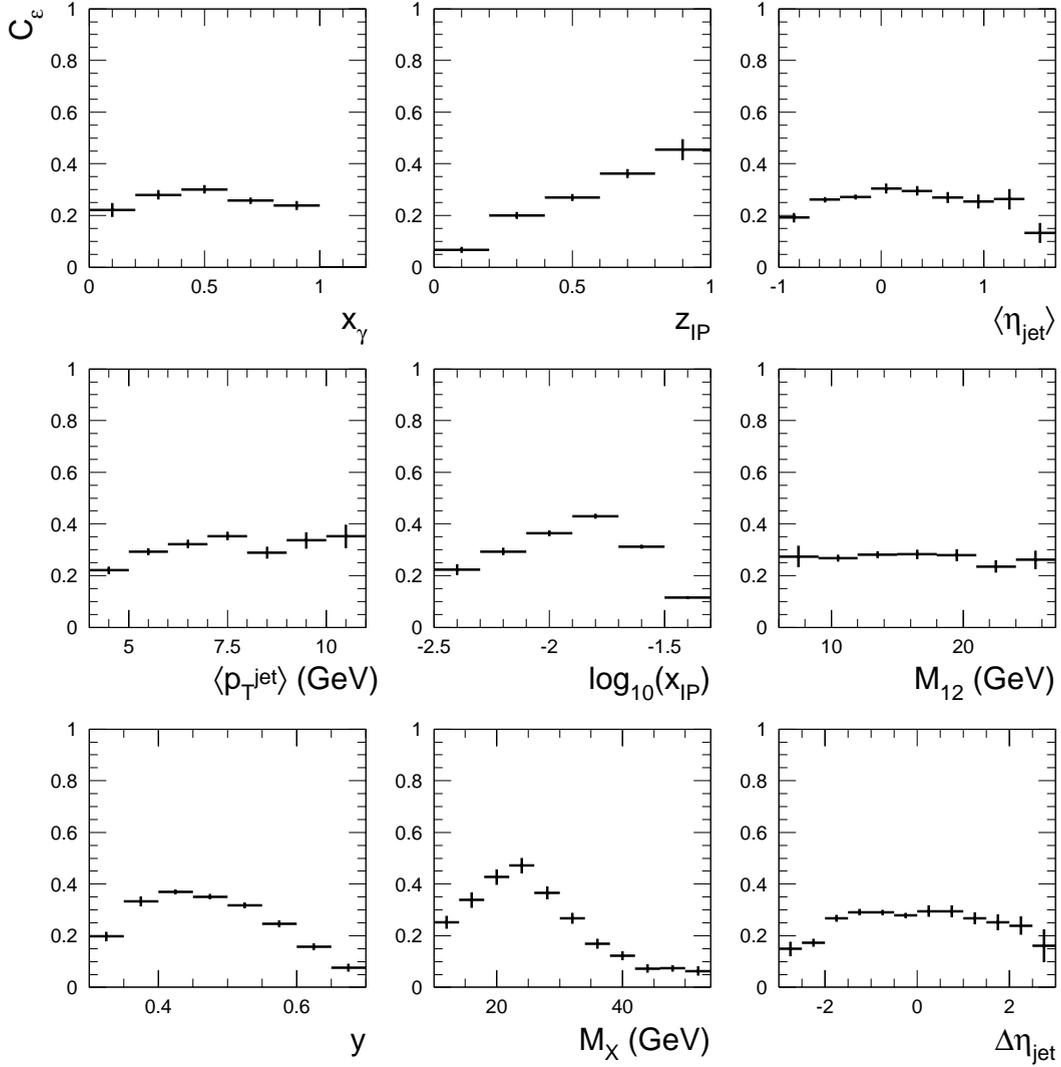


Fig. 4.10. The efficiency correction factor C_ε for all cross section variables. C_ε takes into account the trigger, etagger, and reconstruction efficiencies and migrations into the detector level diffractive sample. The proton dissociation correction and the correction for noise in the forward muon detector are not included.

Cut Monitoring		
	hadron 2jets	4719
	↓	
	$+\varepsilon_{\text{et ag}}$	2252
	↓	
	$+\varepsilon_{\text{trig}}$	1878
	↓	
	+noise patterns	1826
	↓	
	$+y_{\text{et ag}}$	1786
	↓	
efficiency losses and migrations out of detector sample	$+E_{\text{PD}}$	1766
	↓	
	$+x_{\text{IP}}$	1729
	↓	
	$+\eta_{\text{max}}$	1080
	↓	
	+PRT	1059
	↓	
	+FMD	1054
	↓	
	$+p_T^{\text{jet}}$	790
	↓	
	$+\eta_{\text{jet}}$	776
	↓	
	$+\varepsilon_{\text{preselection}}$	634
	detector 2jets + all hadron cuts	
	↓	
	$-\eta_{\text{jet had}}$	676
	↓	
	$-p_T^{\text{jet had}}$	1192
	↓	
migrations into detector sample	$-t_{\text{had}}$	1192
	↓	
	$-M_Y^{\text{had}}$	1192
	↓	
	$-x_{\text{IP}}^{\text{had}}$	1220
	↓	
	$-y^{\text{had}}$	1242
	↓	
	$-Q_{\text{had}}^2$	1310
	detector 2jets	

Tab. 4.3. Monitoring of cut efficiencies. Starting on hadron level the detector cuts are gradually imposed. When all detector cuts are applied, the hadron level cuts are removed. The event numbers are obtained from the MC Set normalized to the number of data events.

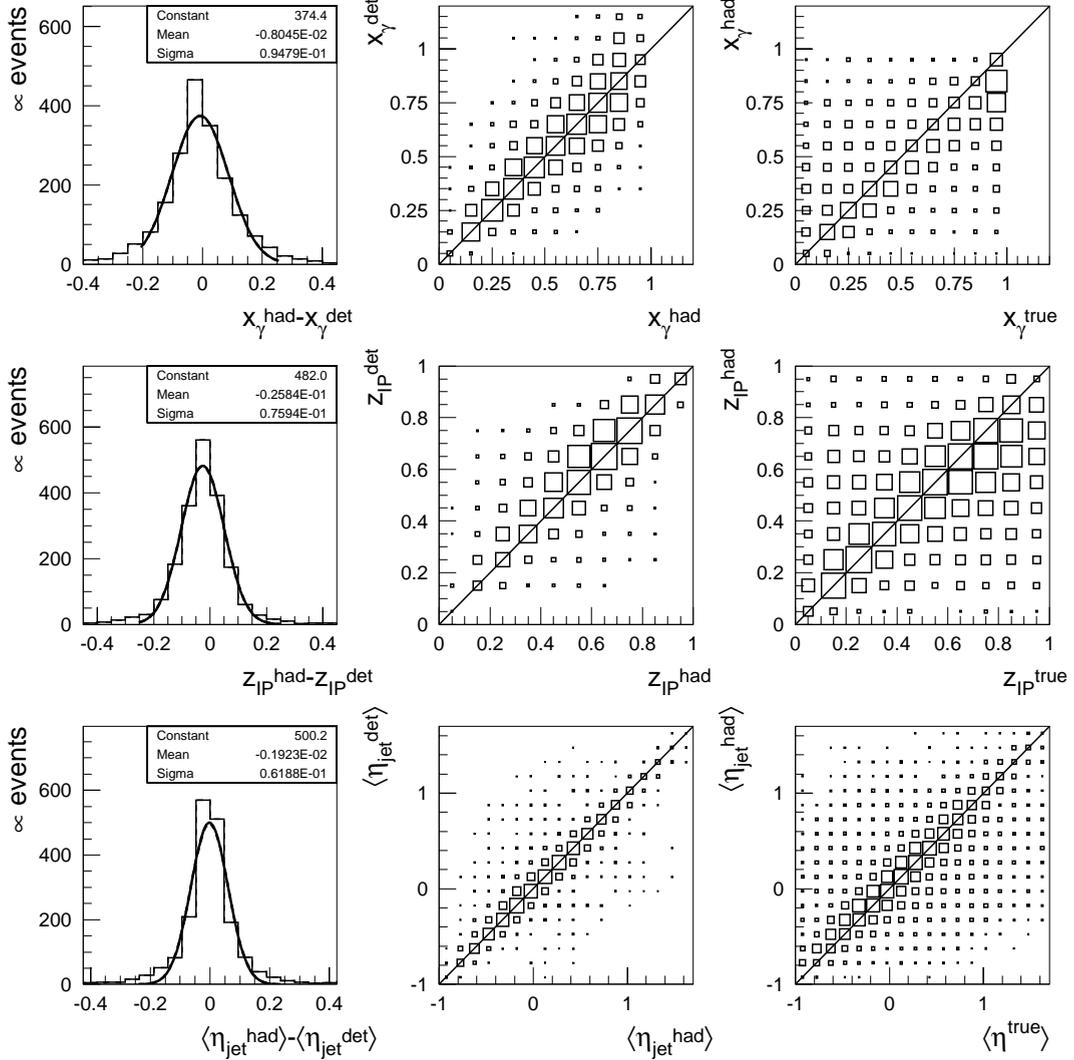


Fig. 4.11. Resolutions and correlations in x_γ (top row), z_{IP} (middle row), and η_{jet} (bottom row). The left column shows the resolution in reconstructing the hadron level quantity on detector level. In the middle, the correlation between the quantity reconstructed on detector level and the quantity on hadron level is shown. The right column shows the correlation between the hadron level quantity and the true value of the quantity as it was generated. In the case of jet quantities, the true value corresponds to the value for the partons.

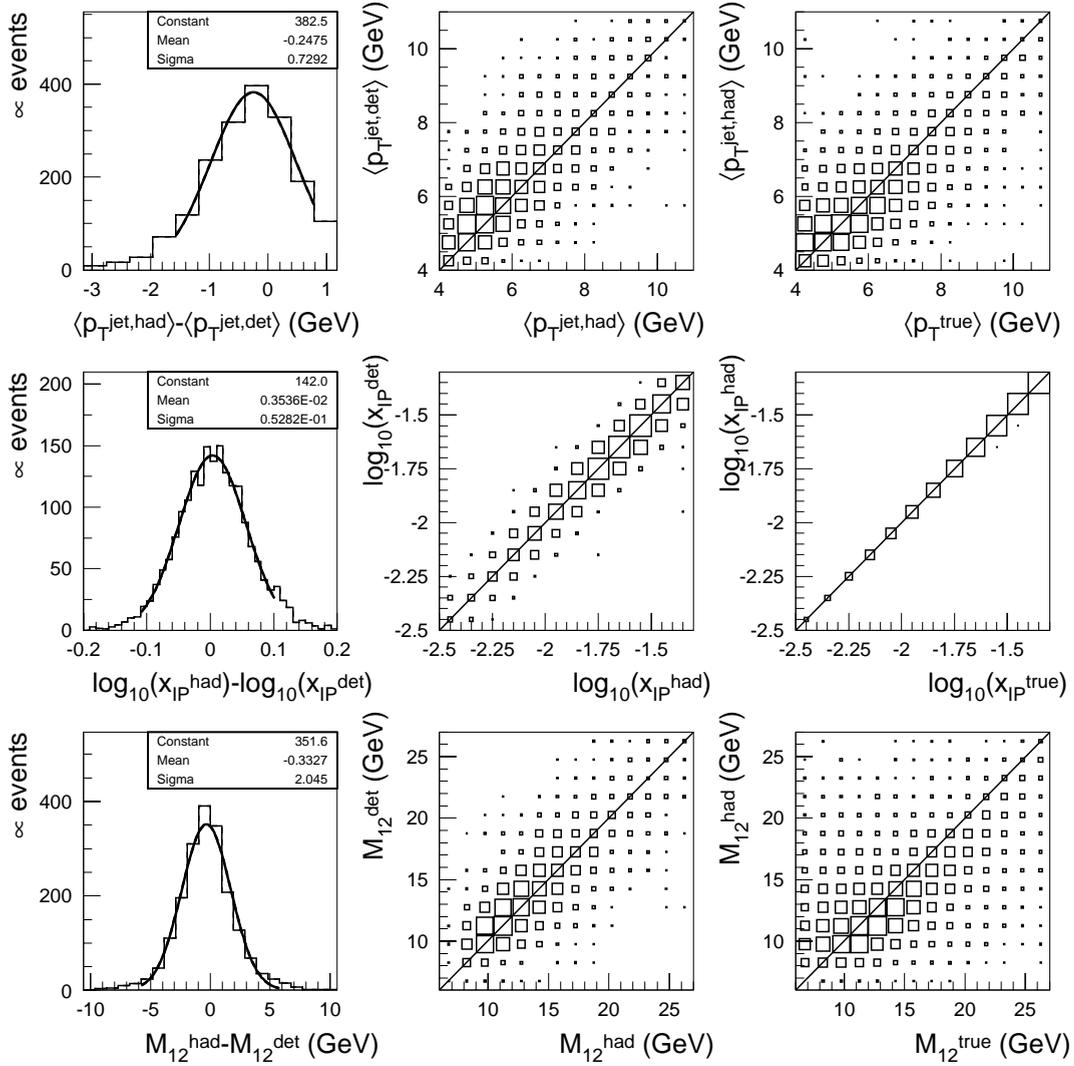


Fig. 4.12. Resolutions and correlations for p_T^{jet} (top row), x_{IP} (middle row), and M_{12} (bottom row). For an explanation see the caption of Fig. 4.11.

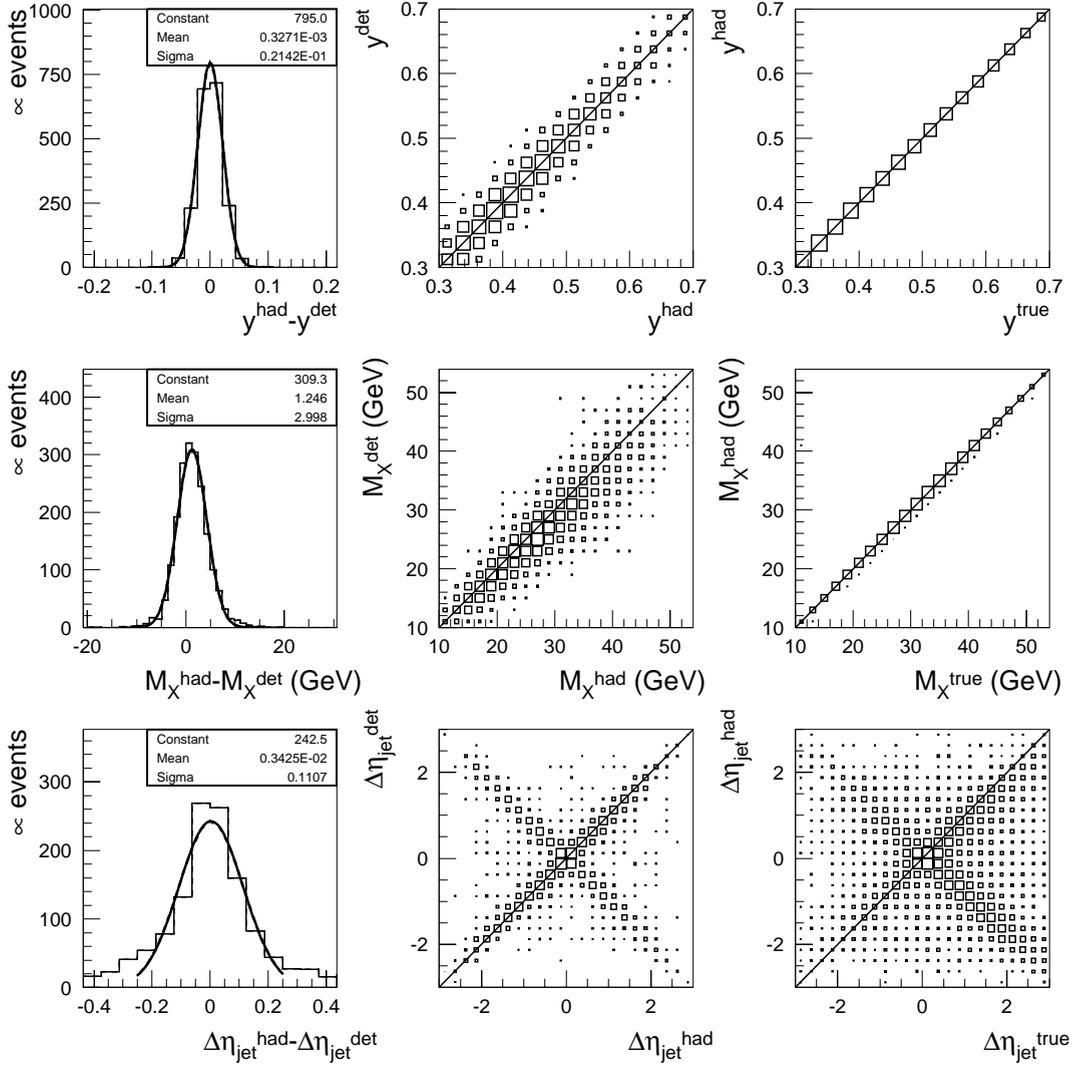


Fig. 4.13. Resolutions and correlations for y (top row), M_X (middle row), and $\Delta\eta_{\text{jet}}$ (bottom row). For an explanation see the caption of Fig. 4.11.

due to noise in the FMD, the overall normalization of the cross sections has to be enlarged by a factor

$$C_{\text{FMD}} = \frac{1}{1 - R} = 1.058 \pm 0.016.$$

The number of events lost due to noise in the proton remnant tagger is quoted to be negligible.

4.3.7 Correction for Proton Dissociation

The cross section is measured for $M_Y^{\text{had}} < 1.6$ GeV. This means, that the proton is allowed to dissociate into a system Y . Proton dissociation in the low M_Y range is not described in the PYTHIA Monte Carlo generator. The process of proton dissociation is assumed to be independent from the rest of the interaction. Then the effect can be studied with the diffractive vector meson generator DIFFVM, which can simulate proton dissociation. A correction factor is derived, which describes the fraction of events which migrate into the detector sample from beyond the $M_Y^{\text{had}} = 1.6$ GeV boundary. The factor is not determined in this analysis, but taken from [Sch00]. A large error of 100 % on the factor accounts for the uncertainties related to the correction procedure. According to a quoted fraction of $R = 6.5\% \pm 6.5\%$ events migrating from larger Y masses into the detector sample, the cross section has to be reduced by a factor

$$C_{\text{diss}} = \frac{1}{1 + R} = 0.939 \pm 0.057.$$

4.3.8 Systematic Errors

The following uncertainties are considered as contributions to the systematic error on the measured cross sections. The errors are tabulated in Appendix C individually for every measured cross section bin.

- The energy calibration of the LAr and SPACAL calorimeters were varied by 4 % relative to the corresponding MC energy scale. For the LAr, this typically affects the cross sections by less than 20 % with sporadic exceptions. In the case of the SPACAL, the cross section is influenced up to 3 %.
- The fraction of events lost due to noise in the FMD is known to 25 %, which translates into a cross section error of 1.5 %.
- With the exception of the cross section in y^{had} , an uncertainty of up to 5 % results from the electron tagger acceptance and efficiency parameterization. For $d\sigma/dy^{\text{had}}$ the uncertainty is up to 18% in the highest bin.
- The uncertainties in the determination of the trigger efficiency and the luminosity affect the total cross section normalization by 8 % [Kau98] and 2 % [Lum96], respectively.

- The error resulting from a systematic variation of the normalization of the non-diffractive background is typically below 5 %.
- The uncertainty in the correction factor for proton dissociation translates into a cross section uncertainty of 6.1 %.

A description of the complete error treatment applied in the analysis is given in Appendix B.

Results

5.1 Cross Sections

The measured cross sections on stable hadron level are shown in the figures below. They are tabulated in Appendix C. The cross section kinematic range is given in Tab. 5.1.

5.2 Comparison to the Resolved Pomeron Model with Parton Distributions extracted from DDIS

The measured cross sections are compared to predictions from the Resolved Pomeron Model with pomeron parton densities extracted from inclusive DDIS and dijets in DDIS, i.e., the H1 QCD fit 2 result, which is compatible with the dijet data. In the following, this combination of the Resolved Pomeron Model and parton distributions is labelled ‘RPM DDIS.’ The photon is parameterized by GRV LO.

5.2.1 Test of hard QCD Scattering

Figs. 5.3 and 5.5 show the measured cross section differential in $\Delta\eta^{\text{j\text{et}}}$ and $\langle p_T^{\text{j\text{et}}} \rangle$, respectively. The RPM DDIS prediction lies above the data by a factor of 2.5. However, the predicted shapes of the distributions agree with the data within errors. The $\Delta\eta^{\text{j\text{et}}}$ and $\langle p_T^{\text{j\text{et}}} \rangle$ distributions are determined by the hard scattering subprocess. From the correct description of the shapes it is concluded that the hard scattering is well described by leading order QCD.

Cross Section Definition

$0.3 < y < 0.7$ $Q^2 < 0.01 \text{ GeV}^2$
$x_{IP} < 0.05$ $M_Y < 1.6 \text{ GeV}$ $-t < 1 \text{ GeV}^2$
CDFCONE, R=1 $p_T^{\text{jet}} > 4 \text{ GeV}$ $\# \text{ jets} \geq 2$ $-1 < \eta_{\text{jet}} < 2$

Tab. 5.1. Definition of cross sections on hadron level.

5.2.2 Cross Section differential in z_{IP}^{had}

The cross section $d\sigma/dz_{IP}^{\text{had}}$ is shown in Fig. 5.7. Not only does the prediction fail in the normalization, also the shape of the distribution is not described correctly.

The ratio of the measured to the predicted cross section in z_{IP}^{had} is shown in Fig. 5.1. The RPM DDIS agrees well with the data at large z_{IP}^{had} . In this regime, no pomeron spectator exists. At low z_{IP}^{had} , however, the RPM DDIS prediction lies significantly above the measurement. This behaviour can be described by a suppression factor $S(z_{IP})$ depending on z_{IP}^{true} , which has to be applied to the prediction from the RPM DDIS. The dependence on z_{IP} can be determined from the data. This is done in the following section.

5.2.3 Suppression Factor $S(z_{IP})$

The suppression factor $S(z_{IP})$ to the RPM DDIS is obtained by a fit of the Monte Carlo to the data. Only the first four bins of the cross sections are used for the fit, the bin $z_{IP}^{\text{had}} > 0.8$ is omitted (see below).

For every hadron level bin i , the histogram $d\sigma/dz_{IP}^{\text{true}}$ vs. $d\sigma/dz_{IP}^{\text{had}}$ is filled. Then the contributions from every true bin to i are weighted by a factor $S(z_{IP}^{\text{true}})$ according to the bin-centre value of z_{IP}^{true} :

$$\text{DATA}^i = \sum_{j=1}^5 S(z_{IP}^{\text{true}}(j)) \text{MC}^{ij},$$

in which $z_{IP}^{\text{true}}(j)$ denotes the value of z_{IP}^{true} at the centre of bin j . The χ^2 is given by

$$\chi^2 = \sum_{i=1}^4 \frac{\left(\text{DATA}^i - \sum_{j=1}^5 S(z_{IP}^{\text{true}}(j)) \text{MC}^{ij}\right)^2}{\sigma_{\text{data}}^2 + \sigma_{\text{MC}}^2}.$$

The following linear parameterization is used for the suppression factor:

$$S(z_{IP}) = a z_{IP}^{\text{true}}(j) + b.$$

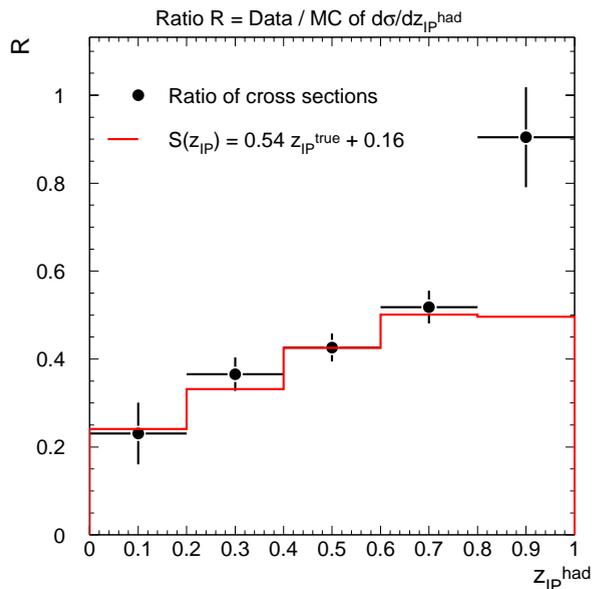


Fig. 5.1. Ratio data/RPM DDIS of z_{IP}^{had} differential cross sections (markers). A linear $S(z_{IP})$ is shown as the solid line.

The obtained fit parameters are

$$a = 0.54 \pm 0.13 \quad \text{and} \quad b = 0.16 \pm 0.06,$$

with a χ^2 of 0.22 for two degrees of freedom. The suppression factor is indicated as the histogram in Fig. 5.1.

In the following, the measured differential cross sections are discussed in comparison to the RPM DDIS weighted by an average factor of $S = 0.4$ (figure on top of page) and by $S(z_{IP})$ (figure at bottom of page).

The RPM DDIS cross section $d\sigma/dz_{IP}^{\text{had}}$ multiplied by $S(z_{IP})$ is shown in Fig. 5.8. Compared to the suppression by a constant factor $S = 0.4$ (cf. Fig. 5.7), the description is much improved. In the bin $z_{IP}^{\text{had}} > 0.8$, the MC deviates from the measurement. However, if the systematic errors on the data and the statistical uncertainty of the MC are taken into account, this deviation is less than 2σ . On detector level, this bin contains 10 % of the data events. Because this number is not too large, the discrepancy between data and prediction at large z_{IP}^{had} only weakly affects other kinematic distributions.

5.2.4 Cross Section differential in x_γ^{had}

The cross section differential in x_γ^{had} is shown in Fig. 5.9. The RPM DDIS describes the shape of the data distribution within errors. For the MC, contributions from different subprocesses are indicated. In this figure, all subprocesses are suppressed by a factor $S = 0.4$. In Fig. 5.2 the direct photon processes BGF ($g\gamma$) and QCD Compton ($q\gamma$) are not suppressed, whereas the other contributions are suppressed by a factor $S = 0.26$

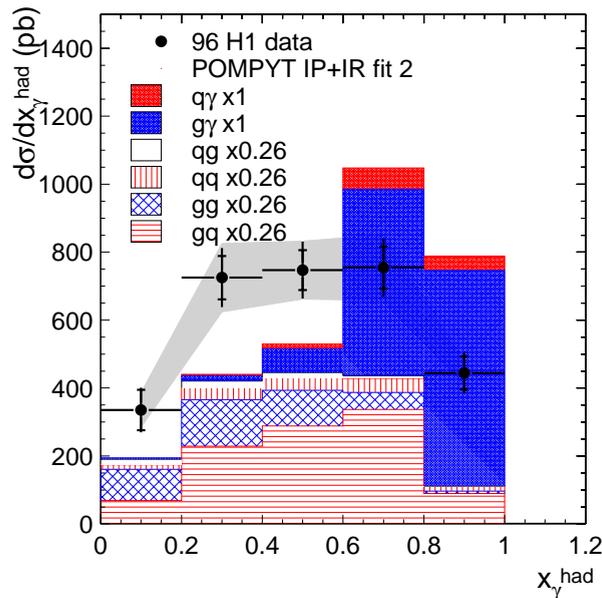


Fig. 5.2. Differential cross section $d\sigma/dx_\gamma^{\text{had}}$. The contributions to the RPM DDIS from different subprocesses are shown separately: direct photon processes BGF ($g\gamma$) and QCDC ($q\gamma$); quark-gluon process ($q\gamma$), where the quark comes from the pomeron; gluon-quark process (gq), where the gluon comes from the pomeron; quark-quark and gluon-gluon processes. The direct photon processes are unsuppressed, whereas the other contributions are suppressed by a factor $S = 0.26$ to normalize the MC to the same area as the H1 data.

to normalize the MC to the same area as the measured cross section. The discrepancy between the MC and the measurement then amounts to a χ^2 of 67 for 5 bins. The application of the suppression factor $S(z_{\mathcal{P}})$, which also suppresses direct photon processes, improves the description (cf. Fig. 5.10) compared to the overall factor $S = 0.4$ (cf. Fig. 5.9).

5.2.5 Cross Section differential in $x_{\mathcal{P}}^{\text{had}}$

Fig. 5.11 shows $d\sigma/d\log_{10}(x_{\mathcal{P}}^{\text{had}})$. The increase at small values of $x_{\mathcal{P}}^{\text{had}}$ is due to the requirement of two jets with $E_T > 4$ GeV: the energy that is accessible to the partons increases with rising $x_{\mathcal{P}}$. At high $\log_{10}(x_{\mathcal{P}}^{\text{had}})$, the logarithmic binning used in the figure conceals a decreasing $x_{\mathcal{P}}$ spectrum. The data cross section is linear in $\log_{10}(x_{\mathcal{P}}^{\text{had}})$, whereas the RPM DDIS exhibits a slightly steeper rise. The RPM DDIS cross section multiplied by $S(z_{\mathcal{P}})$ is shown in Fig. 5.12; the description is improved.

5.2.6 Cross Section differential in M_X^{had}

The differential cross section $d\sigma/dM_X^{\text{had}}$ is shown in Fig. 5.13. For $M_X^{\text{had}} > 22$ GeV, the shape of the data distribution is reproduced by the RPM DDIS. In the low M_X^{had}

region, however, the prediction deviates, but still describes the data within errors. The reweighting in $z_{\mathcal{P}}$ does not change M_X^{had} significantly (cf. Fig. 5.14).

5.2.7 Cross Section differential in $\langle \eta_{\text{jet}}^{\text{had}} \rangle$

In Fig. 5.15 the cross section differential in $\langle \eta_{\text{jet}}^{\text{had}} \rangle$ is shown. The RPM DDIS description of the shape is correct within errors. The reweighting with $S(z_{\mathcal{P}})$ slightly improves the agreement (cf. Fig. 5.16).

5.2.8 Cross Section differential in M_{12}^{had}

The cross section $d\sigma/dM_{12}^{\text{had}}$ is shown in Fig. 5.17. The data exhibit an exponential dependence on M_{12}^{had} . The shape is well described by the RPM DDIS. The rise of the distribution at low M_{12}^{had} is a kinematic effect. The reweighting in $z_{\mathcal{P}}$ leaves the distribution of the RPM DDIS nearly unchanged (cf. Fig. 5.18).

5.2.9 Cross Section differential in y^{had}

Fig. 5.19 shows the differential cross section $d\sigma/dy^{\text{had}}$, which is related to the cross section dependence on the γp centre-of-mass energy W . The shape is described by the RPM DDIS within errors. The deviation in the bin $0.55 \leq y^{\text{had}} \leq 0.6$ is statistically not very significant. The reweighting in $z_{\mathcal{P}}$ does not change the prediction significantly (cf. Fig. 5.20), because y is independent of the hard subprocess.

5.3 Summary of Results

The RPM DDIS fails in the description of the normalization of the data distributions by a factor of 2.5.

The shapes of the distributions are predicted reasonably well within errors. The application of a suppression factor $S(z_{\mathcal{P}}) = 0.54 z_{\mathcal{P}}^{\text{true}} + 0.16$ to the RPM DDIS leads to a consistent description of all variables. Direct photon processes are found to be suppressed as well.

Though not very significant with the present statistics, interactions with $z_{\mathcal{P}} = 1$ do not seem to be suppressed. It would be very interesting to study this regime with more statistics because it may point to subprocesses which contribute with $z_{\mathcal{P}} = 1$, e.g. 2 gluon exchange. These processes are not implemented in the MC. More data are needed to investigate S by measuring double differential cross sections in $z_{\mathcal{P}}$ and x_{γ} .

5.4 Comparison to previous Measurements

For the H1 1994 data, the photoproduction dijet cross sections differential in η_{jet} , p_T^{jet} , x_{γ}^{had} and $z_{\mathcal{P}}^{\text{had}}$ were measured [Adl99] for exactly two jets with $p_T^{\text{jet}} > 5$ GeV. The cross

sections obtained are higher than those measured in the present thesis, although from the decreasing p_T^{jet} spectrum a higher cross section is expected for an analysis of jets with $E_T > 4$ GeV.

Many cross checks have been performed in which no error was found in the present analysis. The different jet algorithm used in the old analysis changes the present cross sections by 15 % – 20 %. A repetition of the old analysis is presently under way to find the origin of the discrepancies.

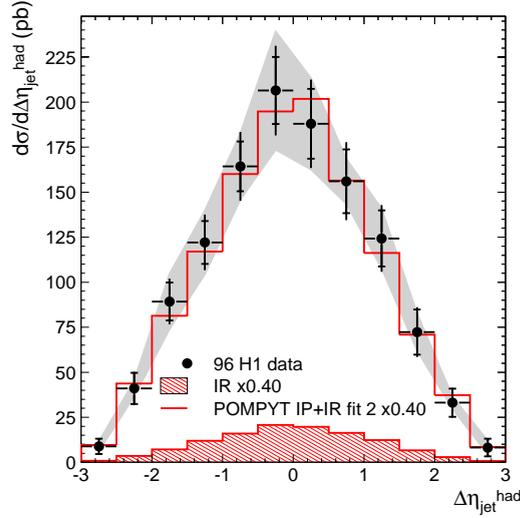


Fig. 5.3. Differential cross section $d\sigma/d\Delta\eta_{\text{jet}}^{\text{had}}$ as measured in this analysis (markers). The inner error bars represent the statistical errors, the outer error bars are the quadratic sum of statistical and uncorrelated systematic errors. The correlated systematic errors are shown separately as a shaded error band. The histogram shows the prediction of the Resolved Pomeron Model with pomeron and reggeon contributions as determined in DDIS (RPM DDIS), multiplied by an overall suppression factor $S = 0.4$. The reggeon is shown as the hatched histogram.

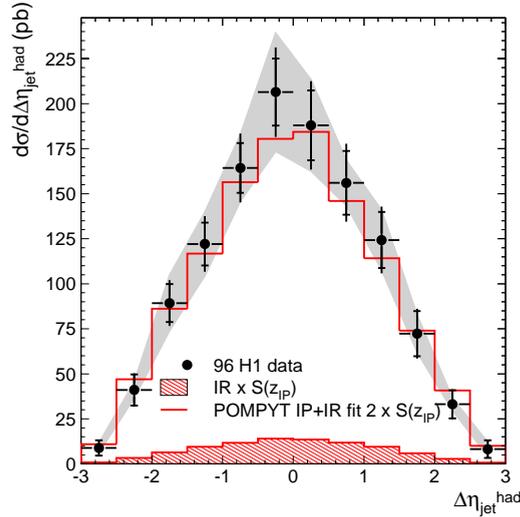


Fig. 5.4. Differential cross section $d\sigma/d\Delta\eta_{\text{jet}}^{\text{had}}$ as measured in this analysis (markers) and for the Resolved Pomeron Model with pomeron and reggeon contributions as determined in DDIS (RPM DDIS), reweighted by $S(z_{\text{IP}}) = 0.54 z_{\text{IP}}^{\text{true}} + 0.16$.

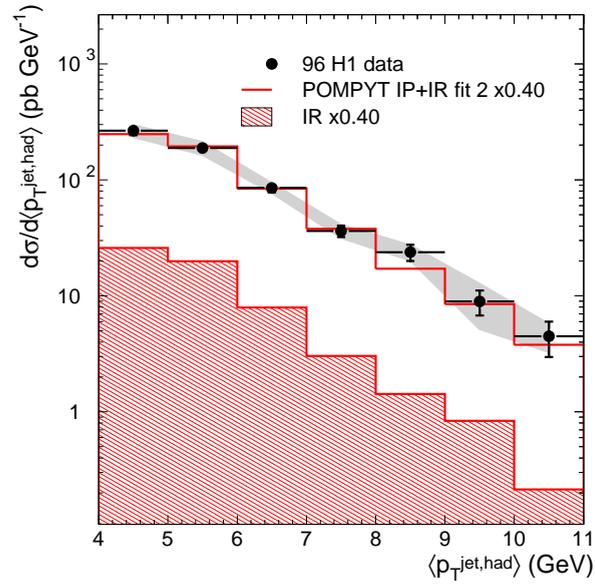


Fig. 5.5. Differential cross section $d\sigma/d\langle p_T^{\text{jet,had}} \rangle$. For an explanation see the caption of Fig. 5.3.

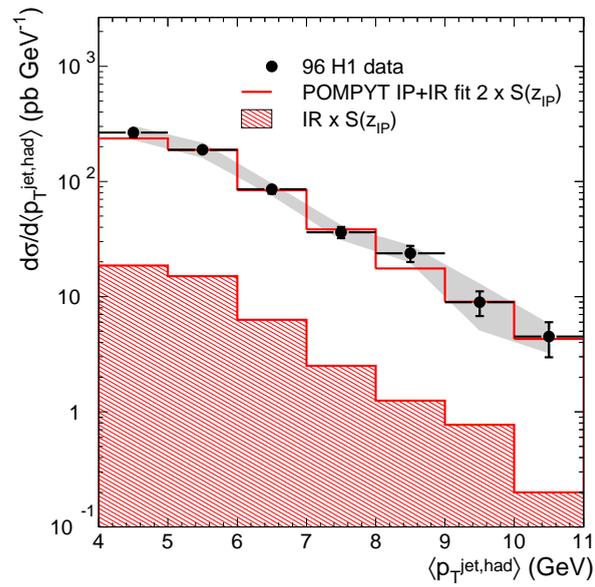


Fig. 5.6. Differential cross section $d\sigma/d\langle p_T^{\text{jet,had}} \rangle$. For an explanation see the caption of Fig. 5.4.

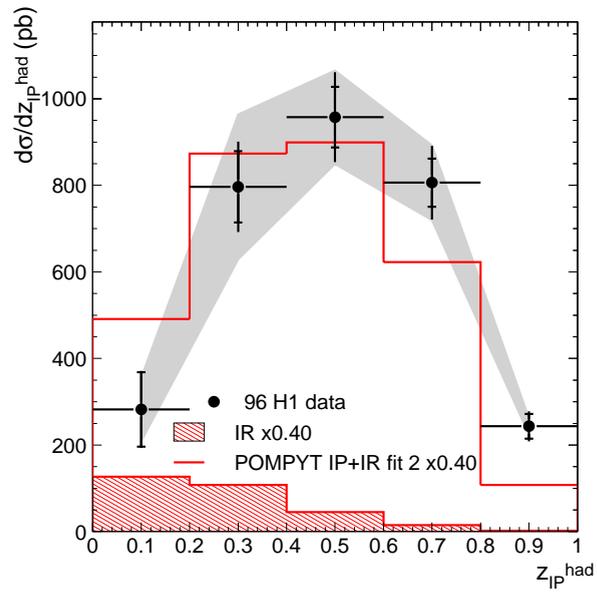


Fig. 5.7. Differential cross section $d\sigma/dz_{IP}^{had}$. For an explanation see the caption of Fig. 5.3.

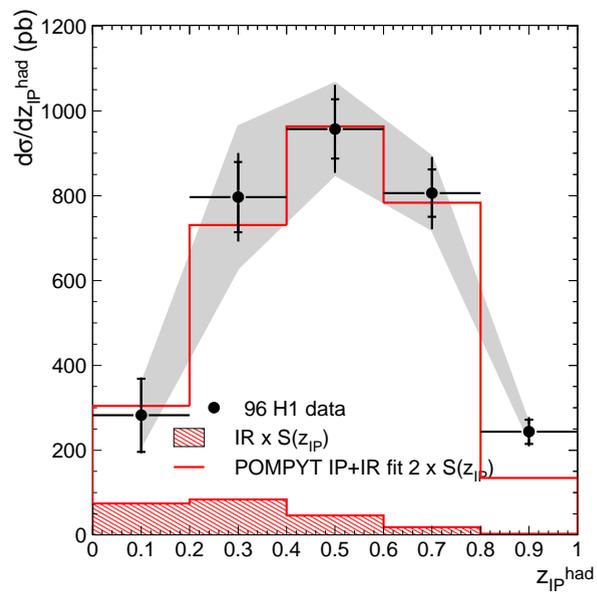


Fig. 5.8. Differential cross section $d\sigma/dz_{IP}^{had}$. For an explanation see the caption of Fig. 5.4.

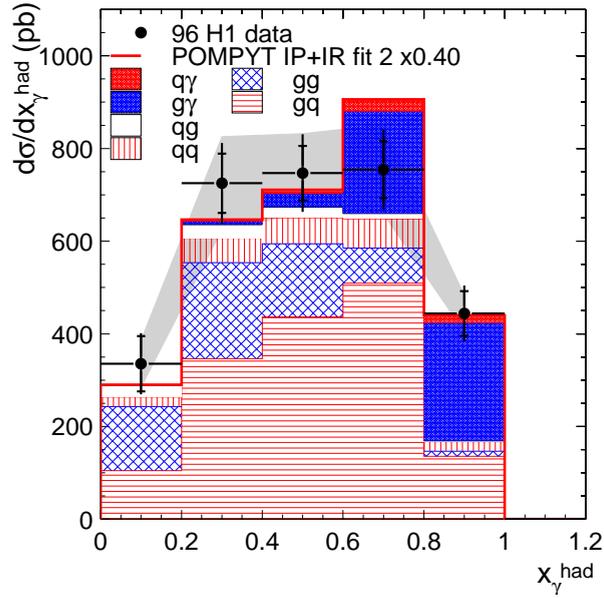


Fig. 5.9. Differential cross section $d\sigma/dx_\gamma^{\text{had}}$. The RPM DDIS prediction is scaled by an overall suppression factor $S = 0.4$. The contributions from the different subprocesses are shown separately: direct photon processes BGF ($q\gamma$) and QDC ($g\gamma$) and QDC ($q\gamma$); quark-gluon process (qg), where the quark comes from the pomeron; gluon-quark process (gq), where the gluon comes from the pomeron; quark-quark and gluon-gluon processes. For further explanation see the caption of Fig. 5.3.

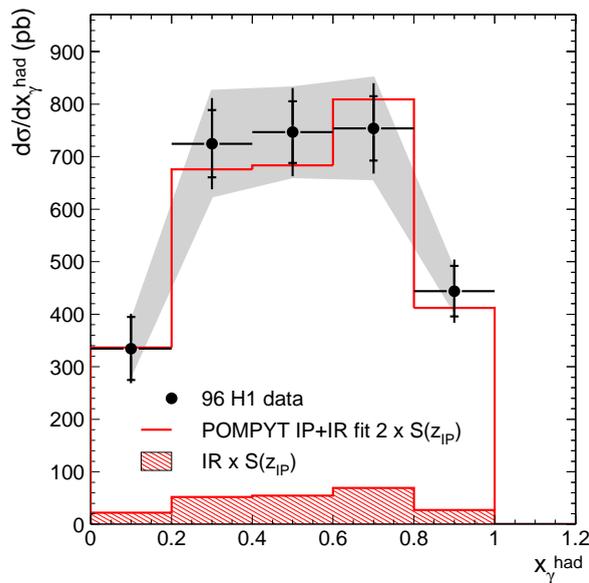


Fig. 5.10. Differential cross section $d\sigma/dx_\gamma^{\text{had}}$. For an explanation see the caption of Fig. 5.4.

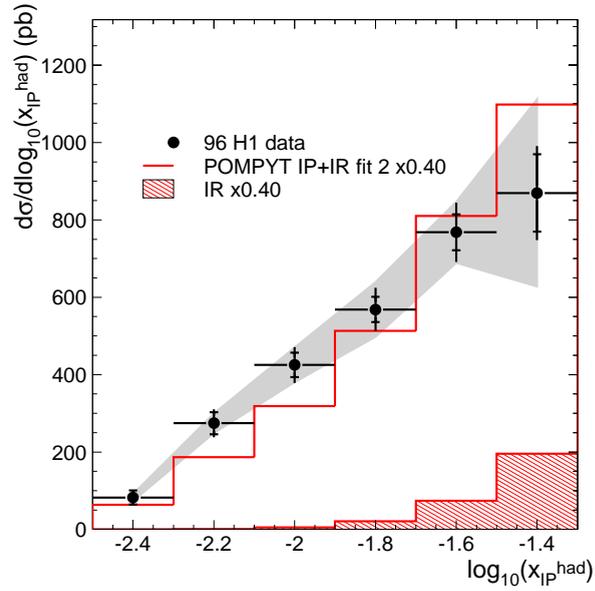


Fig. 5.11. Differential cross section $d\sigma/d\log_{10}(x_{IP}^{\text{had}})$. For an explanation see the caption of Fig. 5.3.

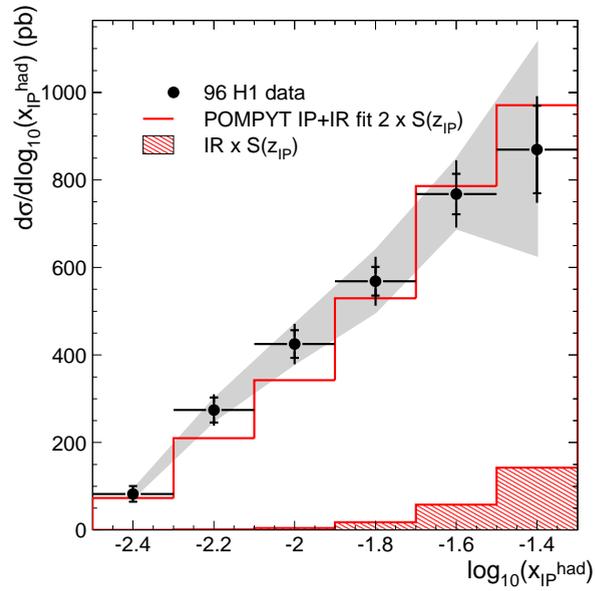


Fig. 5.12. Differential cross section $d\sigma/d\log_{10}(x_{IP}^{\text{had}})$. For an explanation see the caption of Fig. 5.4.

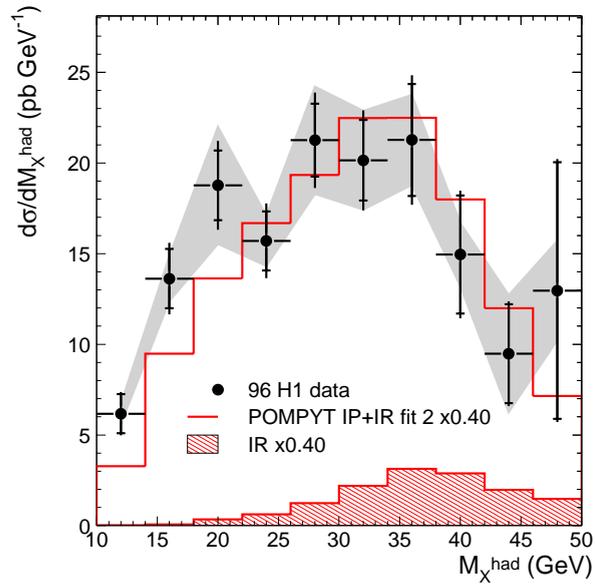


Fig. 5.13. Differential cross section $d\sigma/dM_X^{\text{had}}$. For an explanation see the caption of Fig. 5.3.

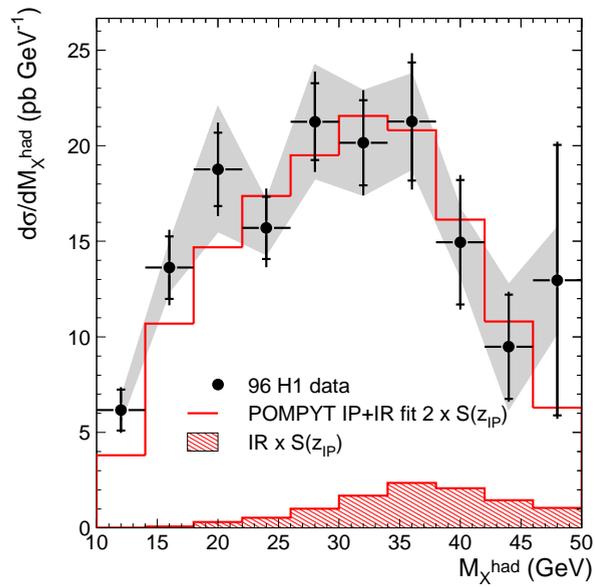


Fig. 5.14. Differential cross section $d\sigma/dM_X^{\text{had}}$. For an explanation see the caption of Fig. 5.4.

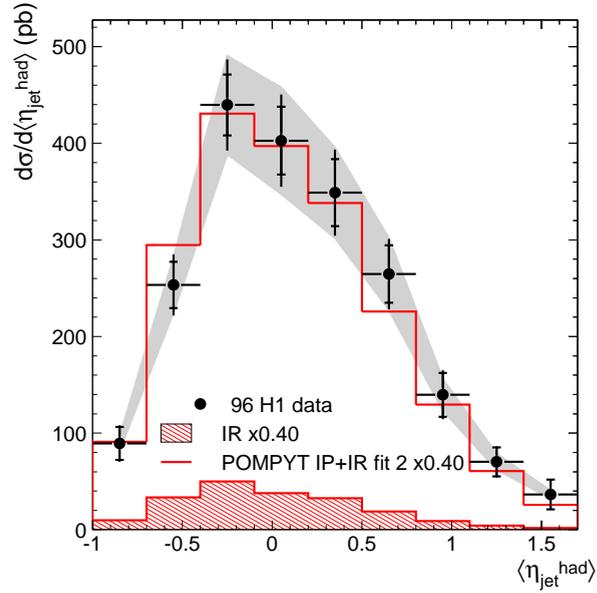


Fig. 5.15. Differential cross section $d\sigma/d\langle\eta_{\text{jet}}^{\text{had}}\rangle$. For an explanation see the caption of Fig. 5.3.

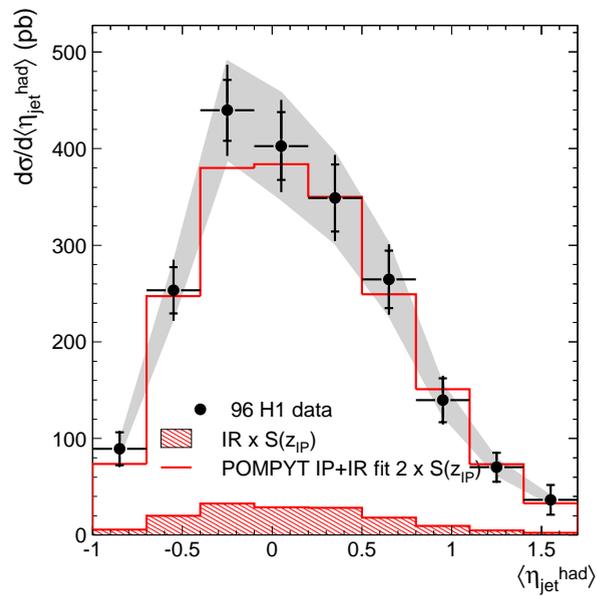


Fig. 5.16. Differential cross section $d\sigma/d\langle\eta_{\text{jet}}^{\text{had}}\rangle$. For an explanation see the caption of Fig. 5.4.

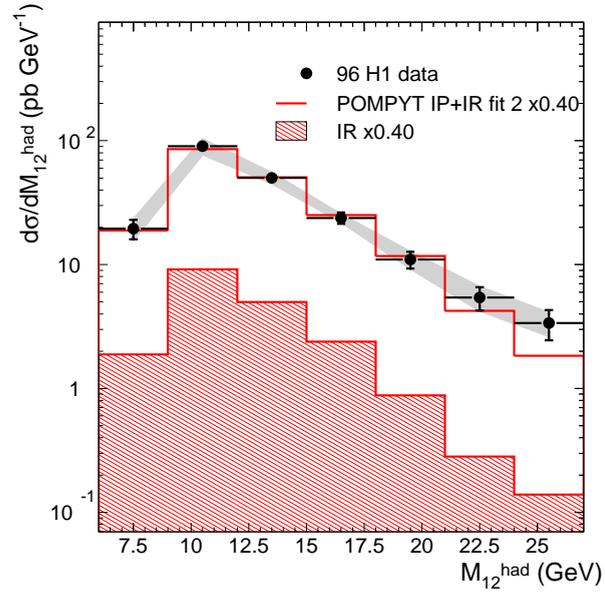


Fig. 5.17. Differential cross section $d\sigma/dM_{12}^{\text{had}}$. For an explanation see the caption of Fig. 5.3.

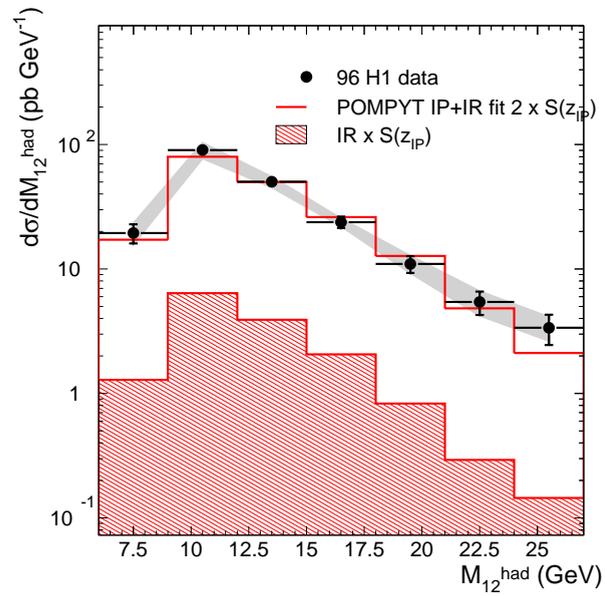


Fig. 5.18. Differential cross section $d\sigma/dM_{12}^{\text{had}}$. For an explanation see the caption of Fig. 5.4.

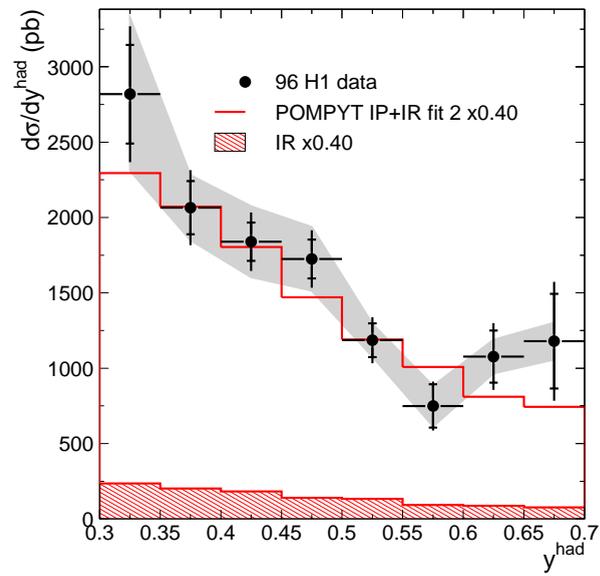


Fig. 5.19. Differential cross section $d\sigma/dy^{\text{had}}$. For an explanation see the caption of Fig. 5.3.

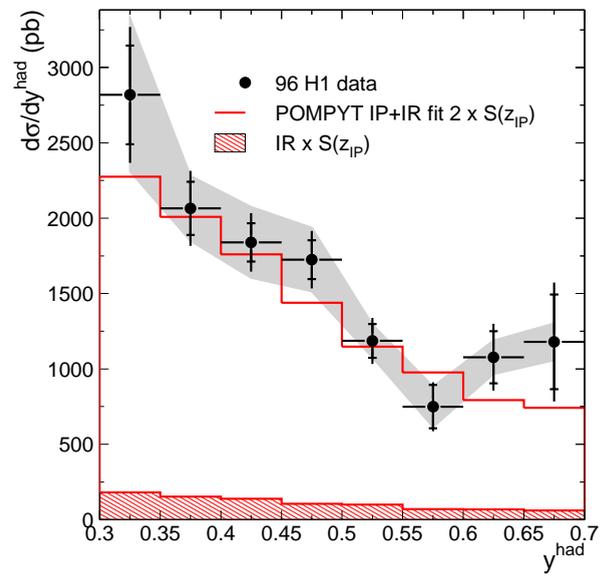


Fig. 5.20. Differential cross section $d\sigma/dy^{\text{had}}$. For an explanation see the caption of Fig. 5.4.

Conclusions and Outlook

This thesis presents measurements of diffractive photoproduction dijet cross sections with data recorded by the H1 experiment at the HERA ep collider. The cross sections are measured differentially as a function of a number of characteristic variables. The data are compared to the Resolved Pomeron Model with diffractive quark and gluon distributions as determined from inclusive and dijet diffractive deep inelastic scattering (RPM DDIS). The RPM DDIS describes the shapes of the differential cross sections reasonably well. However, the predicted cross sections are in average a factor of 2.5 higher than the measured cross sections.

A consistent description of both the normalization and the shapes is obtained by applying a suppression factor $S(z_{IP})$ to the RPM DDIS. The suppression factor S depends on the fractional pomeron momentum z_{IP} entering in the hard subprocess. A linear parameterization of $S(z_{IP})$ suffices to obtain a consistent description of the measured distributions.

Direct photon processes are found to be suppressed as well. Interactions between the pomeron and photon remnants are therefore not responsible for the filling of the gap. Instead, the measurements indicate that the gap destroying mechanism depends on the pomeron remnant but not on the photon remnant.

The investigation of the dependence of the suppression factor on z_{IP} and x_γ remains an exciting field of diffraction physics which can be pursued in the future with a larger data sample. Then double differential cross sections can be measured. In addition, comparative studies with a number of different existing diffraction models can be carried out, e.g. the Soft Colour Interaction Model or models for a gap survival probability. These models are

able to describe the diffractive dijet cross section measured for $p\bar{p}$ collision at Fermilab and it is interesting to see whether they can describe the γp data as well.

The results presented here are able to bridge the gap between DIS and $p\bar{p}$ collisions. Given the rather detailed information available, it can be expected that the γp data will be able to discriminate between the different models. In the limited time available for a diploma thesis these steps could not be carried out.

Bibliography

- [Abe97] F. Abe et al., *Phys. Rev. Lett.* **78** (1997) 2698;
T. Affolder et al., *Phys. Rev. Lett.* **84** (2000) 232.
- [Adl97] C. Adloff et al., *Z. Phys. C* **76** (1997) 613.
- [Adl99] C. Adloff et. al., *Eur. Phys. J. C* **6** (1999) 421.
- [Aff00] T. Affolder et al., *Phys. Rev. Lett.* **84** (2000) 5043.
- [And83] B. Andersson, et. al., *Phys. Rep.* **97** (1983) 31.
- [HER81] J.L. Augneres et. al., *HERA A Proposal for a large Electron-Proton Colliding Beam Facility at DESY*, DESY HERA 81/10, 1981.
- [Ber87] E. Berger et. al., *Nucl. Phys. B* **286** (1987) 704.
- [Bru94] R. Brun, et. al., *GEANT Long Writeup*, CERN Program Library **W5013**, 1994.
- [Bru93] P. Bruni, G. Ingelman, *Proc. of the Europhysics Conference, Marseilles, France, July 1993* 595; see also <http://www3.tsl.uu.se/thep/pompyt/>.
- [Col77] P.D.B. Collins, *An Introduction to Regge Theory and High Energy Physics*. Cambridge University Press, 1977.
- [Col98] J.C. Collins, *Phys. Rev. D* **57** (1998) 3051.
- [Der95] M. Derrick et al., *Z. Phys. C* **76** (1997) 613;
M. Derrick et al., *Phys. Lett. B* **356** (1995) 129;
M. Derrick et al., *Eur. Phys. J. C* **6** (1999) 43. 129.
- [Don92] A. Donnachie, P. Landshoff, *Phys. Lett. B* **296** (1992) 227.
- [Edi96] A. Edin et al., *Phys. Lett. B* **366** (1996) 371;
A. Edin et al., *Z. Phys. C* **75** (1997) 57.
- [Eil96] *Proc. Topical Conference on Hard Diffractive Processes*, Eilat, Israel, February 18-23, 1996.
- [Fri93] S. Frixione, M. Mangano, P. Nason, G. Ridolfi, *Phys. Lett. B* **319** (1993) 339.
- [Fro61] M. Froissart, *Phys. Rev.* **123** (1961) 1053;
A. Martin, *Phys. Rev.* **129** (1963) 1432.
- [Glü92] M. Glück et. al., *Phys. Rev. D* **46** (1992) 1973.
- [Goo60] M.L. Good, W.D. Walker, *Phys. Rev.* **120** (1960) 1854.

- [Gou83] K. Goulianos, *Phys. Rep.* **101** (1983) 169.
- [Gou00] K. Goulianos, *hep-ex/0011060*, 2000.
- [Det96] H1 Collaboration *The H1 Detector at HERA*. Internal Report DESY H1-96-01, 1996.
- [Hut90] J.E. Huth et. al., in: E.L. Berger (ed.) *Proc. of the 1990 Summer Study on High Energy Physics, Snowmass, Colorado*, World Scientific, Singapore, 1990;
F. Abe et. al., *Phys. Rev. D* **45** (1992) 1448;
S.D. Ellis, et. al., *Phys. Rev. Lett.* **69** (1992) 3615.
- [Ing85] G. Ingelman, P. Schlein, *Phys. Lett. B* **152** (1985) 256.
- [Jam98] F. James, *MINUIT Long Writeup*, CERN Program Library **D506**, 1998.
- [Kau98] O. Kaufmann, *PhD Thesis*, University of Heidelberg, 1998.
- [Lev] S. Levonian, *Help for the e-Tagger related Analyses*,
<http://www-h1.desy.de/~levonian/QPETAC.html>.
- [Lis93] B. List, *Diploma Thesis*, University of Berlin, 1993.
- [Lum96] S. Levonian
http://www-h1.desy.de/h1/www/h1det/lumi/summary_tables/summary.html.
- [Mar] J. Marks, *HFS—A Software Package To Cope With The Hadronic Final State*,
<http://www-h1.desy.de/iwork/iescale/hfs/hfs.html>.
- [Mar00] J. Marks, *private communication*.
- [Mey91] J. Meyer (ed.), *Guide to Simulation Program HISIM*, H1 Software Notes 03-11/89.
- [New96] P.R. Newman, *PhD thesis*, University of Birmingham, 1996.
- [Nic96] T. Nicholls et. al., *Nucl. Instr. Meth. A* **374** (1996) 149.
- [Rat99] J. Rathsmann, *Phys. Lett. B* **452** (1999) 364.
- [Reg59] T. Regge, *Nuovo Cimento* **14** (1959) 951;
T. Regge, *Nuovo Cimento* **18** (1960) 947.
- [Sch00] F.-P. Schilling, *PhD Thesis*, University of Heidelberg, 2000.
- [Sey94] M.H. Seymour, *Z. Phys. C* **62** (1994) 127.
- [Sjö86] T. Sjöstrand, *Computer Physics Commun.* **39** (1986) 347;
T. Sjöstrand, M. Bengtsson, *Computer Physics Commun.* **43** (1987) 367.

χ^2 Fit of x_{IP}^{det}

The data distribution of x_{IP}^{det} is fitted by the sum of PYTHIA and POMPYT event distributions. The fit determines the normalization factors that have to be applied to the MC events to describe the data. The following procedure is adopted: first, the normalized distributions are fitted (shape fit) and the factors for the unnormalized sum are calculated afterwards from the result of the shape fit.

The event samples used in the fit are the events on detector level remaining after all cuts except for the cuts in x_{IP}^{det} and η_{max} . x_{IP}^{det} is left unrestricted, because this is the fit variable. Because of the close relation between x_{IP}^{det} and η_{max} (x_{IP}^{det} is most sensitive to energy in the forward region, cf. Eq. (2.17)), a too harsh restriction of η_{max} would limit x_{IP}^{det} as well. The upper limit on η_{max} is therefore chosen to be 3.2.

For the fit, the PYTHIA MC is also used in the M_Y^{had} region in which the DIFFVM correction for proton dissociation is applied.

A.1 Shape Fit

This section describes the fit procedure applied to the normalized event distributions.

Let DATA, PYTHIA and POMPYT be the unnormalized distributions of the data, PYTHIA and POMPYT, respectively and DA, PY and PP denote the corresponding normalized distributions, such that for every bin i

$$\begin{aligned} \text{DA}(i) &= \text{DATA}(i)/N_{\text{Data}}, \\ \text{PY}(i) &= \text{PYTHIA}(i)/N_{\text{Pythia}}, \\ \text{PP}(i) &= \text{POMPYT}(i)/N_{\text{Pompyt}}, \end{aligned}$$

in which the N_j denote the total number of events in the unnormalized samples.

Then the fit reads

$$\text{DA}(i) = a \text{PY}(i) + (1 - a) \text{PP}(i), \quad (\text{A.1})$$

with the single fit parameter a .

The χ^2 is then defined as

$$\chi^2 \equiv \sum_i \left(\frac{\mathcal{D}(i)}{\delta \mathcal{D}(i)} \right)^2,$$

with

$$\mathcal{D} \equiv \text{DA}(i) - a \text{PY}(i) - (1 - a) \text{PP}(i).$$

The square of the uncertainty in \mathcal{D} is given by

$$(\delta \mathcal{D})^2 = \left(\frac{\partial \mathcal{D}}{\partial \text{DA}} \delta \text{DA} \right)^2 + \left(\frac{\partial \mathcal{D}}{\partial \text{PY}} \delta \text{PY} \right)^2 + \left(\frac{\partial \mathcal{D}}{\partial \text{PP}} \delta \text{PP} \right)^2,$$

with

$$\begin{aligned} \delta \text{DA}(i) &= \sqrt{\text{DATA}(i)/N_{\text{Data}}}, \\ \delta \text{PY}(i) &= \sqrt{\text{PYTHIA}(i)/N_{\text{Pythia}}}, \\ \delta \text{PP}(i) &= \sqrt{\text{POMPYPY}(i)/N_{\text{Pompyt}}}. \end{aligned}$$

Then

$$(\delta \mathcal{D})^2 = \frac{\text{DATA}(i)}{N_{\text{Data}}^2} + a^2 \frac{\text{PYTHIA}(i)}{N_{\text{Pythia}}^2} + (1 - a)^2 \frac{\text{POMPYPY}(i)}{N_{\text{Pompyt}}^2},$$

and

$$\chi^2 = \sum_i \frac{(\text{DA}(i) - a \text{PY}(i) - (1 - a) \text{PP}(i))^2}{\frac{\text{DA}(i)}{N_{\text{Data}}} + a^2 \frac{\text{PY}(i)}{N_{\text{Pythia}}} + (1 - a)^2 \frac{\text{PP}(i)}{N_{\text{Pompyt}}}}.$$

The fit range is chosen according to the diffractive region $x_{\mathbb{P}}^{\text{det}} < 0.05$ and such that DATA, PYTHIA and POMPYPY are larger than 10 in every bin. The unnormalized distributions are shown in Fig. A.1, where also the fit range is indicated. The fitting itself is done using of the minimization package MINUIT [Jam98]. The result is $a = 0.40 \pm 0.05$. The obtained χ^2 is 5.6 for four bins and one parameter, corresponding to 1.87 per degree of freedom. The fit suffers from the absence of a meson MC.

A.2 Factors to unnormalized Monte Carlo Events

This section describes how the actual normalization factors to the MC events are obtained from the fit parameter a .

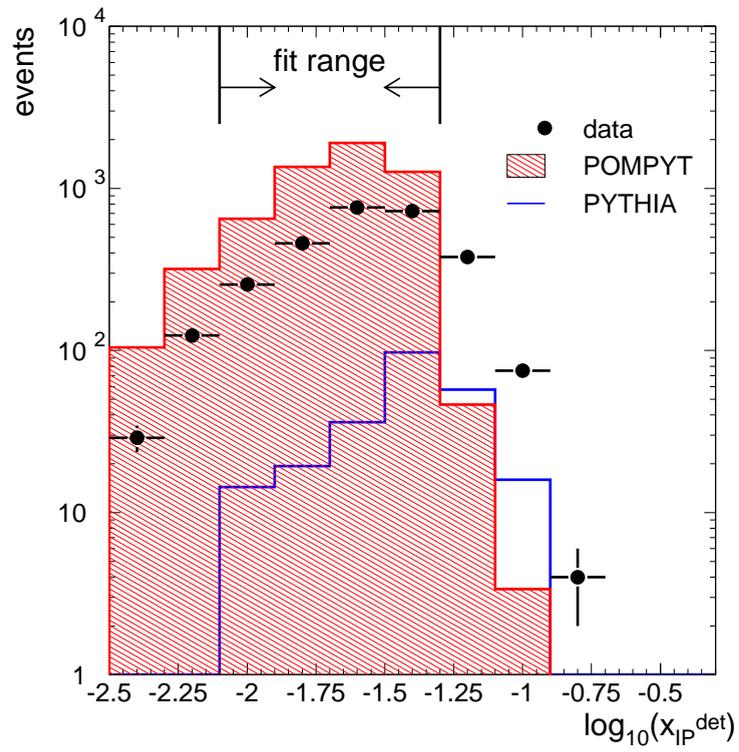


Fig. A.1. Unnormalized distributions as used in the x_{IP}^{det} fit. The samples do not correspond to the same luminosity.

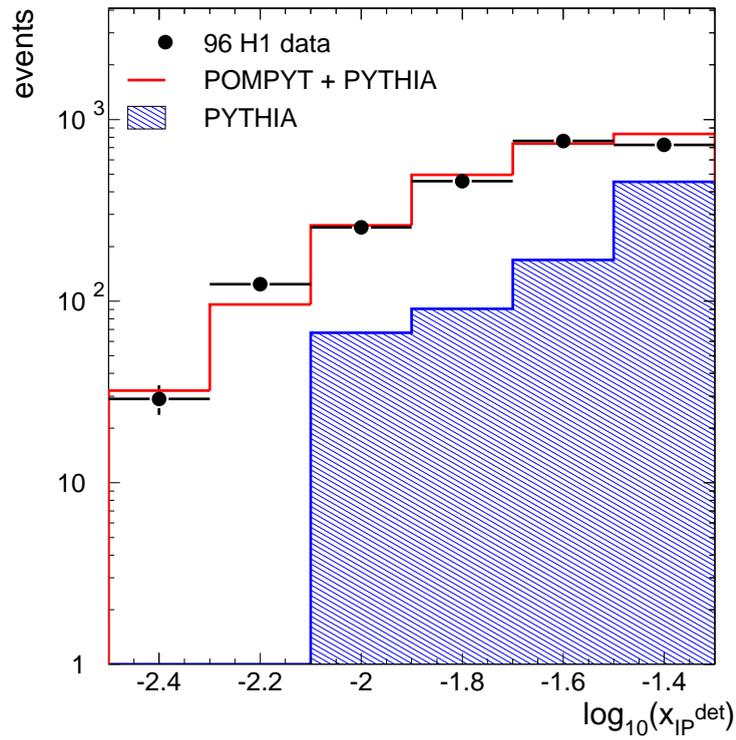


Fig. A.2. Result of the fit to $x_{\mathbb{P}}^{\text{det}}$. Shown is the region $x_{\mathbb{P}}^{\text{det}} < 0.05$. For the fit, $\eta_{\text{max}} < 3.2$ and the PYTHIA MC is used also in the region $m_p < M_Y^{\text{had}} < 5$ GeV.

From a the factors b and c of the MC sum with the MCs scaled to the luminosity of the data sample can be calculated.

$$\text{DATA} = b \text{PYTHIA} \frac{L_{\text{Data}}}{L_{\text{Pythia}}} + c \text{POMPYT} \frac{L_{\text{Data}}}{L_{\text{Pompyt}}}.$$

Dividing both sides by N_{Data} yields

$$\frac{\text{DATA}}{N_{\text{Data}}} = b \text{PYTHIA} \frac{L_{\text{Data}}}{L_{\text{Pythia}} N_{\text{Data}}} + c \text{POMPYT} \frac{L_{\text{Data}}}{L_{\text{Pompyt}} N_{\text{Data}}},$$

which can be compared with Eq. (A.1):

$$b = \frac{N_{\text{Data}}}{N_{\text{Pythia}}} \frac{L_{\text{Pythia}}}{L_{\text{Data}}} a, \tag{A.2}$$

$$c = \frac{N_{\text{Data}}}{N_{\text{Pompyt}}} \frac{L_{\text{Pompyt}}}{L_{\text{Data}}} (1 - a). \tag{A.3}$$

The result of the fit is shown in Fig. A.2 in the region $x_{\mathbb{P}}^{\text{det}} < 0.05$. The contributions from PYTHIA include events in the DIFFVM region $m_p < M_Y^{\text{had}} < 5$ GeV. The sharp drop-off of the PYTHIA events at $\log_{10}(x_{\mathbb{P}}^{\text{det}}) = -2.1$ stems from the limited statistics of the PYTHIA MC.

Appendix B

Error Treatment

This appendix describes the error treatment applied in the analysis to derive the systematic and statistical uncertainties of the measured cross sections.

The cross section differential in the variable x in bin i is given by

$$\frac{d\sigma^i}{dx} = \frac{N_{\text{data}}^i - N_{\text{non-diffr.}}^i}{C_\varepsilon^i} \frac{C_{\text{FMD}} C_{\text{diss}}}{L \Delta x}.$$

It is proportional to the number of events corrected for non-diffractive background, divided by the correction factor C_ε^i , which takes into account migrations and the efficiency to detect a diffractive event. C_{FMD} and C_{diss} are the correction factors for noise in the Forward Muon Detector and for proton dissociation, respectively. Δx is the bin width of the differential cross section and L is the integrated luminosity.

B.1 Sources of Uncertainty

Number of Data Events N_{data}^i

The number of detected diffractive events is distributed according to Poisson statistics. The absolute error on N_{data}^i is therefore given by $\sqrt{N_{\text{data}}^i}$.

Number of non-diffractive Background Events $N_{\text{non-diffr.}}^i$

The PYTHIA MC is used to simulate non-diffractive background in the range $x_{\text{IP}}^{\text{had}} > 0.05$. Therefore, all PYTHIA events in the detector sample¹ are migrational background.

¹. The detector sample is defined by the events that pass the detector level diffractive cuts. In the same way the hadron sample is defined.

These events were generated with weights, to enhance a certain kinematic range.² The uncertainty on $\text{PYTHIA}^{\text{det}}$ is therefore not given by the Poissonian distribution. The statistical error of N events with weights w_i is given by

$$\sigma = \sqrt{\sum_{i=1}^N w_i^2}. \quad (\text{B.1})$$

The absolute normalization of the non-diffractive background is obtained from the $x_{\text{IP}}^{\text{det}}$ fit:

$$N_{\text{non-diffr.}}^i = b \text{PYTHIA}^{\text{det}}(i),$$

in which b is correlated to the fit parameter a by Eq. (A.2). The statistical error on $N_{\text{non-diffr.}}^i$ is calculated by scaling the error on the number of PYTHIA events, which is obtained according to Eq. (B.1), by the normalization factor b . The error on the fit parameter a systematically affects the number of non-diffractive background events. The change in the cross section when a is varied by its error is considered the systematic error on the cross section related to a . This systematic error is correlated among the bins, because a shift in a directly translates into the number of background corrected data events.

Correction Factor C_{ε}^i

The data need to be corrected for the efficiency to detect a diffractive event and for migration effects among the bins and from outside the hadron level kinematic range into the detector level diffractive sample. The correction factor is given by (cf. Sec. 4.3.4)

$$C_{\varepsilon}^i = \varepsilon_{\text{trig}}^i \varepsilon_{\text{etag}}^i \left(\varepsilon_{\text{rec}}^i + \text{mig} \right), \quad (\text{B.2})$$

with the trigger efficiency $\varepsilon_{\text{trig}}^i$, the etagger efficiency $\varepsilon_{\text{etag}}^i$, the reconstruction efficiency $\varepsilon_{\text{rec}}^i$ and the migrations into the detector level diffractive sample. The treatment of the individual uncertainties related to the quantities in Eq. (B.2) is discussed in the following paragraphs.

Trigger Efficiency $\varepsilon_{\text{trig}}^i$

The trigger efficiency $\varepsilon_{\text{trig}}$ is taken from the trigger simulation in H1SIM , which is accurate within 8 % for all bins, as shown in a previous analysis [Kau98]. This error is not correlated among the bins.

². The MC files were originally created for a different analysis.

Etagger Efficiency $\varepsilon_{\text{etag}}^i$

The etagger efficiency $\varepsilon_{\text{etag}}^i$ is given for each event individually as a weight calculated using the parameterization routine QPETAC on the basis of the true value of the inelasticity y . The change in the cross section resulting from the variation of y^{true} by $\pm 1.5\%$ is attributed to the uncertainty on $\varepsilon_{\text{etag}}^i$. The uncertainty is not correlated among the bins.

Reconstruction Efficiency $\varepsilon_{\text{rec}}^i$

Apart from etagger and trigger effects, the reconstruction efficiency $\varepsilon_{\text{rec}}^i$ is the probability to detect a diffractive event. Then the detection process can be thought of as being of the *Bernoulli* type: the event is either detected (with probability $\varepsilon_{\text{rec}}^i$) or not detected (with probability $1 - \varepsilon_{\text{rec}}^i$). The probability to detect k out of N diffractive events is then given by the binomial distribution

$$\binom{N}{k} (\varepsilon_{\text{rec}}^i)^k (1 - \varepsilon_{\text{rec}}^i)^{N-k}.$$

The mean value \bar{k} and the rms-deviation $\sigma_{\bar{k}}$ are given by

$$\bar{k} = N \varepsilon_{\text{rec}}^i, \quad \sigma_{\bar{k}} = \sqrt{N \varepsilon_{\text{rec}}^i (1 - \varepsilon_{\text{rec}}^i)}.$$

By considering $\varepsilon_{\text{rec}}^i$ as variable, these formulas can be used to derive the error for the efficiency:

$$\sigma_{\varepsilon_{\text{rec}}^i} = \sigma_{\bar{k}}/N = \sqrt{\varepsilon_{\text{rec}}^i (1 - \varepsilon_{\text{rec}}^i)/N}.$$

The uncertainty is of statistical nature and not correlated among the bins.

Migrations into Detector Sample

The last term in Eq. (4.6) describes the migrations into the detector sample. It is given by the ratio of the number of POMPYT events in the detector level sample which are not part of the hadron level sample to the number of POMPYT events in the hadron sample (cf. Sec. 4.3.4). The event samples in the nominator and the denominator of the ratio are therefore independent from each other. The errors for nominator and denominator can thus be calculated separately according to Eq. (B.1) and the resulting relative errors are quadratically added. The resulting error is pure statistical and not correlated among the bins.

Energy Calibration of Calorimeters

The energy scale of the LAr and SPACAL calorimeter are known within 4% relative to the MC energy scale. The change observed in the cross section when shifting the LAr calorimeter energy scale by 4% is therefore attributed to the uncertainty in the energy scale. The same is done separately for the SPACAL calorimeter. The resulting errors of the cross sections are correlated among all bins.

Correction Factors C_{FMD} and C_{diss} and Luminosity

The relative errors on C_{FMD} , C_{diss} and L are taken from other analyses. All three uncertainties are correlated among the bins, because a shift in these quantities directly translates into a shift of the cross section ('scaling errors').

B.2 Statistical Errors

Statistical errors are the Poissonian uncertainty in the number of uncorrected data events, the statistical uncertainties in the numbers of non-diffractive PYTHIA and migrational POMPYT events, and the error on the reconstruction efficiency.

The absolute uncertainties on the data and the PYTHIA events are quadratically added, and the resulting error is translated into a relative uncertainty on the number of background-corrected data events.

The absolute uncertainties in the number of migration events and the reconstruction efficiency are quadratically added. The resulting absolute error is translated into the relative statistical error on C_{ε}^i .

The relative uncertainty on the number of background-corrected data events and the relative statistical error on the correction factor C_{ε}^i are quadratically summed, yielding the total relative statistical error of the cross section. The corresponding absolute uncertainty is shown as the inner error bar in the cross section histogram.

B.3 Systematic Errors

B.3.1 Uncorrelated Systematic Errors

Uncorrelated systematic errors are the uncertainty on the trigger efficiency and the error attributed to the uncertainty in the etagger efficiency. The corresponding relative errors are quadratically summed, yielding the total uncorrelated systematic error of the cross section.

The relative uncorrelated systematic error and the total relative statistical error are added quadratically. The resulting error is translated into an absolute uncertainty on the cross section and is shown as the total error bar in the cross section histogram.

B.3.2 Correlated Systematic Errors

The systematic errors originating from the following sources are correlated among the bins: energy scale of calorimeters, fit in $x_{\text{IP}}^{\text{det}}$, correction factors for FMD noise and proton dissociation, and luminosity.

The quadratic sum of their relative errors constitutes the total relative correlated systematic error of the cross section measurement. The corresponding absolute value of this error is shown as a shaded error band in the cross section histograms.

Appendix C

Tabulated Cross Sections

The measured cross sections are tabulated on the following pages. The statistical and systematic error contributions are shown separately for every bin. The systematic error is separated into an uncorrelated contribution ('syst. uncorr.')

 and a correlated contribution ('syst. corr.') which corresponds to the error band in the cross section histograms. The error resulting from the normalization of the non-diffractive background is labelled 'non-diffr. norm.' For an explanation of the other quantities see Appendix B.

$$d\sigma / d\Delta\eta_{\text{jet}}^{\text{had}}$$

Bin	1	2	3	4	5	6	7	8	9	10	11	12
$\Delta\eta_{\text{jet}}^{\text{had}}$ min,max	-3,-2.5	-2.5,-2	-2,-1.5	-1.5,-1	-1,-0.5	-0.5,0	0,0.5	0.5,1	1,1.5	1.5,2	2,2.5	2.5,3
$d\sigma/d\Delta\eta_{\text{jet}}^{\text{had}}$ (pb)	8	41	89	122	164	206	188	156	124	72	33	8
Errors:												
stat. (%)	48.4	21.2	11.7	9.8	8.4	9.0	10.3	11.3	12.5	17.3	23.7	59.7
syst. uncorr. (%)	8.1	8.0	8.0	8.0	8.0	8.0	8.0	8.0	8.0	8.0	8.0	8.1
syst. corr. (%)	29.0	10.6	17.2	14.4	11.2	15.8	13.5	8.0	13.3	14.1	10.0	45.2

statistical errors (%)

$N_{\text{data}} - N_{\text{nd}}$	44.7	19.2	10.6	8.9	7.6	8.2	7.2	8.2	9.3	12.0	18.3	44.7
C_{ϵ}	18.6	8.9	5.1	4.1	3.7	3.7	7.3	7.8	8.5	12.5	15.2	39.6

systematic errors (%)

uncorrelated												
ϵ_{trig}	8											
ϵ_{etag}	1.0	0.4	0.3	0.4	0.2	0.3	0.5	0.4	0.2	0.2	0.4	1.3
correlated												
non-diffr. norm.	0.0	0.0	0.6	2.0	2.1	5.6	2.3	1.0	2.0	0.0	0.0	0.0
LAr	20.0	3.7	15.5	12.6	8.3	12.4	11.4	4.0	11.1	7.2	6.7	20.0
SPACAL	20.0	7.4	3.3	0.7	2.8	4.6	1.4	1.7	2.4	10.1	3.3	40.0
correlated, scale												
C_{FMD}	1.5											
C_{diss}	6.1											
L	2											

$$d\sigma / d\langle p_T^{\text{jet,had}} \rangle$$

Bin	1	2	3	4	5	6	7
$\langle p_T^{\text{jet,had}} \rangle$ (GeV) min,max	4,5	5,6	6,7	7,8	8,9	9,10	10,11
$d\sigma / d\langle p_T^{\text{jet,had}} \rangle$ (pb GeV ⁻¹)	265	188	85	36	23	8	4
Errors:							
stat. (%)	8.4	7.0	8.7	11.2	16.0	24.2	33.6
syst. uncorr. (%)	8.0	8.0	8.0	8.0	8.1	8.1	8.2
syst. corr. (%)	11.8	12.8	9.9	12.8	15.1	41.9	26.8

statistical errors (%)

$N_{\text{data}} - N_{\text{nd}}$	5.3	5.1	7.0	10.3	13.9	22.3	31.1
C_ϵ	6.5	4.7	5.2	4.5	8.0	9.4	12.9

systematic errors (%)

uncorrelated							
ϵ_{trig}	8						
ϵ_{etag}	0.3	0.2	0.6	0.8	1.1	1.3	1.7
correlated							
non-diffr. norm.	3.3	2.6	1.0	3.0	0.0	12.0	7.2
LAr	8.8	10.5	7.2	10.3	13.5	39.3	25.0
SPACAL	2.7	1.4	1.4	2.1	1.9	4.4	0.0
correlated, scale							
C_{FMD}	1.5						
C_{diss}	6.1						
L	2						

$$d\sigma / dz_{IP}^{\text{had}}$$

Bin	1	2	3	4	5
z_{IP}^{had} min,max	0,0.2	0.2,0.4	0.4,0.6	0.6,0.8	0.8,1
$d\sigma / dz_{IP}^{\text{had}}$ (pb)	283	797	958	806	243
Errors:					
stat. (%)	30.3	10.3	7.3	6.9	11.7
syst. uncorr. (%)	8.2	8.0	8.0	8.0	8.0
syst. corr. (%)	25.4	20.9	11.2	10.7	7.7

statistical errors (%)

$N_{\text{data}} - N_{\text{nd}}$	24.8	7.7	5.3	4.8	7.7
C_{ε}	17.4	6.8	5.0	4.9	8.8

systematic errors (%)

uncorrelated					
$\varepsilon_{\text{trig}}$	8				
$\varepsilon_{\text{etag}}$	1.8	0.6	0.4	0.3	0.5
correlated					
non-diffr. norm.	19.9	5.6	2.7	0.4	0.0
LAr	14.0	18.6	8.7	8.4	3.6
SPACAL	3.5	4.1	0.3	1.4	1.8
correlated, scale					
C_{FMD}	1.5				
C_{diss}	6.1				
L	2				

$$d\sigma / dx_{\gamma}^{\text{had}}$$

Bin	1	2	3	4	5
x_{γ}^{had} min,max	0,0.2	0.2,0.4	0.4,0.6	0.6,0.8	0.8,1
$d\sigma / dx_{\gamma}^{\text{had}}$ (pb)	326	705	726	734	432
Errors:					
stat. (%)	17.8	8.8	7.9	8.1	10.9
syst. uncorr. (%)	8.3	8.1	8.0	8.0	8.1
syst. corr. (%)	15.2	13.9	11.4	12.8	8.9

statistical errors (%)

$N_{\text{data}} - N_{\text{nd}}$	12.6	5.9	5.5	6.3	8.2
C_{ϵ}	12.6	6.6	5.6	5.1	7.2

systematic errors (%)

uncorrelated					
ϵ_{trig}	8				
ϵ_{etag}	5.2	4.2	3.2	3.6	4.3
correlated					
non-diffr. norm.	5.8	1.9	1.9	2.2	1.9
LAr	8.2	9.6	5.7	8.0	3.0
SPACAL	1.0	1.8	1.4	0.3	4.1
correlated, scale					
C_{FMD}	1.5				
C_{diss}	6.1				
L	2				

$$d\sigma / d\log_{10}(x_{IP}^{\text{had}})$$

Bin	1	2	3	4	5	6
$\log_{10}(x_{IP}^{\text{had}})$ min,max	-2.5,-2.3	-2.3,-2.1	-2.1,-1.9	-1.9,-1.7	-1.7,-1.5	-1.5,-1.3
$d\sigma/d\log_{10}(x_{IP}^{\text{had}})$ (pb)	82	274	425	568	768	871
Errors:						
stat. (%)	21.7	10.3	7.4	5.7	6.0	11.4
syst. uncorr. (%)	8.1	8.0	8.0	8.0	8.0	8.0
syst. corr. (%)	10.8	9.1	10.5	12.4	10.2	27.7

statistical errors (%)

$N_{\text{data}} - N_{\text{nd}}$	19.6	9.1	6.6	5.3	5.5	10.4
C_{ε}	9.4	5.0	3.3	2.2	2.5	4.7

systematic errors (%)

uncorrelated						
$\varepsilon_{\text{trig}}$	8					
$\varepsilon_{\text{etag}}$	1.1	0.2	0.3	0.4	0.3	0.4
correlated						
non-diffr. norm.	3.2	0.0	0.9	0.3	3.3	8.4
LAr	7.1	5.7	8.1	10.3	6.9	25.6
SPACAL	3.6	2.5	0.9	1.9	1.7	0.0
correlated, scale						
C_{FMD}	1.5					
C_{diss}	6.1					
L	2					

$$d\sigma/dM_X^{\text{had}}$$

Bin	1	2	3	4	5	6	7	8	9	10
M_X^{had} (GeV) min,max	10,14	14,18	18,22	22,26	26,30	30,34	34,38	38,42	42,46	46,50
$d\sigma/dM_X^{\text{had}}$ (pb GeV ⁻¹)	6	13	18	15	21	20	21	14	9	12
Errors:										
stat. (%)	17.4	12.0	10.3	10.3	9.4	11.0	14.5	21.8	28.7	54.6
syst. uncorr. (%)	8.3	8.1	8.1	8.0	8.0	8.1	8.4	8.9	10.0	12.2
syst. corr. (%)	8.8	9.0	17.2	8.8	13.9	13.5	11.6	11.5	34.0	21.1

statistical errors (%)

$N_{\text{data}} - N_{\text{nd}}$	14.4	8.3	6.4	8.1	6.8	8.1	10.0	15.6	23.6	31.6
C_ε	9.8	8.6	8.1	6.4	6.6	7.5	10.5	15.1	16.4	44.5

systematic errors (%)

uncorrelated										
$\varepsilon_{\text{trig}}$	8									
$\varepsilon_{\text{etag}}$	2.1	1.5	1.2	0.5	0.4	1.1	2.6	4.0	6.0	9.3
correlated										
non-diffr. norm.	0.0	0.6	0.2	4.1	3.0	2.3	3.4	3.7	0.0	0.0
LAr	4.2	6.1	15.7	3.9	11.7	11.5	8.9	8.7	33.3	20.0
SPACAL	4.2	0.7	2.4	1.3	1.6	1.2	0.9	0.0	0.0	0.0
correlated, scale										
C_{FMD}	1.5									
C_{diss}	6.1									
L	2									

$$d\sigma / d\langle \eta_{\text{jet}}^{\text{had}} \rangle$$

Bin	1	2	3	4	5	6	7	8	9
$\langle \eta_{\text{jet}}^{\text{had}} \rangle$ min,max	-1,-0.7	-0.7,-0.4	-0.4,-0.1	-0.1,0.2	0.2,0.5	0.5,0.8	0.8,1.1	1.1,1.4	1.4,1.7
$d\sigma/d\langle \eta_{\text{jet}}^{\text{had}} \rangle$ (pb)	89	253	439	402	349	264	139	70	36
Errors:									
stat. (%)	19.1	9.4	7.2	8.7	9.9	11.2	16.2	21.4	42.1
syst. uncorr. (%)	8.9	8.1	8.0	8.0	8.0	8.0	8.0	8.0	8.0
syst. corr. (%)	7.9	11.2	11.5	13.7	13.3	14.0	11.4	11.8	11.2

statistical errors (%)

$N_{\text{data}} - N_{\text{nd}}$	16.4	8.5	6.4	6.0	7.7	7.9	12.1	15.4	30.2
C_{ε}	9.7	4.1	3.3	6.3	6.3	8.0	10.8	14.8	29.4

systematic errors (%)

uncorrelated									
$\varepsilon_{\text{trig}}$	8								
$\varepsilon_{\text{etag}}$	3.9	1.3	0.2	0.2	0.1	0.1	0.2	0.3	0.3
correlated									
non-diffr. norm.	2.3	3.8	1.6	1.0	4.3	0.0	5.7	0.0	0.0
LAr	2.6	8.0	9.2	11.5	10.7	12.3	7.4	9.5	9.1
SPACAL	2.6	2.0	1.5	3.2	1.7	0.6	0.0	2.4	0.0
correlated, scale									
C_{FMD}	1.5								
C_{diss}	6.1								
L	2								

$$d\sigma/dM_{12}^{\text{had}}$$

Bin	1	2	3	4	5	6	7
M_{12}^{had} (GeV) min,max	6,9	9,12	12,15	15,18	18,21	21,24	24,27
$d\sigma/dM_{12}^{\text{had}}$ (pb GeV ⁻¹)	19	90	50	23	11	5	3
Errors:							
stat. (%)	17.6	6.8	7.5	10.6	15.4	21.3	27.2
syst. uncorr. (%)	8.0	8.0	8.0	8.0	8.1	8.1	8.2
syst. corr. (%)	18.9	14.1	9.8	7.1	15.6	22.0	21.5

statistical errors (%)

$N_{\text{data}} - N_{\text{nd}}$	9.1	4.5	5.6	8.4	13.0	18.6	23.4
C_{ε}	15.1	5.0	4.9	6.4	8.3	10.4	13.8

systematic errors (%)

uncorrelated							
$\varepsilon_{\text{trig}}$	8						
$\varepsilon_{\text{etag}}$	0.2	0.1	0.3	0.4	0.9	1.1	1.6
correlated							
non-diffr. norm.	0.4	3.2	0.6	1.9	3.9	0.0	4.3
LAr	16.5	11.6	6.9	0.0	12.9	20.7	20.0
SPACAL	6.6	3.4	2.2	2.0	4.3	3.4	0.0
correlated, scale							
C_{FMD}	1.5						
C_{diss}	6.1						
L	2						

$$d\sigma/dy^{\text{had}}$$

Bin	1	2	3	4	5	6	7	8
y^{had} min,max	0.3,0.35	0.35,0.4	0.4,0.45	0.45,0.5	0.5,0.55	0.55,0.6	0.6,0.65	0.65,0.7
$d\sigma/dy^{\text{had}}$ (pb)	2818	2065	1840	1725	1186	751	1078	1180
Errors:								
stat. (%)	11.6	8.5	6.9	7.4	9.4	18.9	16.0	26.6
syst. uncorr. (%)	11.0	8.5	8.0	8.2	8.8	10.1	12.9	20.2
syst. corr. (%)	18.0	10.4	12.8	12.2	9.2	17.6	10.2	10.2

statistical errors (%)

$N_{\text{data}} - N_{\text{nd}}$	7.0	6.4	6.3	6.8	8.6	18.1	13.3	18.1
C_ϵ	9.2	5.7	2.8	3.1	3.8	5.5	8.8	19.5

systematic errors (%)

uncorrelated								
ϵ_{trig}	8							
ϵ_{etag}	7.6	2.9	0.4	1.6	3.6	6.1	10.1	18.5
correlated								
non-diffr. norm.	1.1	1.7	0.6	1.2	3.1	13.9	4.7	5.2
LAr	16.6	7.7	10.9	10.0	5.6	8.6	6.2	5.9
SPACAL	2.4	1.9	1.2	2.2	0.7	0.0	0.0	0.0
correlated, scale								
C_{FMD}	1.5							
C_{diss}	6.1							
L	2							